6-27-2022

BIOMIMETIC STRATEGIES TO CONTROL THERAPEUTIC RELEASE FROM NOVEL DNA NANOPARTICLES

Robert J. Mosley
Rowan University

BIOMIMETIC STRATEGIES TO CONTROL THERAPEUTIC RELEASE FROM NOVEL DNA NANOPARTICLES

by

Robert J. Mosley

A Dissertation

Submitted to the
Department of Biomedical Engineering
Henry M. Rowan College of Engineering
In partial fulfillment of the requirement
For the degree of
Doctor of Philosophy
at
Rowan University
April 29, 2022

Dissertation Chair: Mark E. Byrne, Ph.D., Professor and Founding Department Head, Department of Biomedical Engineering

Committee Members:
Jacek Wower, Ph.D., Professor, Department of Animal and Dairy Sciences, Auburn University
Vince Beachley, Ph.D., Associate Professor and Graduate Coordinator, Department of Biomedical Engineering
Sebastian Vega, Ph.D., Assistant Professor, Department of Biomedical Engineering
Mary Alpaugh, Ph.D., Associate Professor, Department of Molecular & Cellular Biosciences
Chun Wu, Ph.D., Associate Professor, Chemistry & Biochemistry

Dedication

This work is dedicated to my friends and family. Thank you for your continued love and support.

Acknowledgements

I would like to thank Dr. Mark Byrne and Dr. Jacek Wower for their advice, support, and guidance throughout my professional pursuits. I would like to thank my committee members, Dr. Vince Beachley, Dr. Sebastian Vega, Dr. Mary Alpaugh, and Dr. Chun Wu for their knowledge and assistance during my research, without which none of this would be possible. I would also like to thank Dr. Peter Galie, Dr. Cristina Iftode, Dr. Liana Wuchte, Dr. Stephen DiPasquale, Dr. Laura L. Osorno, and Dr. David Brennan for their valuable advice and assistance over the course of my research. I extend my appreciation to my colleagues, Brandon DeOre, Kiet Tran, Matthew Flamini, Matthew Grisley, Brendan Rucci, Kadie L. Davis, and Ashleigh Jankowski. Special thanks go to Dr. Ricky Whitener for training me early in my career. I want to thank Dr. Mindy George-Weinstein, Dr. Grzegorz Gorski, and Dr. Jacquelyn Gerhart for assistance with cell culture. I would also like to thank my NSF REU mentees Julia Hart and Patricia Poley.

Abstract

Robert J. Mosley
BIOMIMETIC STRATEGIES TO CONTROL THERAPEUTIC RELEASE FROM NOVEL DNA NANOPARTICLES
2021 - 2022
Mark E. Byrne, Ph.D.
Doctor of Philosophy in Biomedical Engineering

The inherent chemical, mechanical, and structural properties of nucleic acids make them ideal candidates for the formulation of tunable, personalized drug nanocarriers. However, none so far have exploited these properties for the controlled release of therapeutic drugs. In this dissertation, a biomimetic approach to controlling drug release is exhibited by specifically manipulating the architecture of novel, DNA nanoparticles to take advantage of drug binding mechanisms of action. Rationally designed DNA strands were immobilized on gold surfaces via a terminal thiol modification. Immobilized monomers can be manipulated to form distinct monolayer architectures including flat, folded, coiled, or stretched structures. Increasing the rate of folding is shown to restrict the diffusion of a surface-bound drug while upright architectures released drug at a 2 - 10 fold rate, depending on sequence length - using this strategy an over four-week release of dexamethasone was achieved. Furthermore, the release of an intercalating drug is controlled by exploiting sequence-specific affinities of the drug toward DNA. Here, using a high-affinity sequence and increasing the strand length a near zero-order release of daunomycin was achieved for up to 12 days. With this work, it is shown for the first time that the mechanisms of drug binding to nucleic acids can be utilized to produce highly controlled drug release from gold-core nucleic acid nanoparticles. These results will have a profound impact on the future design of novel, therapeutic nanocarriers.

Table of Contents

Table of Contents (Continued)

Table of Contents (Continued)

Table of Contents (Continued)

List of Figures

List of Figures (Continued)

Figure Page

List of Tables

Chapter 1

Introduction

1.1 Background

Cancer is a leading cause of death and a growing public health crisis worldwide. In 2020 alone it was associated with over 13 million new diagnoses and more than 6 million deaths.[1] Although referred to as a "disease", cancer is a general term describing a class of diseases identified by abnormal cell proliferation generally identified by uncontrolled cell proliferation triggered by the accumulation of genetic mutations. Cancers are distinguished by the site of origin: the top three cancers by diagnoses are breast, lung, and colorectal, and the top three by mortality are lung, colorectal, and liver. In low and middle-income countries, a significant fraction of cancers are caused by pathogens that are implicated in the development of cancer.[1] In all other populations, almost half of all cancers are caused by risk factors like tobacco and alcohol consumption, unhealthy diet, physical inactivity, and exposure to pollutants.[2] For cancers that have a good surveillance method, can be detected early, or are still organ confined, effective treatment and improved prognosis is more likely. However, late diagnosis or metastasized cancers still present a high risk of mortality, and certain types (e.g. pancreatic, liver, small-cell lung, and uterine corpus) remain significantly challenging to treat effectively.

In the United States, cancer is the second leading cause of death (21% of all mortality) and the leading cause of death among women aged 40-79 years and men aged 60-79 years. The chances of being diagnosed are 40.2% for men and 38.5% for women over a lifetime. Breast, prostate, lung, and colorectal cancer accounting for about half of

all diagnoses. In 2022 there will be almost two million new cancer cases, about 5,000 each day, and over 600,000 deaths, about 1,700 per day, in the US alone. The total economic burden is expected to reach over $246 billion by 2030 with annual average medical costs for patients exceeding $42K, $5K, and $105K in the initial, continuing, and end-of-life phase of care, respectively. The burden will be exacerbated in subsequent years due to the substantial reduction in routine cancer screenings caused by overwhelmed healthcare facilities during the COVID-19 pandemic.[3,4]

Modalities in cancer therapy have gone through a series of phases over the past century (Figure 1.1). Although cancer has been known to practitioners of medicine for millennia, it was not until the late 19th century that the idea of chemically treating the disease, or chemotherapy, was proposed by Dr. Paul Ehrlich. It was initially his research on the affinity of small molecules that led to his hypothesis of molecularly targeted compounds, or, in his own words, “wir müssen chemisch zielen lernen” (“we have to learn how to aim chemically”).[5] In the following years George Clowes successfully transplanted tumors in rodents leading to a phase of developing relevant clinical models which resulted in the Sarcoma 37 (S37), Sarcoma 180 (S180), Walker 256, and Ehrlich's ascites tumor models.[6] This phase culminated in Murray Shear's 1935 program for cancer drug screening, which screened over 3,000 compounds but was ultimately dropped due to a lack of understanding of cancer and the ethical issues of testing toxic compounds in humans.[7]

The fervent search for chemotherapeutics continued after World War II stemming from the observation of depleted lymph nodes and bone marrow in soldiers exposed to mustard gas; this resulted in the discovery of a number of alkylating agents and folate

analogs used with little success throughout the 1950s. It was not until the 1960s, assisted by the discovery of the double helix by Watson and Crick, that the idea of DNA function-affecting compounds as anticancer agents emerged.[8] The first example of a cured cancer was Hodgkin's lymphoma, in 1970, via aggressive administration of a combination of chemotherapeutics.[9]

Improved understanding of cancer-specific genetics and signal transduction pathways, along with the production of the first monoclonal antibodies (mAbs) in 1975,[10] led to the next phase of specific targeting of cancer hallmarks led by the treatment of chronic myelocytic leukemia via Bcr-Abl tyrosine kinase inhibitor in 1996.[11] In the following decade the immune therapies, including immune checkpoint inhibitors and modified T cells expressing chimeric antigen receptors (CAR T-cell therapy), began to emerge.[12,13] The suboptimal clinical efficacy of these new targeted therapies, and the previous success of combination therapies, resulted in a shift to applied nanotechnology to produce targeted drug payload carriers, or nanocarriers. The beginning of the nanocarrier phase is marked by the FDA approval of Doxil in 1995.[14] The nanocarrier strategy is highly emphasized in the current day, fueled by a continued investigation of patient and disease-specific cancer hallmarks leading the field to the precipice of truly personalized therapeutics.[15] Unfortunately, there are still challenges to overcome.

1.2 Motivation

The difficulty in treating cancer is due to the unique properties of the disease itself (Figure 1.2). The major characteristics of cancer are uncontrolled growth and proliferative signaling, genetic instability and mutation, stimulation of angiogenesis, evasion from growth suppressors and the immune system, inflammation, and the

promotion of invasion and metastasis (Table 1.1). The so-called "tumor microenvironment" accounts for all stages of cancer progression including tumorigenesis, growth, proliferation, and metastasis.[16] Due to the difficulties in specifically targeting cancer cells, the search for the proverbial "magic bullet" has so far failed.[5] An emerging paradigm in cancer treatment revolves around the manipulation of materials at the nano-scale to produce multifunctional, specifically targeted therapeutic agents. Nanoparticles have been observed passively accumulating at tumor sites due to the upregulation of vascularization in tumors via the enhanced permeability and retention (EPR) effect. Furthermore, nanotechnology provides an outstanding suite of techniques and strategies for tuning materials for physical, chemical, and functional properties useful in medicine. *In vitro*, this has led to the formulation of highly functional, stimuli-responsive, "smart" nanomedicines designed with regard to specific cancer hallmarks or microenvironmental triggers. Of the multitude of nanomaterials in use, nucleic acids (NAs) have emerged as a very promising component in the construction of next-generation cancer therapeutics.[17] The unique information-carrying properties imbued by the sequence-specific base pairs, directed layer-by-layer assembly, stimuli responsiveness, biocompatibility, and drug loading capacity are all advantages of NAs which make them attractive for constructing cancer nanomedicines. However, controlled and extended release constitutes a great challenge at the nanoscale. A strategy that takes advantage of the mechanisms of action of drug binding to nucleic acids has yet to be exhibited and would significantly improve drug release kinetics and nanocarrier design. Therefore, the main goal of the research herein is to engineer novel nucleic acid nanoparticles and develop methods by which the

release of chemotherapeutics can be controlled via a biomimetic approach to drug loading and release.

1.3 Objective

A tunable, tailorable, platform-based delivery of therapeutic molecules would revolutionize both diagnostics and therapeutics for cancer treatment.[18] This work, therefore, is motivated by the desire to develop such a platform with emphasis placed on NAs as the functional component. The specific objectives involve the discovery and development of novel methods of controlling the release of chemotherapeutic drugs bound non-covalently to the surface of nucleic acid-based, biohybrid nanoparticles via biomimetic design strategies (Figure 1.3). Specifically, biomimetic strategies involve manipulation of the mechanical and structural properties of DNA and exploiting drug binding mechanisms of action to control release. Chapter 2 will describe the rational design of drug nanocarriers and the influence of key physical properties on their *in vivo* fate with emphasis on NA nanocarriers. Chapter 3 introduces a dendritic DNA nanocarrier loaded with cytotoxic doxorubicin engineered to target a specific subpopulation of cells via conjugation of a monoclonal antibody; an elegant and high-throughput cell culture model was designed and showcased to compare a novel controlled release mechanism to a bolus injection in dynamic flow environments. Chapter 4 introduces DNA-gold conjugates as a platform for building advanced nanocarriers, with the controlled manipulation of DNA layers on both planar gold surfaces and gold nanoparticles highlighted. Chapter 5 utilizes the manipulation of DNA films on gold to control the release of a surface bound chemotherapeutic, dexamethasone. Here, controlled release is achieved via modulation of DNA nanoarchitecture correlated to the

degree of folding about the gold core. Chapter 6 subsequently showcases the controlled release of the intercalating chemotherapeutic daunomycin from DNA films on gold. In this case, control is achieved via modulation of DNA sequence and length, taking advantage of the mechanism of binding of daunomycin to DNA. Comparisons of release profiles from planar gold films and gold nanoparticles are also shown. Chapter 7 provides a summary of conclusions, highlighting major results and significant contributions to the field of drug delivery and nanocarrier design.

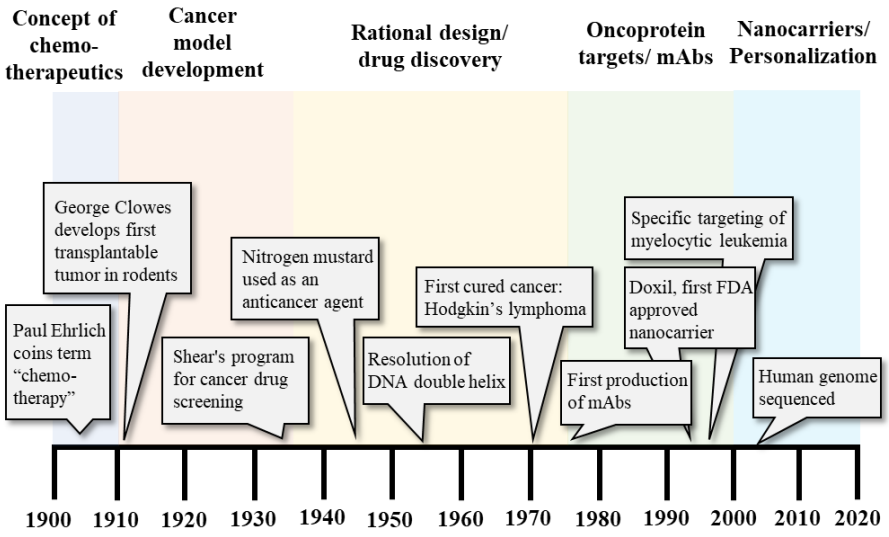

Figure 1.1. A brief history of chemotherapy. The history of chemotherapy starts with Dr. Paul Ehrlich who posited the idea of chemically targeting cancer in the early 1900s, thus inventing the concept of chemotherapeutics. The next phase involved the rapid development of relevant clinical models for different cancer types. The rational design and discovery of chemotherapeutic drugs was accelerated by novel effects observed due to mustard gas, leading to the focus on alkylating agents as anticancer drugs. Throughout the mid-1900s, spurred by the discovery of the DNA double helix, a large number of novel drugs were synthesized to target DNA replication; this phase culminated in the first cured cancer via combination therapy in 1970. For the rest of the century, targeted therapies began to emerge based on specific oncogenes and proteins, with the very late years of the 1900s showcasing the utility of drug nanocarriers with the approval of Doxil. Over the past few decades, an improved understanding of cancer genetics and heterogeneity has pushed the development of highly tailorable nanocarriers for the multiplexed delivery of chemotherapeutic drugs.

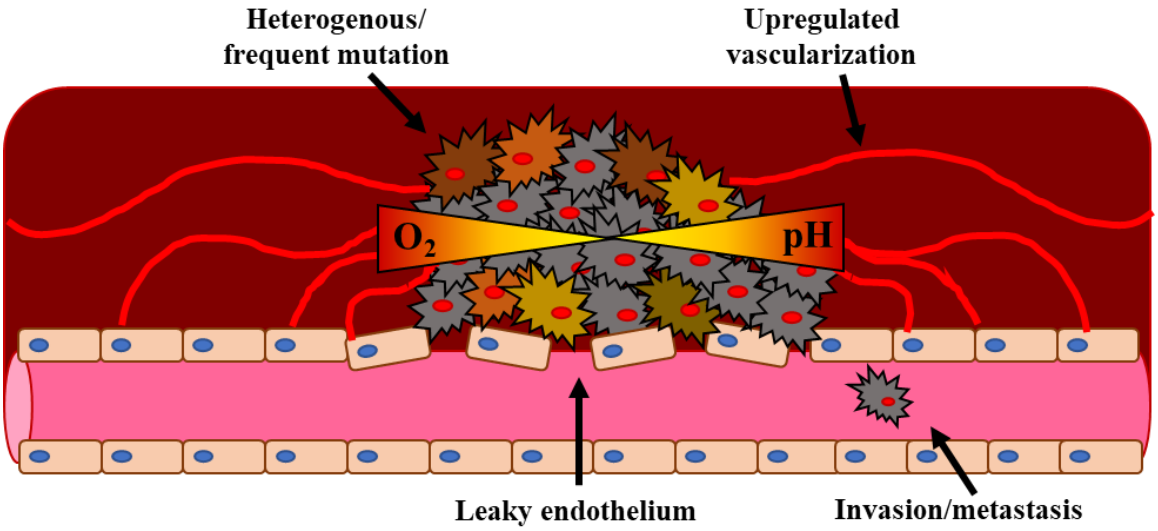

Figure 1.2. The tumor microenvironment. The tumor microenvironment plays a role in all stages of cancer progression including tumorigenesis, growth, proliferation, and metastasis. Triggered by mutations that cause unchecked multiplication and proliferation, tumors grow rapidly at the tissue or organ of origin. Upregulated vascularization draws nutrients from the blood stream while dysregulated gene expression helps cancer cells evade growth suppressors and the immune system. The resultant vasculature is tortuous and leads to inflammation, intratumoral pressure, and a buildup of metabolic waste. Over time, tumors can metastasize and invade other tissue.

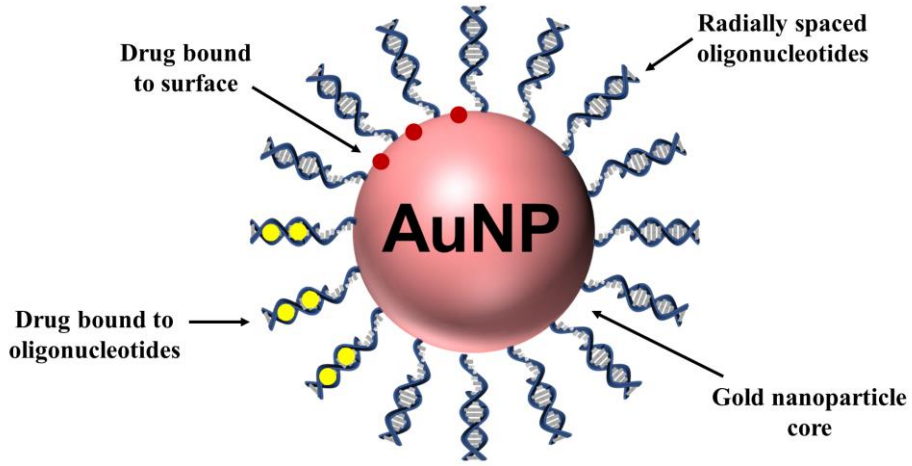

Figure 1.3. A novel, biohybrid therapeutic nanocarrier**.** The main subject of this work is a novel, biohybrid nanocarrier formed via conjugated of a 5' thiol-terminated oligonucleotide to the surface of a 15 nm gold nanoparticle in a radially arranged orientation. Various drugs can be bound non-covalently to the surface of the particle by adhering them to the gold surface or by arranging them within the nucleic acid monolayer. The mechanisms of drug binding and manipulation of nucleic acid structures can be used to control drug release.

Table 1.1

Difficulties in Treating Cancer

Cancer property	Result
Uncontrolled growth	• Accumulation of mutation • Aberrant signaling • Promotion of invasion
Proliferative signaling	• Tumor growth • Evasion of growth suppressors • Cancer progression
Genetic instability and mutation	• Genetic heterogeneity • Acquired resistance to treatment
Stimulation of angiogenesis	• Increased nutrient uptake • Accumulation of metabolic waste
Evasion of growth suppressors and immune system	• Unchecked proliferation • Resistant to body's natural defenses
Inflammation	• Intratumoral pressure • Restricts delivery of therapeutics • Causes further tissue damage
Promotion of invasion and metastasis	• Cancer spread throughout the body • Affects unrelated tissue • Difficult to diagnose/treat

Chapter 2

Rational Design of Nanocarriers for Improved Drug Delivery

2.1 Introduction

Nanomedicine is one of the most promising drivers of next-generation therapeutic strategies for the management of pressing diseases. The unique optical, magnetic, electronic, and structural characteristics that emerge at the nanoscale have resulted in the rational design of novel formulations tailored for urgent medical needs including sensing and imaging, drug delivery, tissue engineering, and gene therapy.[19–21] Since the introduction of the term "nanomedicine" over 30 years ago, research on the topic has expanded significantly with more than 50 approved formulations, hundreds of ongoing clinical trials, and a 1000X increase in peer-reviewed manuscripts.[22–24] Most affected has been cancer treatment due to the development of a variety therapeutic agents designed with molecular precision for the treatment of specific cancer genotypes.[25] Additionally, advances in diagnostics and treatment of, e.g., reproductive diseases,[26] Alzheimer's,[27] infectious disease,[28] cardiovascular disease,[29] viral diseases,[30] chronic inflammation,[31] and neurodegenerative diseases[32] have showcased the utility of nanomedicine in a broad range of diseases. At its core the advantage of nanomedicine lies in the tunability of nanomaterials which allow for highly versatile and multifunctional therapeutic agents, often referred to as personalized medicines (Figure 2.1).[33] In particular, the inclusion of biomolecules has had an enormous impact on the rational design of nanomedicines. The chemical complexity and high molecular weight of biomolecules imbue intricate architectures and unique mechanical properties to biohybrid materials.[34,35] They are generally highly functional and exhibit dynamic and stimuli-triggered responsiveness, i.e.

"smart" materials.[36–40] Designs inspired by or mimicking the complexity of biological tissue have increased precision and personalization in both diagnostics and therapeutics.[41]

Unfortunately, the unpredictable efficacy of nanomedicines in human patients related mainly to in vivo pharmacokinetics, tissue distribution, immunological responses, and penetration and accumulation at the target site have limited the clinical success of nanomedicines.[42–44] Biological barriers such as fluid dynamics within the blood, opsonization and recognition by the mononuclear phagocyte system, extravasation to the disease site, and intracellular compartmentalization all determine the in vivo fate of nanomedicines and thus must be considered in the design of novel formulations.[45] Attempts at designing biomimetic materials meant to mimic the dynamic properties of biological tissue have revealed the lack of understanding of biomolecular physics at the nanoscale.[46,47] Thus, a new paradigm of bio-inspired materials has focused instead on exploiting the modulatory nature of biomolecules as building blocks of nanoparticle therapeutic delivery vehicles, or nanocarriers, instead of using them strictly for their biological mechanisms of action. In terms of therapeutic delivery, nanocarriers maintain advantages over other nanomedicines including diversity of payload, high drug-to-targeting-ligand ratio, multivalency, and controlled drug release.[48] Furthermore, utilizing bio-inspired materials in this way allows for more simplified, holistic design principles that can dictate nanocarrier formulation for improved therapeutic outcomes.[49–51]

In this chapter, a summary of the physical properties of nanocarriers and their effect on in vivo fate will be discussed. These properties include the size, shape, mechanical properties, and surface properties of nanocarriers. These properties are then discussed specifically in the administration of nucleic acid-based nanocarriers due to their

unique applicability as controllable, self-assembling, and highly functional building blocks for nanomedicines. Finally, the controlled release of therapeutics from nucleic acid-based nanocarriers will be discussed.

2.2 The Influence of Physical Properties on Nanomedicine Fate In Vivo

The most important factor in the design of nanomedicines is their interactions with biomacromolecules. Thus, many researchers take the approach of functionality through synthesis whereby specific chemical units are incorporated onto nanocarrier surfaces to exploit their inherent biological mechanisms of interaction.[52] For example, outfitting surfaces with small molecules, polymers, biomolecules, etc., can impart specific biomedical functionalities including immune recognition, cell internalization, molecular targeting, drug loading, biosensing, and biological stealth. The chemical tailorability of nanomaterials presents a seemingly limitless collection of possible surface modulations that has accelerated the development of novel nanomedicines and nanocarriers; however, the excitement has not led to a proportional increase in clinical translation.[53]

The myopic focus on functionality and the lack of clinical success has revealed an immense ignorance of the essential physical parameters that drive the biological interactions of nanomaterials. In this section, a general overview of these parameters - specifically, size, shape, mechanical properties, and surface properties - and their effect on the in vivo fate of nanocarriers will be presented and discussed.

2.2.1 Size

Nanoparticles, by nature of their dimensions, are able to freely circulate through vasculature and are readily cleared from tissue.[54,55] However, physiological barriers

imposed by organs involved in filtration, recognition, and removal of foreign material - particularly the kidneys, liver, and spleen - severely limit therapeutic delivery and induce prohibitive side effects via accumulation of toxins in these organs. Particle size plays an important role in the ability of a nanocarrier to maneuver through these physiological barriers (Figure 2.2).

Renal filtration is the process by which the kidneys filter waste products out of the blood and excrete them in urine. This process will remove most particles of < 15 nm in diameter and all particles of 6 nm or smaller.[56] Thus, 15 nm is the lower limit for a circulating nanocarrier. Increasing particle size, however, correlates to an increase in phagocytosis and the accumulation of particles in the liver; this occurs in the range of 15 - 200 nm.[57,58] This process occurs largely via resident macrophages known as Kupffer cells,[59] although particles on the lower end of this range are also removed via receptors on liver sinusoidal endothelial cells and hepatic stellate cells.[60] It is also driven by adhesion of circulating opsonin proteins which allow for recognition of foreign materials. The role of the spleen in nanocarrier sequestration is less broadly elucidated. Marginal zone macrophages within the spleen were observed to selectively internalize nanoparticles with sizes between 100 - 200 nm.[61] Larger particles are subsequently filtered out and retained in the red pulp of the spleen where they become internalized by red pulp macrophages; sequestration in the red pulp is maximized with particles larger than 400 nm in diameter.[61]

The size of a nanocarrier also affects the ability to marginate to endothelial tissue. Margination is the movement of nanocarriers under dynamic fluid flow from the center toward the walls of a channel. For most drug delivery applications, margination is

imperative as it encourages attachment and diffusion of nanocarriers through the endothelium and into disease sites. It was previously found that particles of less than 100 nm were found to interact with the endothelium more often compared to larger particles.[62] This phenomena is likely due a result of lower drag force and larger contact area of smaller particles.[63] In tumors, margination is less important as the EPR effect encourages passive accumulation at the target site. The intervascular pores in tumors, which do not exist in most healthy tissue, are between 100-780 nm in diameter and thus a wide range of particle sizes can naturally accumulate in these spaces.[64] However, larger particles tend to induce higher background accumulation in healthy tissue in spite of the EPR effect.[65] Therefore, designing nanocarriers with diameters between 15 - 100 nm would provide the most efficient tumor targeting without accumulation in healthy organs or tissue.

2.2.2 Shape

Precision in nanotechnology has resulted in the synthesis of a wide variety of nanoparticle shapes, including spheres, rods, discs, stars and polyhedra. Only recently was shape investigated as a driver of biological interactions (Figure 2.3). One of the most influential parameters regarding nanoparticle shape is the surface curvature. On the nanoscale, the high surface area to volume ratio of particles results in significant curvature compared to more macro-sized curved particles. This high curvature can substantially alter the orientation of surface bound ligands, such as conjugated antibodies, which significantly affects binding specificity and avidity of targeted nanocarriers.[66,67] Additionally, surface curvature can affect macrophage uptake. Highly curved surfaces lower the thermodynamic barrier to protein adsorption and thus are recognized and

phagocytosed by macrophages at a higher rate.[68,69] They also show increased accumulation in the liver compared to disc-shaped or hexagonal nanoparticles.[57,63,68] Indeed, the local surface curvature affects the rate of phagocytosis by directly influencing the actin structure of macrophages; spherical particles that require a gradual expansion of actin ring are phagocytosed more efficiently compared to particles that require a high degree of macrophage spread along the surface.[70]

Similar to surface curvature, the aspect ratio of nanocarriers plays a significant role in influencing biological interactions. Ellipsoidal or rod-shaped nanoparticles are phagocytosed at a much lower rate than spherical nanoparticles, which is related to the lower surface curvature along the long axis.[71,72] Indeed, this observation is less pronounced in shorter rod-shaped particles which tend to accumulate more frequently within the liver.[73] Regarding tissue penetration, the tumbling motion of rod-shaped nanoparticles in the blood stream results in increased contact and adherence to endothelial tissue.[74] Furthermore, compared to spherical particles they show increased transport across intestinal endothelium, blood-brain-barrier, accumulation in tumors, and passive diffusion to the nucleus.[75–78] Aspect ratio also affects biological function and cytotoxicity. Increasing particle aspect ratio has been observed to influence cellular functions such as proliferation, apoptosis, cytoskeleton formation, adhesion and migration.[79] Furthermore, higher aspect ratio, "needle-shaped" particles were found to induce a significant amount of cytotoxicity due to lysosomal disruption.[80] Particles with very high aspect ratios are known as filamentous nanoparticles. These have shown the excellent ability to remain in circulation up to ten times longer than spherical nanoparticles and are readily taken up by endothelial tissue.[81,82]

2.2.3 Mechanical Properties

The mechanical properties of nanocarriers have only recently been recognized as a mediator of effective drug delivery (Figure 2.4).[83] As such, the effects of mechanical properties on drug delivery are not fully understood. Soft particles exhibit significantly improved circulation times compared to rigid particles.[84] The deformability of soft particles increases their ability to pass through biological filters (e.g., in the spleen) leading to improved circulation time and reduced uptake by the immune system; additionally, the deformability of a particle significantly reduces the rate of phagocytosis.[70,85,86] However, this flexibility also increases interactions with opsonin proteins which can increase the rate of macrophage uptake.[87]

Opsonization is significantly reduced by increasing the rigidity of a nanocarrier.[87,88] However, the flow dynamics of hard particles result in a higher chance of marginating and encountering macrophages within the liver.[89] Surface-bound ligands are able to interact with the biological environment more readily on the surface of rigid nanoparticles. In the case of ligand targeting, this leads to improved receptor mediated uptake; however, in cases such as Fc-receptor-mediated phagocytosis, uptake by macrophages is also increased for rigid particles.[90,91]

Overall, conclusions about the optimum mechanical properties of nanocarriers are difficult to draw. At times reports may contradict about the biological effect of varying mechanical properties. For example, both increasing and decreasing the moduli of nanoparticles have shown advantages regarding targeting and tissue penetration.[91,92] As such, mechanical properties must be optimized on a case-by-case basis in order to tune the nanocarrier for targeting and transport through specific physiological environments.[93]

2.2.4 Surface Properties

Chemical properties such as charge and hydrophobicity are understood to affect protein adhesion, transport through tissue, interactions with cells, transcytosis, phagocytosis, and particle biodegradation.[58,94–98] However, a less understood mediator of nanocarrier fate is in the nanoarchitectures of the functional ligands bound to a particle surface. As discussed above, functionalization via conjugation of ligands is the most popular method of formulating nanocarriers but has not translated to significant clinical success. Therefore, this section will discuss physical considerations for the functionalized surface layer in the context of nanocarrier interactions with the biological environment.

Functional groups grafted to the surface of nanocarriers dictate many of the interactions the nanocarrier has with biological barriers. These interactions are not always simply understood. For example, certain surfactants are able to mimic lipoprotein particles to encourage transport across the blood-brain-barrier, while others do not elute the same kind of uptake.[99] The density of functional ligand, specifically those meant for molecular targeting, is also essential for dictating particle-cell interactions. Increasing ligand density results in stronger and faster bond formation with its target, although too high of a density can lead to reduced interactions.[74,100] Thus, it is not only density but the local nanoarchitecture that dictates the *in vivo* fate. Indeed, nanoparticle tropism for neutrophils was seen to be significantly dependent on the supramolecular arrangement of proteins rather than size, shape or charge.[101] In experiments using self-assembled monolayers of oligo(ethylene glycol) and polyethylene glycol, polymers commonly utilized to increase solubility and reduce biofouling, it was found that resistance to

protein adsorption and cell uptake were more dependent on the spatial configurational freedom of the polymer chains than the density of the polymer on the surface.[102,103]

The effect of polymer architecture also extends to the formulation methods of the nanocarrier. It was shown that nanocarriers with grafted PEG-PLA coatings had significantly reduced protein binding and macrophage uptake compared to multiblock PLA-PEG-PLA polymer despite the relatively lower PEG content.[104] Verma et al. constructed nanoparticle "isomers" using 11-mercapto-1-undecanesulphonate 1-octanethiol in either a striated or randomly distributed conformation. They confirmed that the striated polymer coating allowed for penetration of the plasma of the plasma membrane without disruption where the randomly distributed coating restricted nanoparticles to the endosomes.[105] Here, therefore, the biomimetic approach is key to tuning the biological interactions of a nanocarrier. For example, nanoporous silicon particles showed excellent "cell-like" properties after being coated with membranes purified from leukocytes.[106]

2.3 Nucleic Acid Nanocarriers

Nucleic acids (NAs) are commonly known as the essential holders of genetic information for the perpetuation of all life. They are extremely versatile building blocks in the construction of complex networks and nanostructures. NAs are biological polymers consisting of helically stacked purine and pyrimidine bases that are connected to a sugar-phosphate backbone and form the well-known double helix structure. At the turn of the 21st century, advances in NA chemistry provided the opportunity for large-scale, inexpensive production of synthetic NAs.[107] Around the same time, reports of the SELEX method for discovering molecularly targeted NAs increased the interest in utilizing NAs

in the construction of multifunctional theranostic tools.[108–111] The specificity of base pairing along with conjugation chemistry allowed self-assembly and layer-by-layer deposition strategies for facile synthesis of highly modular and versatile materials to act as therapeutics (Figure 2.5).[112] Over the last 30 years, NA therapies approved by the FDA have included antisense oligonucleotides, siRNAs, one aptamer (Pegaptanib), and two mRNA-based vaccines for COVID-19 granted emergency use authorization by FDA.[113] Furthermore, there are currently over one hundred ongoing clinical trials involving NA therapeutics.[114]

Effective targeted or systemic delivery of NA therapies is limited mainly due to the physiochemical properties of NAs themselves. As large hydrophilic molecules they are unable to penetrate cell membranes. Additionally, their susceptibility to enzymatic activity causes them to be rapidly degraded in the bloodstream and in the cytoplasm. As a result, most NA therapies require chemical modification of oligonucleotides or administration alongside active molecular enhancers in order to remain stable in vivo for delivery to disease sites.[115,116] More contemporary strategies have placed high emphasis on designing nanocarriers for efficient delivery of NAs, mostly involving methods of encapsulating or protecting the cargo instead of utilizing it as a functional unit within the nanocarrier itself.[117,118] This strategy can prove effective but it significantly limits the functionality of NAs. For example, engineered NAs with specific sequence sites related to targeting, immunomodulation, structural stability, and drug loading can be incorporated into a single, modular nanocarrier.[119] With each facet of this nanocarrier contained within a single, molecular component, the physical properties of the nanocarrier can then be tuned for a specific purpose. The physical properties discussed in

Section 2.2 will be again discussed in the following section with specific focus on NA nanoparticles.

2.4 Rational Design of Nucleic Acid Nanocarriers

NAs administered systemically have three major barriers to overcome: stability and degradation in physiological media, tissue localization and penetration to the target site, and unwanted activation of the immune system. Due to the molecular precision and variety of nanostructures possible via NA engineering, there are multiple emerging strategies that allow tunability regarding these three barriers. These strategies are closely related to the physical parameters discussed in Section 2.2. Thus, this section will focus on rational design strategies for tailoring the physical properties of NA nanocarriers for improved performance in biological systems. Specifically, the spherical nucleic acid (SNA) nanocarrier - nanoparticles with radially oriented oligonucleotides - will be highlighted.

2.4.1 Stability and Degradation

Complex NA nanostructures are often unstable in physiological media. This is due to the need for a sufficient concentration of cations to allow for dense NA packing which is unsuitable in low ionic buffers. However, rational nanostructural design can be used in biological applications.[120] By controlling the density of DNA helices in nanostructures, stability in physiological buffers can be achieved and has led to extremely stable DNA nanostructures spanning a wide range of complex shapes.[121] Supramolecular DNA nanostructures, such as "chain-armor" DNA catenanes formed via azide modified copper-catalyzed azide–alkyne cycloaddition (CuAAC) click chemistry, have also exhibited excellent stability.[122] For example, this structure was found to be stable up to

95ºC and after ethanol precipitation. Additionally, it was resistant to nuclease degradation.[122] Cationic polymer coatings are commonly utilized as protective agents against degradation, but often this leads to unanticipated changes in particle size, shape, and cell uptake.[123] One solution has been the complexation of copolymers with NA structures. Poly(ethylene glycol)−poly(l-lysine) (PEG−PLL) block copolymer conferred increased thermal stability to plasmid DNA and reduced the activity of DNase I.[124] The copolymer also restricted DNA aggregation compared to PLL homopolymer due to the segregation of DNA into the PEG core. Additionally, tubular DNA nanostructures were observed to aggregated when coated with oligolysines but not when coated with an oligolysine-PEG copolymer. This copolymer coating allowed the DNA structure to survive in acidic endosomal compartments and exhibited an increase in bioavailability in a mouse model.[125] Furthermore, mixed polymer coatings or encapsulations can be formulated to protect NA nanostructures, such as PEGylated lipid bilayers, which protect the nanostructure against nuclease digestion and improved bioavailability to a significant degree.[126] In another example, poly(2-dimethylaminoethyl methacrylate) poly(ethylene glycol) (PDMAEMA-PEG) copolymer was complexed with tubular DNA nanostructures. Not only were the resulting complexes stable in physiological media, by tuning the copolymer coverage they were able to control the catalytic activity of encapsulated enzyme.[127]

SNAs provide a unique architecture for improving NA stability *in vivo*. Since the oligonucleotides are not conjugated via base pairing, and due to high surface curvature at the nanoscale reducing intermolecular repulsion, stability in physiological salt concentrations is maintained. Furthermore, with the multivalent and cooperative

hybridization to SNA surfaces, melting temperatures are increased and sharp melting curves have been observed using SNAs.[128] These structures also reduce enzymatic degradation. The steric hindrance induced by dense oligonucleotide packing can inhibit enzyme binding; furthermore, even bound enzymes are restricted from catalyzing hydrolysis due to the local surface charge and salt concentration within the NA shell-layer.[129,130]

2.4.2 Tissue Localization

Targeted, tissue-specific delivery is essential for nanocarriers carrying highly cytotoxic chemotherapeutic drugs. For NA nanocarriers, conjugation of a targeting ligand can be done via complementary base pairing with either aptamers or other oligonucleotide-functionalized moieties. However, considerations of ligand density, spatial arrangement, and orientation are imperative as they can directly determine particle affinity and avidity toward the target.[131] Furthermore, encapsulated NA nanostructures may hinder the binding mechanism of surface-bound molecules.[132] Therefore, careful consideration of the location and orientation of targeting ligands must be taken. NA nanocarriers can also take advantage of the EPR effect for tumor targeting. Even in the absence of a targeting ligand, increasing the size of RNA nanocarriers improved accumulation at tumor sites.[133] Indeed, the flexibility of NA nanostructures contributes significantly to its ability to penetrate tissue, accumulate within tumors, and avoid sequestration by the immune organs.[134]

Tissue targeting of SNAs is achievable via tuning of constituent components of the particle. First off, particle size can be controlled by selecting core diameters and oligonucleotide lengths. Radially oriented NA layers also retain a significant amount of

flexibility allowing for deformability and more efficient penetration of tissue layers.[135] Furthermore, SNAs are capable of binding multiple targeting probes with higher binding constants for complementary strands compared to free NAs.[136] In fact, the shape of SNAs improve the display of conjugated targeting ligands and increase binding avidity.[67] SNAs are also profoundly capable of being taken up by cells and have shown to rapidly accumulate in over 50 different cell lines without the need for transfection reagents.[137] The mechanism of internalization is due to weak, non-specific protein binding on the SNA surface activating scavenger receptors and leading to internalization[138]; this mechanism is also highly dependent on the density and architecture (i.e., radial orientation) of the NA layer.[139] This allows for SNA transport across difficult physiological barriers such as the skin and the blood-brain-barrier.[140,141] Indeed, even for cation coated SNAs the shell orientation remains capable of inducing cellular uptake.[142]

2.4.3 Immunogenicity

The recognition of foreign NAs involves the activation of the innate immune system, specifically host pattern recognition receptors such as the toll-like receptors (TLRs) and retinoic acid–inducible gene-I-like helicases (RLHs).[143] This recognition is highly dependent on the size, shape, and structure of the circulating NAs.[144] For example, RLH proteins retinoic acid–inducible gene-I (RIG-I) and melanoma-differentiation–associated gene 5 (MDA5) recognized NAs depending on the oligonucleotide length and TLR-9 activation is enhanced by curved DNA structures.[143,145] Furthermore, pattern recognition receptors can have specificity for specific helical structures, such as B-form DNA, over others.[146]

Planar NA structures are significantly more immunostimulatory compared to chain or fiber nucleic acids.[147,148] It was additionally found that specific shapes, such as triangles, squares, or pentagons, can induce distinct immune responses with varying magnitudes of immune stimulation.[149] Cubical nucleic acid structures of both RNA and DNA have shown to have vastly different immune stimulating properties.[148] Furthermore, the inclusion of single-stranded nucleic acids extended from vertices can induce a strong immune response that is not observed when the vertices are unconjugated.[150] It has been observed that 3D tetrahedrons induce stronger immunostimulation compared to planar structures driven by sequence specific extensions from vertices.[150]

The immune response to internalized SNAs is significantly decreased compared to free NAs. Specifically, this is due to a restriction in the activity of enzymes responsible for recognizing foreign NAs and was observed to be inversely dependent on the surfaces density of oligonucleotides.[151] Indeed, the display of immunostimulatory oligonucleotides, such as the CpG motif, can be tailored on SNAs to tune the activation of macrophages.[152] This control has led to a great emphasis on using SNAs as vaccine adjuvants. Co-delivery of antigens paired with an SNA construct showed markedly improved immunostimulation depending on how the antigen was incorporated into the nanoparticle.[153] An SNA designed with peptides for human prostate-specific membrane antigen (PSMA) resulted in elevated secretion of cytokines and increased cytotoxic T cell activity in humanized mice and human peripheral blood mononuclear cells.[154] More recently, an SNA coated with the COVID-19 receptor-binding domain (RBD) subunit and a dense shell of CpG motif oligonucleotides led to a 100% survival rate in humanized ACE2 transgenic mice.

2.5 Controlled Release Strategies from Nucleic Acid Nanocarriers

Although used frequently as a drug carrier, controlling the release of drugs from NAs presents a significant challenge. This is due to the high surface area to volume ratio at the nanoscale, which allows for excessive hydration and solvation, along with the extremely short diffusion path for the drug to escape. However, utilizing NAs as nanocarriers as opposed to administering them alone as therapeutics leads to improved treatment outcomes and reduction of multidrug resistance.[155] Furthermore, controlled release is essential for therapeutics that act as circulating drug reservoirs, require passive or active targeting, and assists in avoiding off-target accumulation and associated toxicities.[156,157] NAs, with their profound capacity for layered self-assembly and modification, are ideal candidates for constructing controlled release nanocarriers.[158]

Physical triggers to alter NA structure are commonly used to control the release of drugs. Heat denaturing of NA shell-layers can be achieved via administration of near-infrared (NIR) light to injected, NIR absorbing gold nanoparticles (AuNPs); the specific wavelength of light can be tuned by changing the size of the AuNP core.[159] Additionally, pH sensitive structural changes, such as induction of the i-motif for C-rich oligonucleotides, can effectively be used as triggered drug release in low pH environments. Dexamethasone-conjugated oligonucleotides hybridized to a DNA nanotube via the i-motif sequence showed selective drug release under acidic pH at 37°C.[160] This technique has also been used to release intercalating doxorubicin in endosomal compartments.[161] Specific recognition sequences have also been utilized to achieve enzyme-specific degradation and drug release from NA nanoparticles.[162]

Steric and electrostatic hindrance of drug diffusion can be exploited by blocking diffusion paths with oligonucleotides, a mechanism known as DNA-gated release. Most commonly this is done by loading drug into porous nanoparticles and arranging oligonucleotides to block the pores. This strategy can be used effectively and reversibly in a temperature specific manner where thermal melting and rehybridization of DNA duplexes effectively triggers the release or entrapment of the drug payload.[163] Using an aptamer as the gate mechanism allows for triggered release of drug payloads in response to specific antigens.[164–167] This mechanism can also be exhibited on non-porous nanoparticles. For example, we recently showed that the release of dexamethasone bound to a AuNP surface can be slowed substantially by promoting folded, looping DNA structures in the DNA shell layer (discussed in Chapter 5).[168] Indeed, engineering nanoparticles with these sequence specific gate mechanisms has led to the exhibition of higher order "logic" mechanisms that are able to multivalently target specific molecular antigens and trigger specific release of encapsulated therapeutics.[169–171]

Intercalating drugs are popular payload candidates for NA nanocarriers due to their inherent ability to bind to NA sequences. However, controlled release of intercalators presents a great challenge. Certain intercalators, such as daunomycin, are known to have sequence-specific affinities toward NAs. Specifically, daunomycin is known to bind with high affinity to the AGC oligonucleotide motif. We have shown that the arrangement of this motif along an oligonucleotide conjugated to AuNPs can affect the loading and release of daunomycin.[172] More recently, by engineering AGC-motif oligonucleotides on gold films we showed near zero order release of daunomycin (discussed in Chapter 6). Therefore, drug release can be controlled from NA shell-layers

via careful engineering of the sequence, size, and structure of the oligonucleotides.

2.6 Conclusions

NA nanocarriers are quickly gaining recognition as one of the most promising nanomaterials for the formulation of next-generation drug delivery vehicles. Indeed, the programmability of NA nanomaterials is expected to significantly impact diagnostics and therapeutics for improved treatment outcomes in a wide range of diseases. These materials can be tailored for highly specific molecular targeting, tissue penetration, payload delivery, stimuli-responsiveness, biosensing, in vivo detection, and beyond.[173] In particular, SNAs represent an outstanding platform for constructing NA nanomedicines. SNAs provide unmatched size control, stability, tissue penetration, cell internalization, and controllable assembly allowing for extreme precision in personalizing and tailoring nanocarriers for specific patients or diseases. Currently, no SNA platforms have been approved by the FDA, although a first-in-human phase 0 clinical study of RNA interference–based spherical nucleic acids in patients with recurrent glioblastoma has recently commenced.[174]

The future of nanomedicine will require rational design strategies that exploit the tunability of nanomaterials for specific purposes. In this review, a broader look at the physical properties of nanocarriers and how they affect behaviors *in vivo* was discussed. Although certain nanomaterials imbue functionalities, a holistic focus on nanocarrier size, shape, mechanical properties, and surface properties will significantly improve the pharmacokinetics and pharmacodynamics of administered nanomedicines. By utilizing NAs as the main functional unit, all of these properties can be determined with a high degree of precision via facile engineering of specific oligonucleotide sequences and

careful considerations of how they are assembled. Additionally, as a payload carrier, multiple classes of therapeutic drugs can be incorporated and the release controlled from the NA layer. It is envisioned that the controlled release strategies discussed in Section 2.5 can be incorporated into NA-based nanomedicine platforms of multiple shapes and sizes, thus formulating platforms whereby the core material determines the general size and shape, the outer layer determines molecular targeting and biological interface, and the layers in between serve as drug reservoirs. Such a strategy is expected to revolutionize the field of nanomedicine in the future.

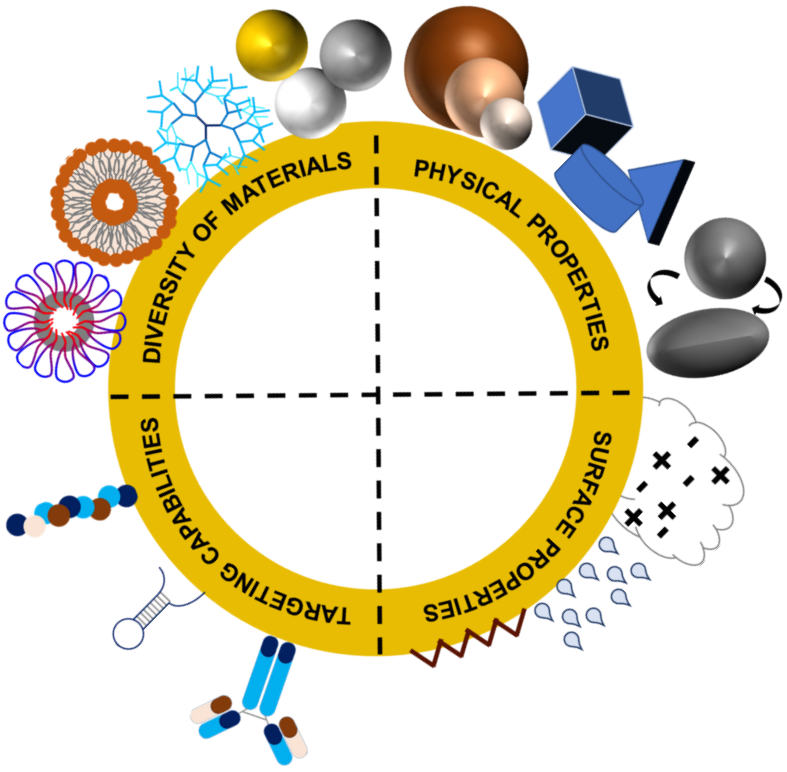

Figure 2.1. The tunability and versatility of nanomedicines. The profound tunability at the nanoscale provides outstanding precision in the construction of nanomedicines. A diverse toolbox of materials is available including polymersomes, liposomes, dendrimers, and inorganic nanoparticles. The physical properties including size, shape, and mechanical properties can be tailored for specific purposes. The surface properties can be chemically altered to produce a specific ionic charge, modulate hydrophobicity, and affect surface roughness. Finally, conjugation chemistry can decorate the surface of a nanomedicine with a functional unit, such as a targeting components, e.g. mAbs, aptamers, or peptides.

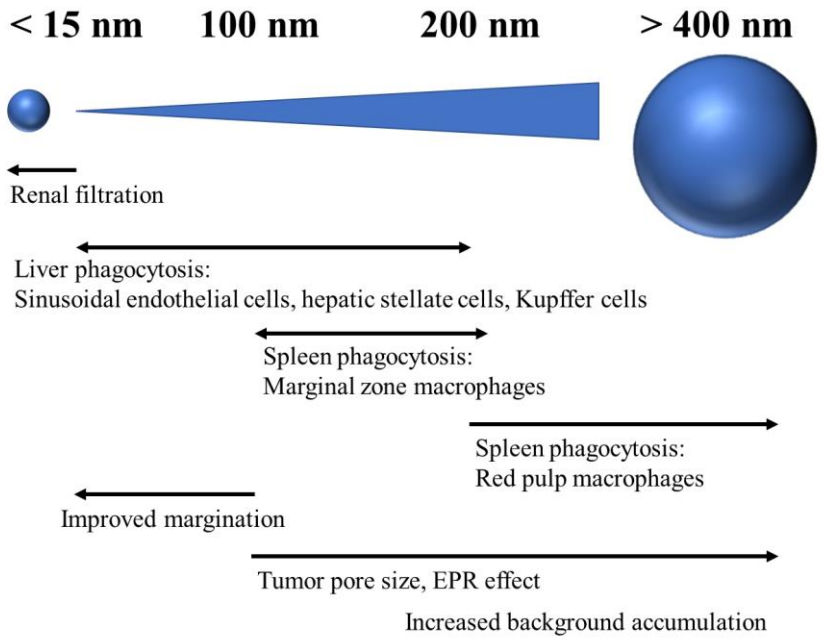

Figure 2.2. The effect of size on nanocarrier fate. Some well-defined size ranges of nanomedicines dictate their in vivo fate. Below 15 nm in diameter, nanomaterials are rapidly excreted in urine due to renal filtration. Phagocytosis in the liver is increased form sizes of 15 - 200 nm, mainly due to Kupffer cells but also due to alternate hepatic cells for particles on the lower end of this range. From 100 - 200 nm, nanomaterials are likely to be phagocytosed by marginal zone macrophages in the spleen, while particles greater than 200 nm are sequestered in the red pulp of the spleen. Margination is improved for particles less than 100 nm in diameter due to improved flow dynamics in the blood. Tumor vasculature in particular is quite porous, with pores in the range of 100 - 780 nm, leading to increased passive accumulation of nanomaterials. However, larger particles will still result in higher background accumulation in healthy tissue.

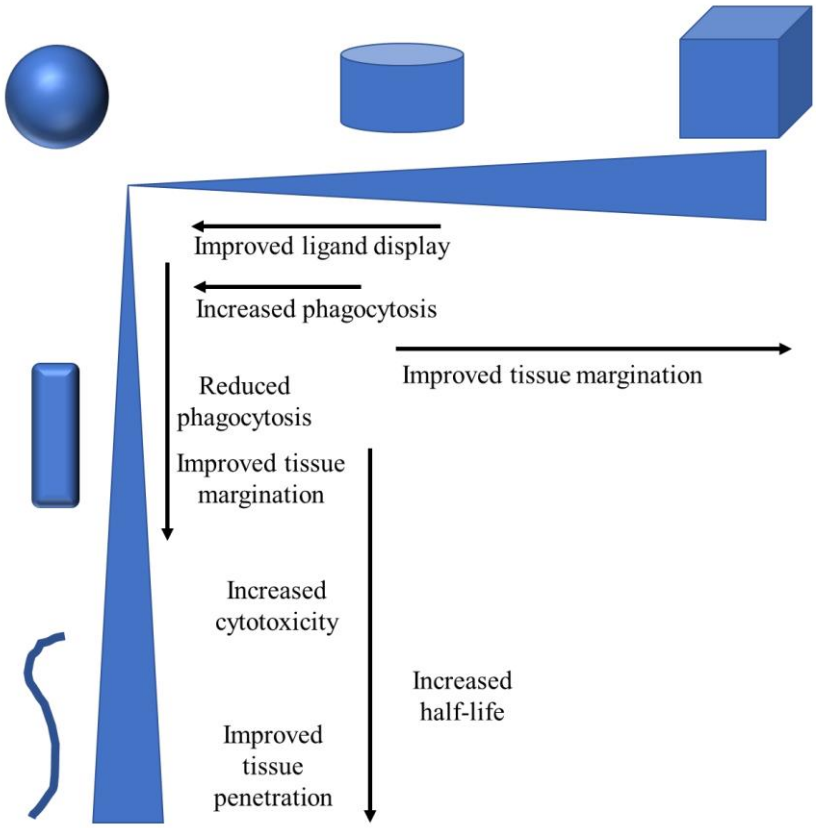

Figure 2.3. The effect of shape on nanocarrier fate. Both surface curvature (top) and aspect ratio (left) influence the in vivo fate of nanomedicines. Highly curved surfaces show improved ligand display especially with regard to molecular targeting and recognition. Curved surfaces are also more prone to opsonization and phagocytosis. Lower surface curvature, e.g. disc-shaped or cube-shaped particles, show improved tissue margination due to flow dynamics. Increasing he aspect ratio of a nanoparticle reduces the rate of phagocytosis and improves tissue margination. Higher aspect ratios, including filamentous particles, can show inherent cytotoxic effects, increased circulation times, and improved penetration through tissue layers.

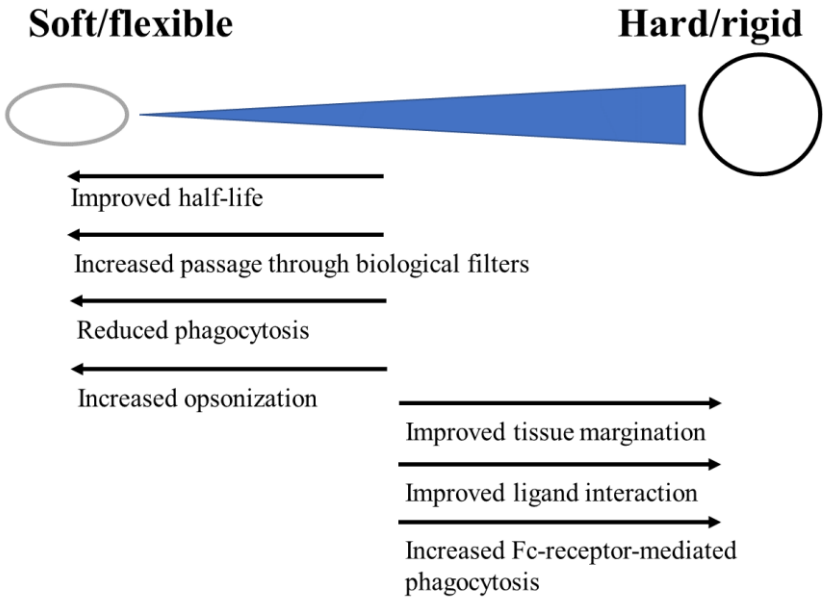

Figure 2.4. The effect of mechanical properties on nanocarrier fate. Softer/flexible particles show increased circulation times, improved transport through biological filters (e.g., renal or splenic filtration), reduces phagocytosis, and increased adhesion of opsin proteins - this is driven mainly by the deformability of the nanomaterial. Hard/rigid particles show improved marination to endothelium and improved ligand display regarding biomolecular interactions. However, this also leads to increased rate of Fc-receptor-mediated phagocytosis.

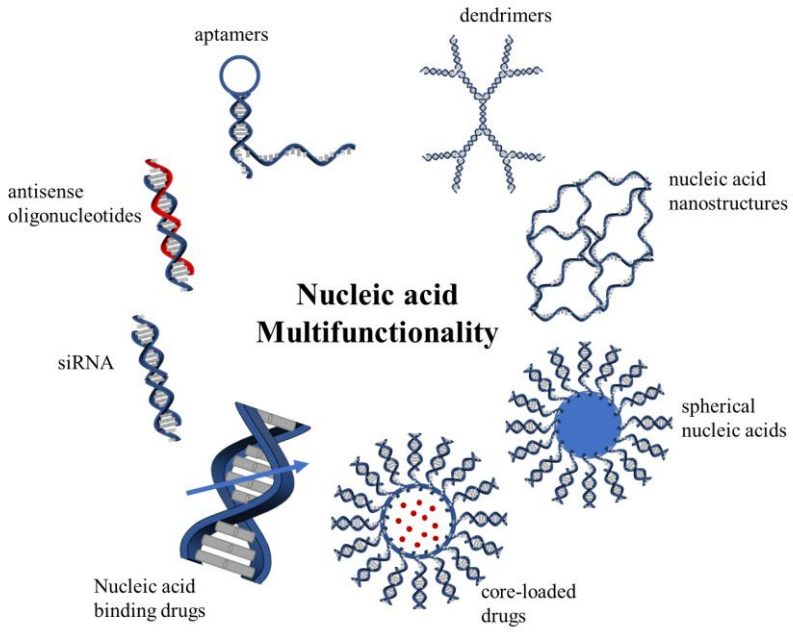

Figure 2.5. Nucleic acid therapeutic multifunctionality. Nucleic acids are highly versatile materials in the field of nanomedicine. Therapeutics include siRNAs, antisense oligonucleotides, and aptamers. Structurally, they can form dendrimers, complex nanostructures, or spherical nucleic acid platforms. They can also be used to load drug either within/on the particle itself or intercalated within the nucleic acid layer.

Chapter 3

Sustained Release of Antibody-Conjugated DNA Nanocarriers from a Novel Injectable Hydrogel for Targeted Cell Depletion

3.1 Introduction

Dendrimer nanoparticles are given much attention for use as advanced therapeutic nanocarriers.[175] They are a highly versatile structural platform comprised of an initiator core, branched substructures, and terminal functional groups**.** Based on simple base-pairing principles and driven by specifically designed single-stranded regions, multi-generational dendritic nanostructures can be easily constructed using carefully designed nucleic acids. The double-stranded regions can be used as a payload carrier for intercalating drugs and from the terminal branches a variety of functional units can be conjugated via complementary base pairing. A dendritic DNA nanocarrier loaded with cytotoxic doxorubicin and conjugated to the G8 monoclonal antibody (mAb) was developed by Code Biotherapeutics (Hatfield, PA), called 3DNA® (Figure 3.1). The 3DNA specifically targets cells expressing brain-angiogenesis-inhibitor 1 (BAI1) and depletes them via release of the intercalated drug. This chapter focuses on the design of a dynamic cell culture model used to test a controlled release formulation of 3DNA. The overarching goal of this study was to improve upon current treatment modalities for posterior capsule opacification (PCO), or secondary cataracts. It also serves as an excellent example of the multifunctionality of dendritic NA nanocarriers.

3.1.1 Motivation

Cataracts are a slowly progessing vision impairment disorder caused by the break down of fibers and proteins in the lens due to injury or aging. They are the leading cause of vision impairment and blindness worldwide.[176] Over 10 million cataract surgeries are

performed annually and this rate is expected to double over the next 10 years.[177] As a result of this predicament, the World Health Organization released a global action plan to increase access to cost-effective cataract surgeries.[178–180]

Surgery is currently the most effective method of treating cataracts. The procedure involves removal of opacified tissue in the lens, replacing the lens with an artificial intraocular lens (IOL). This surgery is safe and effective, and in most cases any complications that arise are manageable by an opthalmologist.[181] However, one major risk involved in cataract surgery is the emergence of PCO, also known as secondary cataracts. During the wound healing process post cataract surgery, a population of fibrotic cells migrates to the lens capsule. These fibrotic cells wrinkle the lens, and over time lead to significant vision loss.[182] PCO occurs in up to 40% of adult patients and nearly all children after cataract surgery.[183] Thus, improving the strategy for PCO prevention represents a pressing issue.

Currently the most effective treatment for PCO is neodymium-doped yttrium aluminum garnet (Nd:YAG) laser capsulotomy, which improves visual acuity by rupturing the opacified tissue with short, high-powered pulses of light.[184] However, Nd:YAG therapy is not available world-wide and there are often side effects from treatment including intraocular pressure spikes, cystoid macular edema, retinal detachment, and IOL damage.[185–188] Improvements in surgical techniques, IOL design, and understanding the influence of biomaterials on IOL performance have improved patient outcomes regarding PCO, but it still presents a significant burden on patients and the healthcare system.[189–192] Cytotoxic drugs and chemicals, including anti-inflammatories, immune-modulating agents, anti-cell migration compounds, and

cytotoxins have been administered after cataract surgery to prevent the initial migratory cell response of PCO, but these drugs eliminate cells non-specifically and drug diffusion to surrounding tissue can initiate an inflammatory response.[193]

With the increase in cataract surgeries expected worldwide, there is an urgent, unmet need for more effective, prophylactic treatment strategies to prevent PCO. The fibrotic cell response that leads to PCO is due to the migration of a specific subpopulation within the lens known as Myo/Nog cells.[194–196] Myo/Nog cells were first identified in the chick embryo blastocyst by their expression of the skeletal muscle specific transcription factor MyoD and the bone morphogenic protein inhibitor noggin.[197,198] Previous experiments revealed the commitment of these cells to the skeletal muscle lineage regardless of their environment.[194] In cultures of human lens tissue, Myo/Nog cells differentiate into myofibroblasts in response to wound healing.[194,195] Depletion of Myo/Nog cells in short-term and long-term cultures of human lens tissue prevented the accumulation of myofibroblasts.[194,195] A third marker of Myo/Nog cells is expression of BAI1 recognized by the G8 mAb.[197,199,200] The anti-BAI1 G8 mAb specifically targets Myo/Nog cells for depletion by complement mediated cell lysis or when conjugated to dendritic DNA nanocarriers loaded with cytotoxic doxorubicin (G8:3DNA:Dox).[194–197,199,201,202] Injections of G8:3DNA:Dox into the rabbit lens capsule during cataract surgery significantly reduced clinical signs of PCO after 28 days.[196]

A controlled release formulation for 3DNA would significantly improve clinical outcomes for patients after cataract surgery. One major advantage of a controlled release compared to a bolus injection is that humans PCO develops more slowly in humans than it does in rabbits.[203] Additionally, over time Myo/Nog cells from the ciliary body may

traverse the zonules and repopulate the lens.[204] In this study, we tested a sustained delivery formulation for delivery of G8:3DNA:Dox in cultures of human rhabdomyosarcoma cells containing a subpopulation that expresses BAI1.[205] The formulation consists of a biodegradable, *in*-situ forming PLGA-PEG-PLGA hydrogel that releases G8:3DNA:Dox for up to 4 weeks.[206] Herein, we compare a bolus dose versus hydrogel-mediated sustained delivery of G8:3DNA:Dox for cell targeting and depletion within a dynamic, microfluidic flow environment representing the fluid flow in the lens (Figure 3.2). The hypothesis underlying this work is that administration of the drug in a sustained delivery formulation will specifically eliminate the subpopulation of cells that express BAI1 more effectively than a bolus dose in long term, dynamic systems.

3.2 Materials and Methods

3.2.1 Materials

Triblock copolymer, PLGA-PEG-PLGA, with d,l-LA/GA ratio of 15/1, PLGA/PEG ratio of 2/1, and PEG with a molecular weight 1,500 Da was purchased from PolySciTech, Inc. (West Lafayette, Indiana). Poly(ethylene glycol) Mn 400 (PEG400) was purchased from Alfa Aesar (Harverhill, MA). G8:3DNA:Dox nanocarriers were obtained from Genisphere, LLC. Rhabdomyosarcoma (RD) cells were purchased from the American Type Culture Collection (ATCC CCL-136) (Manassas, VA). Phosphate-buffered saline (PBS) was purchased from VWR (Radnor, PA).

3.2.2 3DNA Nanocarrier Synthesis and Formulation

The term 3DNA refers to a novel, dendritic nanocarrier comprised of nucleic acid strands designed specifically for step-wise hybridization and layer-by-layer assembly, described previously.[195,207,208] It consists of approximately 3000 DNA bases with 36

single-stranded peripheral regions. The approximate molecular weight, diameter, and zeta potential of 3DNA are 10^6 Da, 60 nm, and -28 meV, respectively. Doxorubicin (Sigma-Aldrich, St. Louis, MO) was intercalated into double-stranded regions of 3DNA by incubating at room temperature at a ratio of 500:1 Dox:3DNA, resulting in >99% loading efficiency. The G8 mAb was conjugated to a DNA oligonucleotide via amine-to-sulfhydryl attachment using a heterobifunctional crosslinker (Pierce Crosslinking Kit; ThermoFisher Scientific) and hybridized to 3DNA peripheries via complementary base pairing. The final 3DNA construct contained 4 mAb per particle and had a diameter of 120 nm.

3.2.3 Injectable Hydrogel Formulation and Characterization

Solutions consisting of 10 (w/v)% PLGA-PEG-PLGA, 1.6 (v/v)% PEG400 were mixed on a tube rotator at 4°C for 24 h. This formulation was previously shown to transition into a hydrogel at 35°C with acceptable physical and optical properties.[206] Solutions were lyophilized and reconstituted with G8:3DNA:Dox in PBS to a final concentration of 0.7 ng 3DNA/μL. Solutions were kept at 4°C until ready for use.

To confirm the formation of a physical hydrogel, the viscoelastic properties of the hydrogel were investigated using an ATS RheoSystem NOVA Rheometer (State College, Pennsylvania). A stress-controlled temperature ramp was performed between two flat plates of diameter 25 mm with the gap between the plates set to 0.3 mm. The heating rate was 1°C/min and the stress was 4 dyn/cm^2 at a frequency of 1.0 rad/s. Optical clarity was determined by measuring light transmittance on a 96-well plate at 35°C using a UV/Vis spectrophotometer (SpectraMax M3, Molecular Devices). The wavelength range was between 400 to 700 nm. Release of G8:3DNA:Dox from hydrogels was performed in a

400 µL chamber under physiological fluid flow (2.5 µL/min) and detected in the release media via a fluorophore (Alexa647) conjugated to the nanocarriers.

3.2.4 Cell Culture and Cytotoxicity Tests

A Myo/Nog-like subpopulation was identified in cultures of RD cells by co-localization of antibodies to noggin and BAI1.[205] Therefore, this cell line was utilized to observe the targeting and depletion of BAI1+ cells with exposure to G8:3DNA:Dox. Cells were cultured in complete Dulbecco's Modified Eagle Medium (DMEM, 10% FBS, 1% antibiotic/antimycotic) in a 37ºC cell incubator (VWR) with 5% CO2. Cell viability tests were performed on cells cultured on 96-well tissue culture plates (VWR). To assess cytotoxicity, these cells were incubated with an aliquot of either hydrogel, 42 ng of G8:3DNA or 42 ng of G8:3DNA mixed with hydrogel. Viability was determined via calorimetric MTT cell viability assay (PromoCell).

3.2.5 Dynamic Cell Culture Experiments

RD cells were cultured in a standard 24-well tissue culture plate, which has a similar diameter (15.62 mm) to the lens capsule (12.53 mm).[206] Each well was capped using polydimethylsiloxane (PDMS) lens molds of the anterior capsule to form chambers of 400 µL volume with inlet and outlet ports for fluid flow (Figure 3.3). Cells were seeded into devices at a density of $2x10^5$ cells/mL and allowed to attach overnight. Then, 42 ng of G8:3DNA:Dox nanocarriers as a bolus or with hydrogel was injected into each device. A syringe pump was used to maintain a flow rate of fresh media at 2.5 µL/minute for up to 7 days. Cells were stained via the covalent, dead cell specific Live-or-Dye NucFix™ Red Staining Kit (Biotium, Fremont, CA) and then immediately fixed with 2% paraformaldehyde followed by permeabilization with 0.5% Triton X-100. BAI1 was

localized with the G8 IgM mAb.[200] The primary antibody was visualized using affinity-purified, F(ab')2 goat anti-mouse IgM μ-chain conjugated with a fluorophore (Bio-techne, Minneapolis, MN). Finally, nuclei were stained with Hoechst dye (Bio-techne, Minneapolis, MN). Immunofluorescence was analyzed with an inverted fluorescent microscope (Zeiss) equipped with AxionCam ICm1 camera and Multi-Image-04 ZEN 2 lite image analysis software program. Cell counts and identification were performed using ImageJ.

3.3 Results

The RD human rhabdomyosarcoma cell line was used to test the efficacy of the drug delivery system. About 12(±9)% of the RD136 cell population is BAI1+.[205] A novel microfluidic system was designed to culture the cells in a small volume and under dynamic fluid flow in order to mimic the lens capsule environment more closely (Figure 3.3). Thus, G8:3DNA:Dox nanocarriers, either as a bolus or with a sustained release hydrogel, could be injected into each well and cell targeting could be compared over time.

3.3.1 Hydrogel Characterization

This study utilized a PLGA-PEG-PLGA triblock copolymer hydrogel for its injectability, controlled gelation temperature, and ability to sustain the release of G8:3DNA:Dox. Rheological characterization is shown in Figure 3.4A. The storage modulus of the hydrogel is near zero below 30^{o}C, suggesting a Newtonian fluid with good injectability. It then spikes between temperatures of 30-45^{o}C. Qualitatively, gelation can be confirmed via the vial-inversion method[209] and it was confirmed that the hydrogel transitions at a temperature of 35^{o}C. Rheology revealed a storage modulus of 170.5 Pa at

this temperature. The storage modulus reaches its peak at 37°C (474.6 Pa) before beginning to decline until reaching a final value of 35 Pa at 49°C. Furthermore, the hydrogel appears optically clear. The measured light transmittance over the wavelengths 470-750nm is greater than 80% for the hydrogel alone (Figure 3.4B). After loading with G8:3DNA:Dox, the light transmittance is slightly improved and retains greater than 80% transmittance over wavelengths 420-750nm.

In Figure 3.4C we show the release of G8:3DNA:Dox from hydrogels in a 400 µL chamber under constant fluid flow of 2.5 µL/min. These release conditions represent the fluid flow within the lens and the small volume allows for a smaller diffusion gradient compared to conditions such as infinite sink. In the microfluidic model conditions, the release of the nanocarrier is sustained for 672 hours, or four weeks. After 24 hours, only 1.2% of nanocarriers are released, indicating that no burst release is occurring and that the transport of the nanocarriers out of the gel is controlled. A cell viability assay was used to determine the cytotoxicity of PLGA-PEG-PLGA hydrogel and G8:3DNA nanocarriers without intercalated doxorubicin. The results are shown in Figure 3.5. Aliquots of hydrogel, G8:3DNA nanocarriers, and a combination of the two showed cell viability greater than 90% indicating that the hydrogel and targeted nanocarrier are nontoxic without the drug payload.

3.3.2 Dynamic Cell Studies

We compared a bolus dose and sustained delivery of G8:3DNA:Dox for their ability to kill BAI1+ cells in long term, dynamic cell cultures. The results are shown in Figure 3.6. Cells in our experiments showed an average expression of 15.9% BAI1+ cells. Relative expression was reduced over time as cells proliferated. The greatest rate of

off-target (BAI1−) depletion was 3.2% after 24 hours in cells treated with the bolus dose. Otherwise, less than 1% of BAI1− cell depletion was observed over the course of the experiment.

The bolus dose of G8:3DNA:Dox showed improved BAI1+ cell targeting after the first 24 hours but the relative targeting declined steadily over the course of the week. At 24 h, relative depletion of 26±15% and 10.4±14.2% BAI1+ cells was observed for bolus and hydrogel treated cells, respectively. Note that these averages are statistically similar. By day 3, only 5.5±2.3% of BAI1+ cells were depleted in cultures treated with the bolus. On day 7 < 2% of BAI1+ cells were depleted. The sustained release of G8:3DNA:Dox showed increased targeting of BAI1+ cells over the course of the. By day 3, 47.9±13.4% of BAI1+ cells were depleted. The result is similar at day 5, with 45.2±21.5% BAI1+ cells targeted. At day 7, 74.2±21.4% of BAI1+ cells were non-viable with release of G8:3DNA:Dox from the hydrogel. Images of specific targeting of BAI1+ cells by G8:3DNA:DOX nanocarriers is shown in Figure 3.7.

3.4 Discussion

PCO is expected to rise with the rate of cataract surgery over the next 10 years. There are no reliable indicators of vulnerability to developing PCO, and therefore, effective methods of preventing its development are imperative to preventing vision loss in patients, especially for those lacking access to Nd:YAG laser therapy. A large barrier in this case is the challenge of effective drug delivery to treat ocular disorders due to the unique physiological barriers present within the eye, ocular fluid dynamics, difficulty in accessing posterior portions of the eye, and low drug bioavailability.[210–212] The structure of the lens capsule and the fluid dynamics therein make intraocular drug delivery

difficult.[213,214] Due to these challenges, many effective ocular treatments are hindered by the need for multiple doses or invasive surgical interventions. As the healing process after cataract surgery can last for weeks, it is imperative that the release of a therapeutic is sustained.

At the forefront of ocular drug delivery are thermoresponsive hydrogels and nanoarchitectures that can achieve a sustained release of therapeutics within the eye, including hydrophilic, hydrophobic, and bioactive drugs.[215–218] Injectable, *in situ* gelling systems in particular present an excellent area of focus due to the ability to provide minimally invasive, site specific dosages of drugs for long term administration.[219,220] In particular, PLGA-PEG-PLGA triblock copolymer hydrogels have emerged as excellent vehicles for ocular therapeutics due to biocompatibility and sustained therapeutic release.[221–223] When in contact with the aqueous humor within the eye, PLGA degrades into its monomers lactic acid and glycolic acid which are metabolized by natural biological processes. Additionally, PLGA-PEG-PLGA hydrogels have tailorable mechanical and optical properties and the capability to sustain therapeutic release. Similar polymers have been studied previously and show no sign of toxicity.[224,225] We show similar observations for our hydrogel in Figure 3.5.

In a previous study, a bolus injection of G8:3DNA:Dox administered in a static environment required two doses to deplete all BAI1+ cells in cultures of human lens tissue.[195] Therefore, we developed a microfluidic system within a 24-well tissue culture plate as a high-throughput method to investigate the long-term prophylactic capabilities of G8:3DNA:Dox in a dynamic environment. Microfluidic designs are able to simulate complex physiological processes and environments to better assess fluid dynamics and

biochemical concentration gradients.[226–228] This allowed us to compare a bolus dose of G8:3DNA:Dox and an injectable, sustained release formulation of G8:3DNA:Dox in a more physiologically relevant environment. In dynamic cultures of RD136 cells in which a subpopulation expresses BAI1, we see that after three days the bolus injection of nanocarriers targets less than 10% of BAI1+ cells. This value continues to decrease for the 3DNA bolus injections until nearly no BAI1+ cells were targeted at 7 days. This is due to the high turnover of fluid which occurs in 3-4 hours within the chamber, which would rapidly reduce the nanocarrier concentration. Conversely, G8:3DNA:Dox nanocarriers in hydrogel continue to deplete BAI1+ cells at an increasing rate over the course of 7 days. On day 7, over 70% of all BAI1+ cells were targeted and killed by nanocarriers released from the hydrogel. This significant difference in cell depletion is due to the transition at physiological temperatures to a non-flowing hydrogel that resides within the culture chamber. The hydrogel subsequently continues to release nanocarriers leading to extended exposure to cells over a longer time period. In all cases, G8:3DNA:Dox specifically targeted the BAI1+ subpopulation via the conjugated G8 mAb, which is necessary to avoid non-specific cell depletion. While it is unknown whether BAI1+ cells remaining in these cultures arose from the proliferation of untargeted BAI1+ cells or from de novo expression of this molecule, these results demonstrate that sustained delivery of the drug in the hydrogel formulation is more effective than bolus delivery for targeting this population.

This work can be compared to previous *in vivo* studies involving bolus injections of G8:3DNA:Dox in adult rabbits during cataract surgery.[196] Animals treated with G8:3DNA:Dox showed little to no clinical evidence of PCO (determined via slit lamp

analysis and histology) 28 days after cataract surgery. However, BAI1+ Myo/Nog cells remained in the lens and more Myo/Nog cells may enter the lens by traversing the zonules from the ciliary body,[204] suggesting that vision impairment can still emerge over time. In the system used here, the ability of a bolus injection of G8:3DNA:Dox to deplete BAI1+ cells began to wane after only 3 days. The sustained hydrogel release, on the other hand, continues to specifically kill BAI1+ cells for at least 7 days.

3.5 Conclusions

Administration of a drug that prevents PCO would reduce vision loss in patients and significantly lessen the burden on the healthcare system. PCO can be reduced by injecting a drug that targets Myo/Nog cells during cataract surgery. However, the physiological conditions within the lens indicate that the concentration of a drug will decline over time. Herein we showed that a biodegradable, *in situ* forming hydrogel loaded with G8:3DNA:Dox targeted nanocarriers significantly outperformed a bolus injection in killing BAI1+ cells in dynamic cell cultures. The hydrogel is in situ forming, non-toxic and optically clear at 37^{o}C, and therefore, could be injected into the lens capsule during cataract surgery. Over time, the hydrogel would degrade into nontoxic components. A microfluidic device utilizing cells cultured on 24-well plates under physiological fluid flow allowed for high-throughput comparisons of BAI1+ cell toxicity over one week via treatment with either a bolus injection of G8:3DNA:Dox or within our PLGA-PEG-PLGA hydrogel formulation. Over time, BAI1+ cells were targeted at a much higher rate using the sustained release hydrogel. A bolus injection did kill BAI1+ cells within the first 24 hours of treatment; however, nearly all remaining BAI1+ cells were viable after 7 days, while sustained release of the drug continued to kill cells over

the course of a week. We expect that targeting would extend for longer than 7 days, as G8:3DNA:Dox was observed to release from the hydrogel for up to 4 weeks. This hydrogel formulation has potential for sustaining drug delivery to prevent PCO.

This work also accentuates a main focus of this dissertation, i.e. the advantages and versatility of NA nanocarriers. The 3DNA nanocarrier is a highly customizable platform for conjugating antibodies for the specific delivery of therapeutics. It is formulated using facile manipulation of NA sequence to control the directed assembly of a multigenerational nanocarrier construct. The platform nature of NA nanotechnology allows for novel applications in a number of pressing diseases - indeed, just this year Code Biotherapeutics has received significant funding to use 3DNA as a treatment for genetic therapy in rare liver disease.[229] It is expected that dendritic NA nanocarriers will prove advantageous for site-specific administration of drugs or delivery to protected regions such as ocular spaces, the skin, or the blood-brain-barrier, where systemic circulation is avoided or not necessary. However, in systemic circulation, NA dendrimers suffer from many of the issues discussed in the previous chapter with regard to stability and degradation, tissue localization, and immunogenicity. Additionally, dendrimers cannot exploit the EPR effect in tumors without further conjugation with PEG or to a nanoparticle core.[118,230] Thus, for systemic circulation and delivery to solid tumors, a more sophisticated architecture is required.

Spherical nucleic acids (SNAs) emerged in the late 20th century as a method of rationally assembling macrostructured networks of gold nanoparticles (AuNPs).[231] Since then, SNAs have become a class of their own due to their unprecedented capabilities of long circulation, stability, and tissue penetration. They have also been utilized in novel

ways to carry drug payloads.[172,232] The following chapter will describe the characterization of NA monolayers on gold surfaces and investigate methods by which the NA shell-layer can be manipulated for the purpose of controlling drug release.

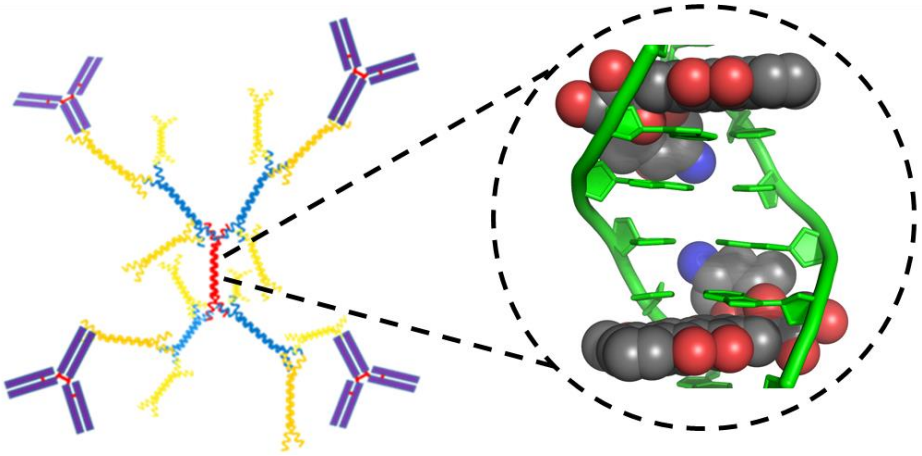

Figure 3.1. Schematic of 3DNA nanocarriers**.** 3DNA is a novel, dendritic nanocarrier comprised of nucleic acid monomers designed specifically for step-wise hybridization and layer-by-layer assembly. It contains approximately 3000 DNA bases, 36 single-stranded peripheral regions, and four conjugated mAbs per particle. Doxorubicin is intercalated into double-stranded regions of 3DNA. The final diameter of 3DNA is 120 nm.

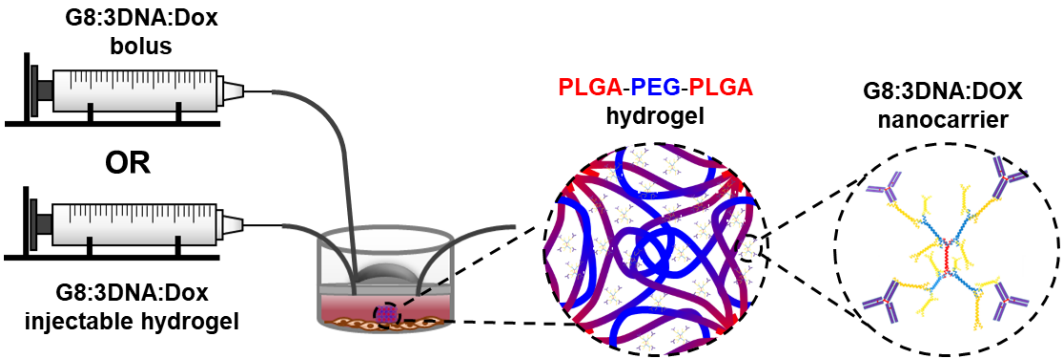

Figure 3.2. Schematic of experimental design**.** Cells were cultured in a 24 well plate capped with PDMS and fresh media was flowed over the culture at a rate of 2.5 µL/min. G8:3DNA:Dox nanocarriers as a bolus or within a hydrogel were injected into the well at the beginning of the experiment. Upon injection and incubation at 37^{o}C, the hydrogel transforms into a non-flowing gel and remains in the chamber for the entirety of the experiment. The 3DNA is released slowly over the course of 4 weeks.

Figure 3.3. The dynamic cell culture design. Close up image of the cell culture chambers in each well. Cells are cultured on the bottom of the plate. Constant fluid flow was maintained within the chamber and throughout the tubing. The total volume within each well was 400 µL.

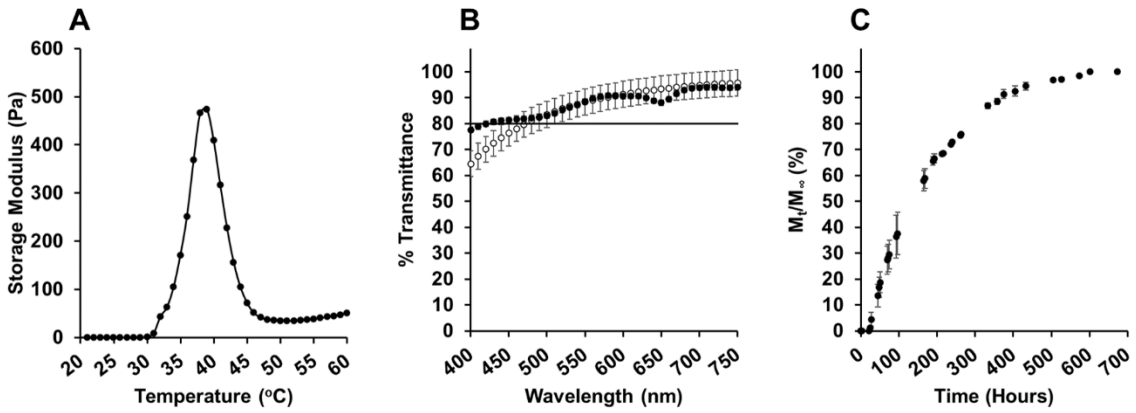

Figure 3.4. Characteristics of G8:3DNA:Dox/PLGA-PEG-PLGA hydrogel. **(A)** Rheological measurements of the hydrogel storage modulus as a function of temperature. A peak at physiological temperature confirms that the solution is transitioning to a hydrogel. **(B)** Optical clarity presented as percentage of light transmittance from 400-750nm wavelength. PLGA-PEG-PLGA(○), G8:3DNA:Dox/PLGA-PEG-PLGA(●). Optical clarity above 80% shows that the gel will not impair vision. **(C)** Release of G8:3DNA:Dox from PLGA-PEG-PLGA hydrogel in microfluidic device over time. Nanocarriers released from the hydrogel for up to four weeks.

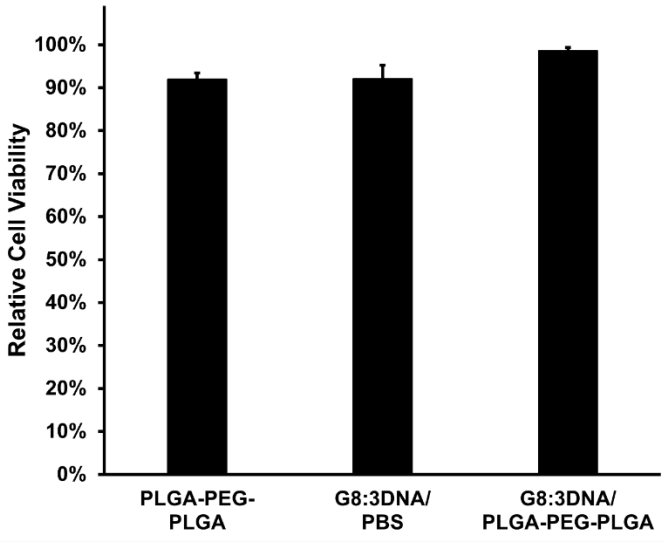

Figure 3.5. Results of MTT cell viability assay. after treating cultures with PLGA-PEG-PLGA hydrogel, nanocarriers in PBS, and nanocarriers with hydrogel. Cell viability was measured without the presence of Dox. All components retain above 90% cell viability indicating that they are non-cytotoxic.

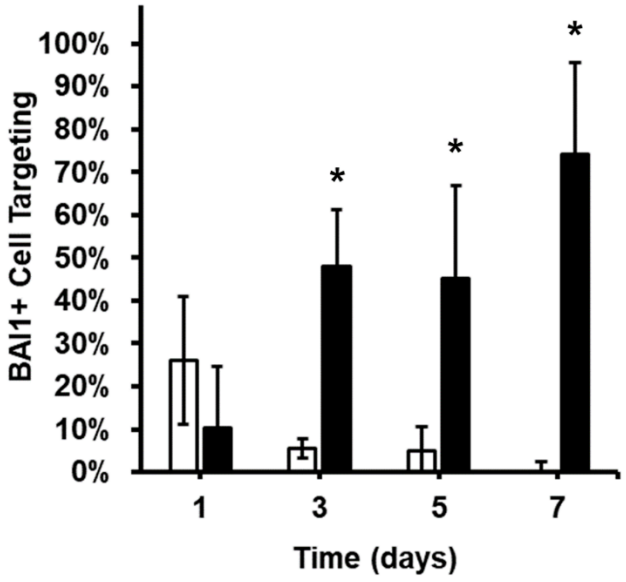

Figure 3.6. BAI1+ cell targeting in dynamic cell cultures. Cells were treated with G8:3DNA:Dox nanocarriers as a bolus (□) or with hydrogel (■) at t_0. The percentage of BAI1+ cells that were targeted were monitored every other day for 7 days. Significant differences are seen in targeting percentage between bolus and sustained release systems, denoted with an asterisk. ($p < 0.05$).

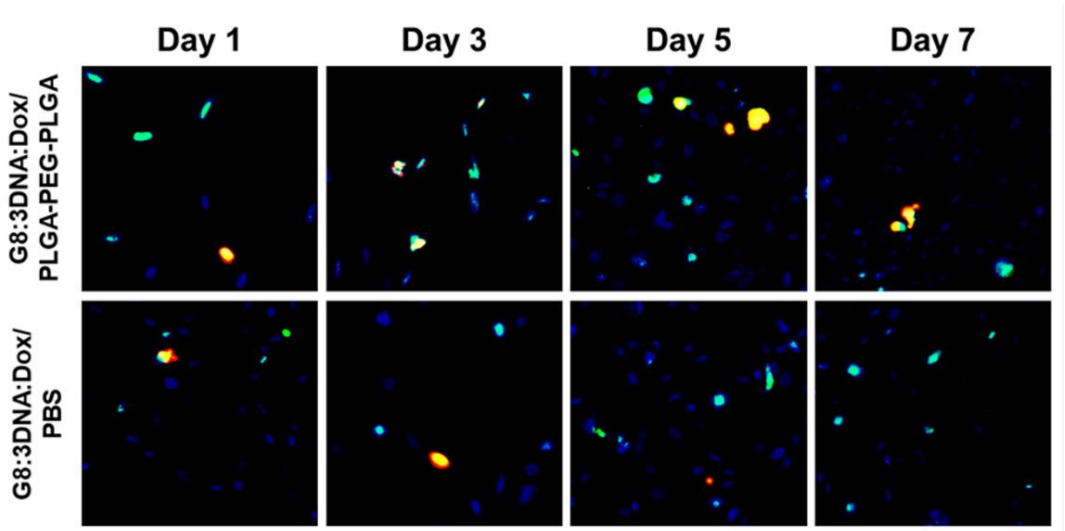

Figure 3.7. Specific targeting of BAI1+ cells over 7 days. Cells were treated with G8:3DNA:Dox nanocarriers in a sustained release hydrogel (G8:3DNA:Dox/PLGA-PEG-PLGA) or as a bolus injection (G8:3DNA:Dox/PBS). Cell nuclei (blue), dead cells (red), and BAI1+ cells (green) were stained. Targeted cells appear yellow due to colocalization of BAI1+ cells and dead cells (green + red). Nanocarriers given as a bolus show very little targeting after 7 days. Nanocarriers released from hydrogel continue to target BAI1+ cells at an increased rate over 7 days.

Chapter 4

Investigating the Nanoarchitectures of DNA Monolayers on Gold Surfaces

4.1 Introduction

Dendrimers represent a simple application of DNA nanocarrier technology driven by complementary base pairing and the careful design of single-stranded overhangs to facilitate branched nanostructures. Sequence selection and layer-by-layer assembly gives precise control over size and shape, multifunctionality, stability, and ability to conjugate functional units or load therapeutics.[233] Such structures provide an exquisite platform for the synthesis of versatile nanocarriers incorporating bioactive functionality such as sensitive biomolecule detection, high drug loading, and/or antibody display.[234] For site specific administration, dendritic DNA likely represents the most elegant solution for targeted delivery of therapeutics, as seen in the previous chapter. However, dendritic DNA nanostructures perform poorly in systemic circulation due to the physiological barriers of nucleic acids delivery including immune stimulation, poor stability, low transfection efficiency, and short biological half-life.[235–237]

The rational design of nucleic acid nanostructures can provide a similarly multifunctional template for drug delivery while also improving bioavailability and the capacity to overcome these physiological barriers. Specifically, spherical nucleic acid nanostructures (SNAs) have proven to be highly capable of withstanding the harsh conditions of systemic circulation. The most common form of spherical nucleic acid is formulated using a gold nanoparticle (AuNP) core. Gold is highly advantageous due to the precise control over the size and shape of AuNPs, optical properties that substantially assist imaging and detection for diagnostics, stability and bioinert nature, and its plethora

of therapeutic effects on several diseases.[238] Oligonucleotides can be self-assembled orthogonally about the AuNPs to form a biopolymer brush arrangement via modification of either the 3' or 5' terminal ends with an alkylthiol moiety. The addition of cations, or salt-aging, is used to screen the negative charges between neighboring DNA strands in order to increase the surface density significantly.[239] The steric density and local concentration of salt ions causes DNA-AuNPs to be extremely stable in physiological media, resistant to protein adhesion, show reduced immune response, and allows them to be efficiently internalized by cells without the need for additional transfection reagents. As a result, the DNA-AuNP nanocarrier presents itself as a highly effective vehicle for systemic delivery of drugs. However, the flexibility of NAs, the possibilities of intra- and inter-molecular interactions, and the poorly understood interactions of parallel DNA present a great mystery as to the nanoarchitecture of NA layers conjugated to gold.

In general, the NA layer conjugated to AuNPs can exist in either a flat, folded, coiled, or stretched state. It was hypothesized that by manipulating a DNA monolayer to adopt these different structures, the architecture can be exploited for controlled release of therapeutic drugs via restrictions to drug transport through the DNA layer. This chapter focuses on characterizing these different NA layers on gold and determines methods by which the nanoarchitectures can be controlled. To investigate the degree to which these layers can be manipulated, self-assembled DNA monolayers were formed on planar gold films and 15 nm AuNPs. The planar films were analyzed via quartz crystal microbalance with dissipation (QCM-D) and the AuNP layers were analyzed via dynamic light scattering (DLS).

4.2 Quartz Crystal Microbalance with Dissipation

4.2.1 Introduction and Theory

A quartz crystal microbalance (QCM) measures mass per unit area by detecting the change in frequency of a quartz crystal resonator, which is proportional to the thickness of the crystal and thus any adlayers conjugated thereto. It works based on the inverse piezoelectric effect, i.e., the application of voltage results in mechanical deformation of crystalline materials with certain symmetrical properties. An alternating current therefore leads to a cyclical or oscillatory deformation. By applying a voltage that matches the crystal's resonance frequency or multiples thereof (overtones), a standing wave is generated inside the crystal. Different oscillations will result depending on the cut of the crystal. QCM uses AT-cut crystals which vibrate in the thickness-shear mode with the two surfaces moving in an antiparallel fashion. Dissipation monitoring (QCM-D) allows one to measures the dampening of the shear wave as it propagates through the adsorbed layer and the bulk solvent. QCM-D operates via the "ring-down" technique where the voltage is intermittently turned off and the oscillations are allowed to decay. The decaying oscillations generate a voltage via the piezoelectric effect. Thus, QCM-D produces two parameters per overtone, the oscillation frequency (*f*, Hz) and the energy dissipation (D, unitless). For these purposes the quartz crystal must be coated by an electrode, which is commonly gold.

The induced oscillations in quartz crystals are exceptionally stable and sensitive to changes in adsorbed mass, hence their utilization as a microbalance (Figure 4.1). For thin, homogenous, rigidly coupled, and non-dissipative films, changes in the oscillation

frequency ($\triangle f$) show a linear relationship to the mass of the adlayer via equations derived by Sauerbrey[240]:

$$\Delta m = -C \cdot \frac{\Delta f}{n}$$

where $\triangle m$ is the change in areal mass density of the film, $\triangle f$ is the change in oscillating frequency, *n* is the overtone number, and C is the mass sensitivity constant (17.7 ng/(cm^2·Hz) for a 5MHz crystal). When the above assumptions are violated, which is usually the case of viscoelastic films or sufficiently thick films, the dissipation is necessary to characterize the adlayer. In these cases, a more intense mathematical model is necessary.

4.2.2 Viscoelastic Modeling

Biomolecular films, being generally highly hydrated polymers that exhibit viscoelastic properties, cause the Sauerbrey relationship to be invalid. Thus, a more advanced analysis is called for. The most appropriate connection between the measured parameters via QCM-D and the physical characteristics of a viscoelastic polymer film is achieved using a continuum mechanics approach. Most often this is done by fitting a Voigt model of viscoelastic films, represented by a purely viscous damper and purely elastic spring connected in parallel. The Voigt model has been derived for used on QCM-D results by Voinova et al,[241] and the relationship between QCM-D parameters and the viscoelastic characteristics of the film are given by the following equations:

$$\Delta f = -\frac{1}{2\pi\rho_o h_0}\left\{\frac{\eta_3}{\delta_3} + h_1\rho_1\omega - 2h_1\left(\frac{\eta_3}{\delta_3}\right)^2 \frac{\eta_1\omega^2}{\mu_1^2 + \omega^2\eta_1^2}\right\}$$

$$\Delta D = \frac{1}{\pi f \rho_0 h_0}\left\{\frac{\eta_3}{\delta_3} + 2h_1\left(\frac{\eta_3}{\delta_3}\right)^2 \frac{\eta_1\omega}{\mu_1^2 + \omega^2\eta_1^2}\right\}$$

Where ρ_0 and h_0 are the density and thickness of the crystal, η_3 is the viscosity of the bulk liquid, δ_3 is the viscous penetration depth of the shear wave in the bulk liquid, ρ_3 is the density of liquid, and ω is the angular frequency of the oscillation. Thus, the adlayer is described by four parameters: density (ρ_1), viscosity (η_1), shear elasticity (μ_1), and thickness (h_1). Using known values to describe the properties of the crystal and the bulk liquid, and subsequently measuring $\triangle f$ and $\triangle$D at multiple overtones, only one value, either layer thickness or density, must be independently verified or assumed in order to fit the equation. For DNA films, we use an assumed density of 1.06 g/cm^3. Therefore, via an iterative fitting of QCM-D parameters to the Voigt model relevant parameters about the thickness and viscoelastic character of bound nucleic acid layers can be extracted.

4.3 Dynamic Light Scattering

When a monochromatic beam of light encounters a solution of macromolecules, light scatters in all directions (Rayleigh scattering) depending on the size and shape of the molecules. The intensity fluctuations caused by Brownian motion in solution can be analyzed to calculate a diffusion coefficient (Dτ). Dynamic light scattering (DLS), also known as photon correlation spectroscopy, is a technique that relates this motion to the size of particles via the Stokes-Einstein equation:

$$D_\tau = \frac{k_B T}{6\pi\eta R_h}$$

where k_B is the Boltzmann coefficient, T is an absolute temperature, η is the viscosity of medium, and R_h is the hydrodynamic diameter of the molecule. Since large particles diffuse more slowly than small particles, this method allows for an accurate estimate of a range of particle sizes in solution. The most popular data analysis method known as

cumulant analysis provides mean values for the diffusion coefficient and thus determines a Gaussian-like distribution around the mean size values. For spherical particles, such as DNA-AuNPs, the mean values approximate very closely the actual size values of the particles.

4.4 Materials and Methods

4.4.1 QCM-D Preparation

All QCM-D experiments were performed on a Q-Sense analyzer from Q-Sense (Gothenberg, Sweden) using gold coated quartz crystal sensors. The sensors were pre-cleaned upon receipt and immediately after experiments and not used more than 4 times. Sensors and all tubing were thoroughly rinsed with 0.01% SDS. Then, sensors were cleaned in a UV/ozone chamber for 10 min, immersed in a base piranha solution (5:1:1 v/v water, H_2O_2 (30%), NH_4OH (30%)) at 75^oC for 5 min, dried using N_2, and cleaned again in a UZ/ozone chamber for 10 min. Baseline frequency and dissipation measurements were observed in air and water/phosphate buffer before starting experiments. Sample introduction was performed via manual syringe injection done slowly over the course of one minute using sufficient volume to ensure total buffer replacement in the sensor chamber.

4.4.2 DNA Oligonucleotide Preparation

Thiolated oligonucleotides were shipped lyophilized in their oxidized form and must be reduced before use. Oligonucleotide stocks were prepared in TE buffer (10 mM Tris-HCl, pH8.0 and 1 mM EDTA) at a 1 mM concentration. Stock solutions were mixed with 50 mM DTT in phosphate buffer (0.2 M, pH 7.4) for 3 hours. The reduced DNA mixtures were desalted using NAP-10 gravity-flow sephadex columns. Concentration of

DNA preparations was validated by their UV absorbance at 260 nm wavelength. All reduced DNA solutions were brought to working concentrations using deionized water or PBS. The hybridized dsDNA molecules were prepared by mixing equimolar amounts of each oligonucleotide and its complement at 80^{o}C for 10 min followed by slow cooling to room temperature. Sequences used were a single- and double-stranded sequence of 19 bp (ss19 and ds19, respectively) and a single-stranded sequence of 52 bp (ss52). They are shown in Table 4.1.

4.4.3 ssDNA and dsDNA Binding to QCM-D Sensors

A single-stranded, 19 nt DNA oligonucleotide and an identical double-stranded oligonucleotide with a 13 nt complement and 6 nt spacer tail (ss19 and ds19, respectively) were dissolved in water at concentrations from 0.3 to 4 µM. Samples were injected into QCM-D chambers after establishing a baseline in water and allowed to bind to the gold surface for one hour. The chamber was then washed with water to remove unbound material and left for a final baseline. Next, 0.3 µM solutions of each DNA oligonucleotide were mixed with NaCl from 0.2 to 1 M and immediately injected into chambers containing cleaned sensors in water. Oligonucleotides were again left to bind for one hour before washing with water.

4.4.4 Klenow Experiments on QCM-D

The ss19 strands was hybridized to the ss52 strand by mixing at 80^{o}C for 10 min followed by slow cooling to room temperature. The hybridized strand was bound to a clean QCM-D sensor in water and allowed to bind for one hour before washing with water. Next, the bound ss52 sequence was washed with 1X DNA polymerase buffer including free nucleotides (dNTPs) at a concentration of 33µM. To this solution 1µL of

Klenow enzyme was added (2 U/µL). The enzyme mixed with the oligonucleotide layer for 6 hours before being washed with water for a final baseline.

4.4.5 Dynamic Light Scattering Experiments

DLS was performed using a Malvern Zetasizer nano series Z-S90. Experiments were performed by loading AuNPs at a concentration of 4.7 x 10^{12} nanoparticles/mL into 1 cm^2 clear DLS cuvettes. Measurements were performed at 25^{o}C and done as cumulants analysis to provide a mean average intensity and estimate hydrodynamic diameter of particles in solution. Diameter ranges are given as % mean intensity.

4.4.6 Klenow Experiments on DNA-AuNP

AuNPs conjugated to ss19 DNA were hybridized with ss52 strands by mixing at 80^{o}C for 10 min followed by slow cooling to room temperature. The particles were resuspended in 1X DNA polymerase buffer including free nucleotides (dNTPs) at a concentration of 33µM. To this mixture 1µL of Klenow enzyme was added (2 U/µL). Samples from the reaction tube were extracted at certain time points, mixed with EDTA, and heated to 75^{o}C for 10 min to remove enzymatic activity. They were then centrifuged and resuspended in water. The resultant samples were loaded into a 2% agarose gel to investigate enzymatic activity over time.

4.5 Results

4.5.1 ssDNA and dsDNA Binding to Gold QCM-D Sensors

The modeled viscoelastic parameters from ss19 layers bound at increasing concentration is shown in Figure 4.2. The ss19 layer reaches its largest thickness at the lowest concentration of 0.3 µM. In this case, the thickness is 4.5 nm on average, equal to about 70% of the theoretical strand length. This indicates a relaxed, coiled layer of

upright ssDNA. The thickness then decreases in a non-linear fashion as the concentration increases. The lowest observed thickness of 1.3 nm occurs at a concentration of 3 μM, which would equate to an almost completely flat layer of ssDNA. The 4.5 nm ssDNA layer is also the stiffest, having a shear modulus value of 0.7 MPa. For the 1.3 nm (flat) layer, the shear modulus value is 0.05 MPa on average, and the softest layer observed. Viscosity estimates interestingly show a peak at 2 μM and a local minimum value of 1.4 mPas at 3 μM, with the average viscosity for all layers being 1.6 mPas.

The modeled viscoelastic parameters from ds19 layers bound at increasing concentration is shown in Figure 4.3. Again we see the largest thickness achieved at the lowest concentration. Here, the ds19 forms a layer about 5.5 nm thick, a full nanometer thicker than the ss19 layer at the same concentration. The ds19 layer also decreases in thickness as the concentration increases, although in this case the decrease is more linear ($R^2 = 0.978$). The lowest thickness observed is 1.1 nm at 4 μM, which is lower than the theoretical thickness of a flat dsDNA layer (2 nm), and thus suggests either denatured dsDNA or sparse surface coverage. Likewise, the estimates of shear modulus are decreased as concentration increases. The thickest, and also stiffest, layer has an estimated shear modulus of 0.29 MPa. Compared to the shear modulus of the same concentration of ssDNA (0.7 MPa), the ds19 layer is more than twice as soft. However, at the higher concentrations, where the dsDNA layer is lying flat, the resultant layers are more than twice as stiff as the flat ssDNA layers. Viscosity estimates remain similar for all concentrations of ds19 tested, averaging about 1.5 mPas, marginally lower than that for ss19 (1.6 mPas).

4.5.2 Effect of Salt Concentration on the Structure of ssDNA and dsDNA Monolayers

Addition of cations is known to increase the surface density of NA monolayers. This increase in surface density, when strands are oriented normal to the surface, results in a stretching or uncoiling of the NA layer. We see the same results in Figure 4.4. The ss19 layer increases in thickness with increasing NaCl concentration reaching the highest value of 7.5 nm at 0.4 M NaCl, which is more than one nanometer thicker than the theoretical strand length. At this concentration the shear modulus is estimated at about 0.4 MPa, which is softer than ss19 with no salt but stiffer than ds19 with no salt. Here also there is a local minimum in viscosity with a value of 1.2 mPas, suggesting a highly hydrated layer. The softest layer, with a shear modulus of 0.3 MPa , is observed at 0.2 M NaCl – here also we see an average thickness of 6.8 nm, which is only slightly thicker than the theoretical length, implying that the surface density is not stretching the strands significantly. Above 0.4 M NaCl the layer condenses and becomes less thick, with average shear modulus values of 0.35 MPa and viscosity of 2.1 mPas.

The effect of NaCl on ds19 layers is shown in Figure 4.5. The thickness of ds19 layers decreases with increasing NaCl until reaching its minimum of 1.2 nm at 0.6 M NaCl. Above this concentration the thickness increases again until reaching 3.8 nm at a concentration of 1 M NaCl. The shear modulus initially decreases at low salt concentrations and then reaches a maximum at 0.8 M NaCl with a value of 0.7 MPa. The viscosity decreases slightly at 0.4 and 0.6 M NaCl, but reaches its maximum also at 0.8 M NaCl with a value of 2.6 mPa s.

4.5.3 Klenow Activity on ss52 Immobilized on QCM-D Sensors

The activity of the Klenow enzyme on immobilized 52 bp DNA with a 39 bp overhang (ss52) is shown in Figure 4.6. The data are shown as the calculated viscoelastic parameters over time. The ss52 sequence rapidly binds to the sensor surface. After washing with Klenow buffer, including free dNTPs, the resultant layer is slightly over 10 nm thick. After the initial peak due to injection of the enzyme, no activity was observed for about 160 min, except for a small peak at about 380 min. Then, significant activity was observed for about 150 min. The activity ceased, and presumably the enzyme disassociated, before the final wash. The final values showed a layer thickness of about 16 nm, a shear modulus of < 0.1 MPa, and a viscosity of about 1.6 mPa s. This thickness is equivalent to about 85% of the theoretical strand length. The shear modulus is lower than results for ss19 DNA, indicating that the longer DNA presents a softer polymer. Additionally, the viscosity is in the range of 1.5 mPas seen for all other sequences thus far.

4.5.4 ssDNA and dsDNA Binding to Gold Nanoparticles

Both ss19 and ds19 oligonucleotides were self-assembled on 15 nm gold nanoparticles and salt-aged to NaCl concentration from 0 to 1 M. Resultant hydrodynamic particle diameter as measured by DLS is shown in Figure 4.7. Unmodified AuNPs showed an average diameter of 18.4 nm. AuNP-ss19, with the DNA bound without NaCl (0.0 M), resulted in an average diameter of 23.2 nm. This indicates that the ss19 layer on either side contributes only 2.4 nm of diameter to the particle, which is about 37% of the theoretical length of the strand, suggesting that the immobilized layer is folded to a significant degree about the nanoparticle surface. When binding ss19 in the

presence of NaCl, all concentrations showed nearly identical DLS profiles with an average diameter of 32.4 nm. In this case, the salt-aged ss19 layer on each side contributes 7 nm to the total particle diameter. This is about 0.5 nm longer than the theoretical strand length, implying that the ssDNA is slightly stretched.

AuNP-ds19 bound without NaCl results in nanoparticles with an average diameter of 36.4 nm. This implies a total contribution of 9 nm for each ds19 molecules, which is about 39% longer than the theoretical strand length. For dsDNA, this is surprising since it is much less capable of uncoiling and stretching compared to ssDNA. However, the increased averaged diameter is likely due to the wide peak which stretches over diameters of 100 nm, suggesting some particles are aggregating together and increasing the average diameter. Adding NaCl exacerbates this phenomenon, with the DLS profiles further stretching to larger particle diameters and subsequently raising the average diameter. Above 0.4 M NaCl, AuNP-ds19 particles aggregate irreversibly. Thus, it appears that ds19 lies upright on the particle surface but there are some unknown particle-particle interactions that result in aggregation, especially with the addition of salt.

4.5.5 Klenow Activity on DNA-AuNPs

The dynamic activity of the Klenow enzyme on ss52-AuNPs is shown in Figure 4.8. The addition of free nucleotides onto the 39 bp overhangs of ss52 are validated via observation of a mobility shift in the gel. The addition of the enzyme causes the particles to migrate more slowly through the gel as soon as one minute after mixing. The rate of mass addition increases for the first hour, where the total mass added begins to plateau. At 120 min, the activity has completely leveled stopped.

4.6 Discussion

Single stranded and double stranded DNA have significantly different mechanical properties and thus form distinct architectures when immobilized on surfaces. This difference is expressed in the persistence length of the oligonucleotides, which is less than 2 nm for ssDNA but around 50 nm for dsDNA.[242] In other word, ssDNA oligonucleotides of only 10 bp are flexible enough to form tight hairpins and loose, looping structures,[243] while dsDNA oligonucleotides of up to 150 bp act like rigid rods end tethered to the gold surface.[244] Additionally, oligonucleotides can interact with the gold surface via electrostatic interactions of the exposed nucleobases. This interaction is enhanced for ssDNA but is also observed for flat-oriented dsDNA oligonucleotides, and thus can explain why we observe layer thicknesses as low as 1.1 nm. Additionally, viscosity stays relatively constant, due in part to DNA having an intrinsic viscosity in the range of 1.5 to 2 mPas, and shear modulus varies between 0.1 and 0.7 MPa.

Polyelectrolyte polymers on surfaces form structures that can be sensitive to the ionic strength of the solution it is in. Thus, high concentrations of the polymer in solution may affect how the polymer organizes itself on the surface after immobilization. Indeed, previous work with proteins and cationic cubosomes have shown that increasing the concentration in solution above a certain point will actually start to decrease the total thickness of the immobilized layer, suggesting a structural change due to the higher solution concentration.[245,246] We see this behavior in two different ways from observing Figures 4.2 and 4.3. For ss19 (Figure 4.2), the viscoelastic properties of the layer vary non-monotonically with the solution concentration of oligonucleotides. Indeed, at the lowest concentration of 0.3 μM the layer appears to be the most organized, with rapid

binding kinetics and an average thickness closest to the theoretical strand length. Increasing the solution concentration leads to thinner layers, presumably due to the flattening of the immobilized DNA which can bind electrostatically to the gold via free nucleobases. The thickness actually increases at certain concentrations, e.g. at 2 and 4 μM, which occurs for unknown reasons but may be due to disorganized layer formation and a mixture of upright and flat strands. The ss19 layers also become softer and less viscous, on average, as the concentration increases, indicating a soft, hydrated film, which contrasts with the parallel, brush like film observed at the lowest concentration. Adding NaCl to the ss19 films will increase the surface density of bound ss19 strands, which upon washing reveals an increase in layer thickness as immobilized oligonucleotides are forced to stand upright or, in the case of 0.4M NaCl, stretch (Figure 4.4). Addition of NaCl causes ss19 layers to become slightly softer compared to the layer bound in water, likely due to the reduction in folded interactions with the gold surface. Viscosity increases as NaCl increases, although it reaches a minimum at 0.4 M NaCl when the layer is at its thickest. Therefore, binding ss19 DNA at a low concentration leads to a more organized, upright monolayer that is affected when the oligonucleotide concentration in solution is increased. When adding NaCl, and increasing the surface density of oligonucleotides, the individual strands become forced to stand upright and eventually stretch due to the negative repulsion from neighboring strands. At NaCl concentrations above 0.4 M NaCl, DNA is likely to condense significantly, so the structures of these layers are likely unorganized and form largely condensed and tortuous DNA networks.[247,248]

The ds19 layers shows substantially different binding kinetics. With increasing concentrations, the layer thickness decreases linearly (Figure 4.3). In this case, the dsDNA is similarly influenced by the oligonucleotide concentration in solution, but the rigidity of the dsDNA results in the formation of a more homogenous structure even when flattened. We again see that the layer becomes softer as the concentration is increased, indicating that an organized DNA polymer brush forms a more rigid monolayer compared to the flat layer. Viscosity does not change to any substantial degree when adding ds19 at different concentrations. In contrast to ss19, when adding NaCl the ds19 layer becomes less thick, likely due to the over-coiling of the DNA double helix. Additionally, even after washing, this coiling might be trapping NaCl and screening the negative charges on neighboring strands. At concentration above 0.6 M NaCl, the thickness begins to increase again. Additionally, at 0.8 M NaCl the peak in shear modulus and viscosity reveals some structural change occurring within the layer. It has been shown that inducing bends in a DNA duplex will increase the viscosity of the molecules.[249] As such, around 0.8 M NaCl we may be observing a bending of the DNA double helix, a behavior that could not occur without the salt acting as a condensing agent. Overall, the rigid structure of the dsDNA alters the way in which the DNA layer is flattened and also affects the influence of NaCl compared to ssDNA.

The resultant diameter of DNA-AuNPs also reveal some differences between the binding of ss- and ds-DNA. In both cases, immobilizing oligonucleotides to 15 nm gold nanoparticles with no salt results in the smallest particle diameter, reaching 23.2 nm and 36.4 nm respectively. For ss19 DNA, this indicates DNA folded about the gold surface. For ds19 DNA, this diameter is larger than the theoretical diameter, although evidence of

particle aggregation is present, presumably due to interactions between duplexes contacting in solution or due to increased contact of Au surfaces due to the lack of oligonucleotide folding. When salt-aging ss19-AuNPs a maximum diameter is reached of about 32.4 nm for all NaCl concentration, indicating that on AuNPs no further structural changes are occurring. A diameter of 32.4 nm is equivalent to a 7 nm increase on each side due to oligonucleotide binding, which is about 0.5 nm longer than the theoretical length. When salt-aging dsDNA-AuNPs, a smaller increase in average diameter is observed while the polydispersity grows, indicating more frequent particle aggregation. Indeed, above concentrations of 0.4 M NaCl particles in solution would irreversibly aggregate. Therefore, it is assumed that salt-aging dsDNA-AuNPs leads to increased inter-particle interactions, likely due to the organized, upright dsDNA layer and the increased coiling which reduces the electrostatic stabilization effect the DNA would have on the surface of AuNPs. For ssDNA-AuNPs, the inherent flexibility and smaller diameter of single stranded oligonucleotides instead leads to more densely packed monolayers that increase electrostatic stabilization and lead to a stretching of the DNA layer when resuspending in low ionic solutions.

Comparisons of Klenow activity on both planar gold and 15 nm AuNPs emphasizes the effect of surface curvature on the structure of the DNA layer. Previous work investigating Klenow activity on QCM-D used streptavidin/biotin interactions to produce well-spaced, organized DNA monolayers.[250] By binding the DNA directly to gold, we have a much denser DNA layer and thus the penetration of the enzyme is affected. The introduction of the enzyme to the DNA layer on QCM-D shows a clear response upon injection but no significant change is observed for about 160 min. After

this, an increase in activity occurs and lasts for about 150 minutes and can be seen in Figure 4.6. This activity is presumably the enzyme finally reaching the terminal ends of the immobilized DNA molecules to bind and begin filling in the overhang of the ss52 sequence. After 150 minutes the activity suddenly stops, likely due to the enzyme finishing its repair of the overhang DNA and disassociating. The end result of this activity is an increase in layer thickness of about 6 nm, a miniscule increase in layer rigidity, and an increase in the viscosity of the monolayer.

On DNA-AuNPs, the activity of the Klenow enzyme is much more rapid. By measuring the addition of mass via mobility through an agarose gel, it is seen that the enzyme begins to work in only a few minutes. The addition of mass stops after only 120 mins, after which a series of degraded products can be observed in the gel (Figure 4.8). This increase in the speed of enzymatic activity is attribute to the highly curved AuNP surface which increases the angle of deflection between neighboring DNA strands and therefore allows the enzyme to penetrate more easily. These results are significant regarding the enzymatic stability of these nanocarriers in physiological media.

4.7 Conclusions

The properties of spherical nucleic acids (SNAs) described in Chapter 2 suggest that these nanoparticle structures will play a significant role in formulating advanced and personalized nanomedicines. Exposure to physiological conditions can significantly affect the properties of biohybrid particles including structural and mechanical properties, elasticity, hydrophilicity, swelling, and degradation.[251–253] Clinically, this can lead to loss of biocompatibility, degradation, non-delivery of payloads, or reductions in the

performance. Thus, it is imperative to understand the unique properties of DNA monolayers on gold surfaces in physiological environments.

Nucleic acids are a unique polymer in which sequence, length, immobilization strategy, and state of hybridization can significantly affect structures and mechanical properties. On gold surfaces, ssDNA acts as a flexible chain capable of folding, coiling, looping, or adhering to the surface, and dsDNA acts as a rigid rod capable of standing upright or lying flat.[254] Addition of salt can screen negative charges and induce high density packing of ssDNA, which at sufficient densities can actually cause stretching of oligonucleotides. For dsDNA, the salt induces supercoiling of DNA double helixes and at high enough concentrations can induce strand bending. Additionally, the longer sequences present a much softer layer compared to the shorter sequences as revealed by the estimations of shear modulus. Thus, increasing the length of the oligonucleotide layer provides a thicker polymer network and a more mechanically deformable layer, which has implications for the tuning of nanocarrier properties in the future.

The structure of NA polymer layers is significantly affected by the curvature of the immobilizing surface. For example, the density of immobilized NAs increases exponentially as the size of AuNPs is reduced from 200 nm to 2 nm due to the extreme curvature inhibiting the electrostatic repulsion from neighboring strands.[255] We see here that this curvature also affects the activity of enzymes in penetrating the NA layer. On planar gold surfaces, the activity of the Klenow enzyme was delayed for over 2 h before polymerization began; in contrast, polymerization began almost immediately on DNA-AuNPs. This improved enzymatic access to the terminal ends of the immobilized

oligonucleotides holds great significance on the *in vivo* stability of administered NA nanocarriers.

The results in this chapter showed furthermore that the nanoarchitectures of NA layers on gold can be manipulated. By binding in low concentrations of salt and low NA concentrations, the induction of a folded NA layer is possible. Additionally, by immobilizing dsDNA or by salt-aging the ssDNA, the layer can be manipulated to stand upright in a brush formation. It was then questioned whether or not this manipulation could be exploited for controlled drug release. In the next chapter, it is shown that by directly manipulating the nanoarchitectures of DNA monolayers on 15 nm AuNPs the transport of a surface bound drug through the DNA polymer layer can be controlled.

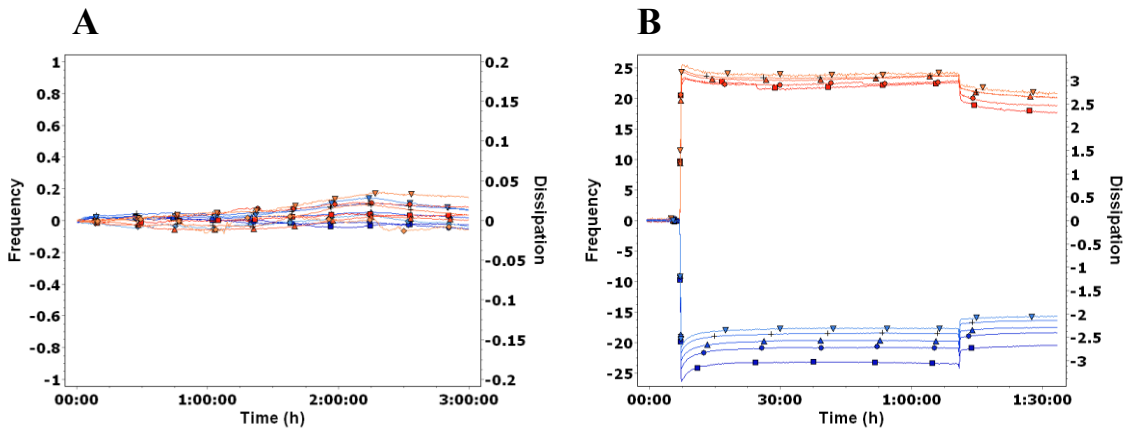

Figure 4.1. Typical QCM-D data generation. (**A**) Frequency and dissipation data at multiple overtones of a QCM-D sensors is shown oscillating in water over 3 hours. Over three hours the total frequency drift is less than 0.1 Hz and the dissipation drift is less than 0.04, indicating excellent stability. (**B**) A typical loading of a thiolated DNA monomer is shown for $\triangle f$ (blue, bottom) and $\triangle$D (red, top). The binding of the DNA causes a decrease in frequency and an increase in dissipation. After washing with buffer, unbound material is removed and the final values are attained.

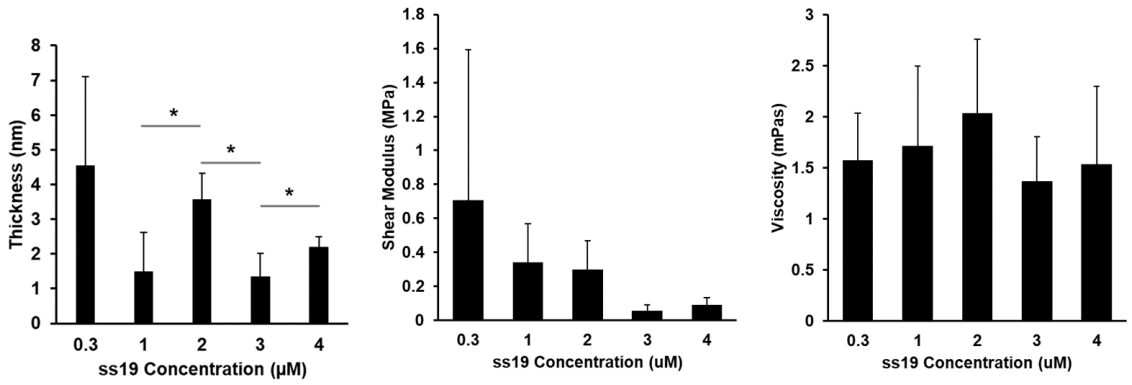

Figure 4.2. Modeled parameters of ss19 DNA bound to gold QCM-D sensors at increasing concentrations. Applying the Voigt viscoelastic model to QCM-D data reveals estimates of monolayer thickness, shear modulus, and viscosity. Significant differences are indicated by an asterisk (p-value < 0.05).

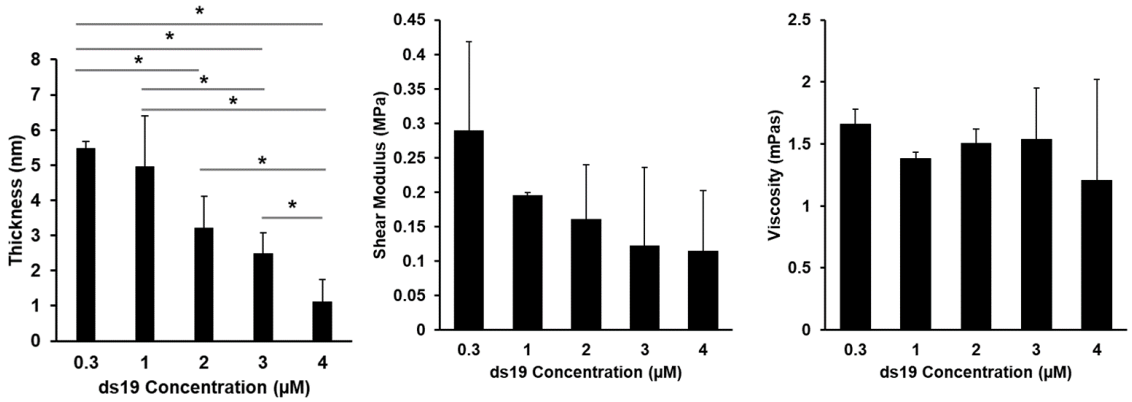

Figure 4.3. Modeled parameters of ds19 DNA bound to gold QCM-D sensors at increasing concentrations. Applying the Voigt viscoelastic model to QCM-D data reveals estimates of monolayer thickness, shear modulus, and viscosity. Significant differences are indicated by an asterisk (p-value < 0.05).

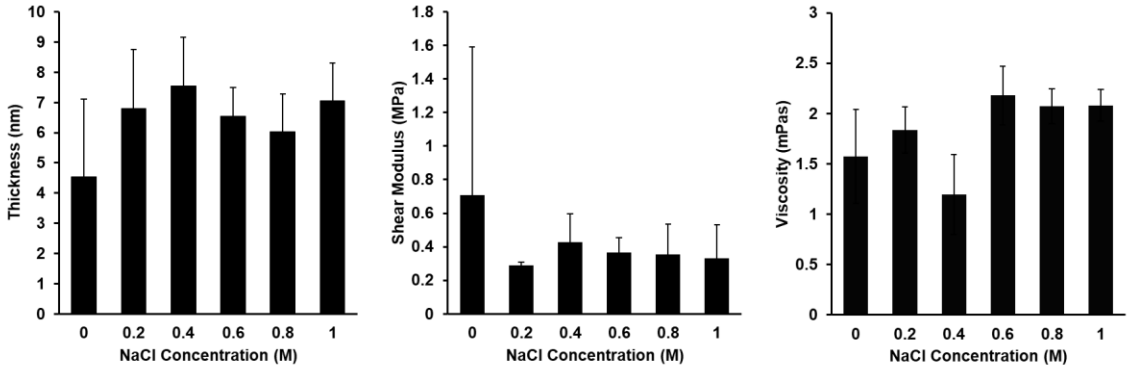

Figure 4.4. Modeled parameters of ss19 DNA bound to gold QCM-D sensors at 0.3 µM with increasing concentrations of NaCl. Applying the Voigt viscoelastic model to QCM-D data reveals estimates of monolayer thickness, shear modulus, and viscosity.

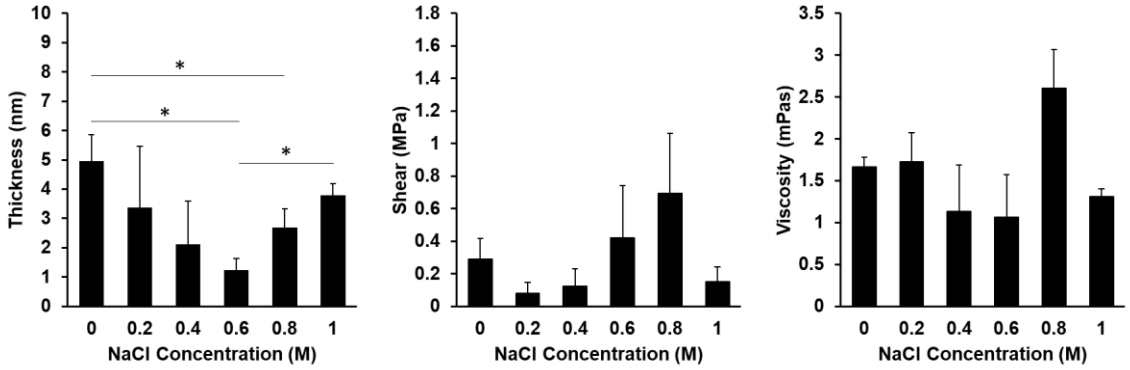

Figure 4.5. Modeled parameters of ds19 DNA bound to gold QCM-D sensors at 0.3 µM with increasing concentrations of NaCl. Applying the Voigt viscoelastic model to QCM-D data reveals estimates of monolayer thickness, shear modulus, and viscosity.

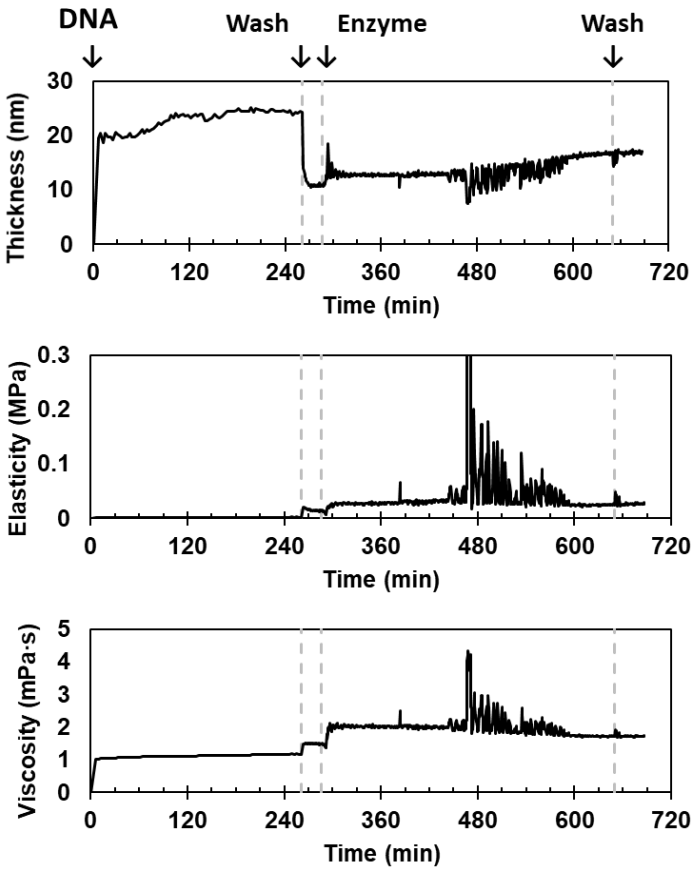

Figure 4.6. Klenow enzyme activity on DNA sequences with single-stranded overhangs on planar gold QCM-D sensor. DNA was immobilized and then unbound material was washed with Klenow reaction buffer. A spike in thickness is seen when the enzyme was injected, but no further activity was observed until about 460 minutes. The activity ceases before the final wash occurred.

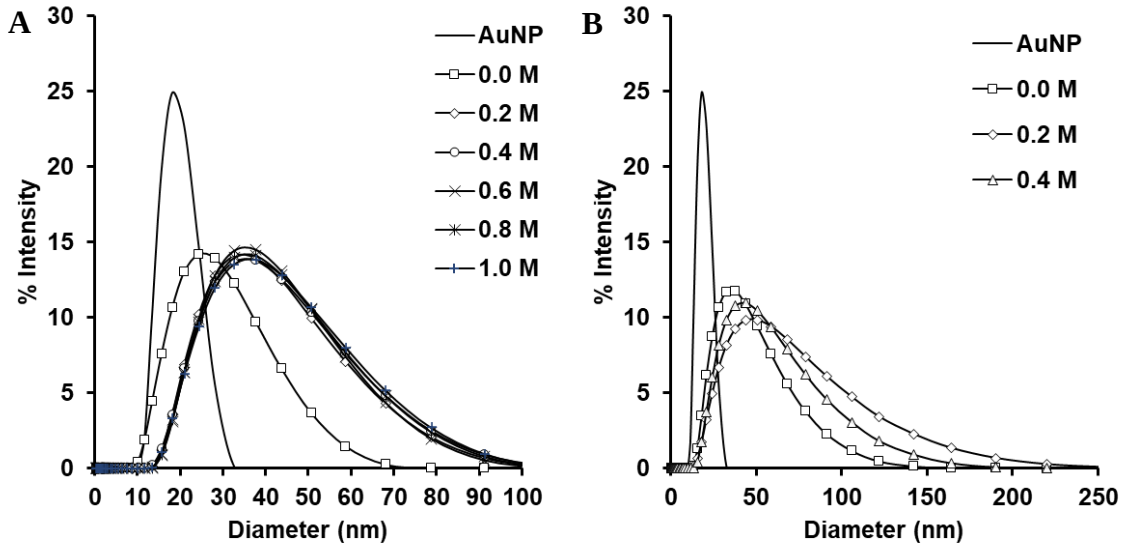

Figure 4.7. DLS results for the hydrodynamic diameter of DNA-AuNPs salt-aged to increasing concentrations of NaCl. Here ss19-AuNPs (**A**) and ds19-AuNPs (**B**) are shown. Unmodified AuNPs are shown as a solid black line. The legend indicates the final NaCl concentration during salt-aging. The ds19-AuNPs aggregated irreversibly at concentrations above 0.4 M.

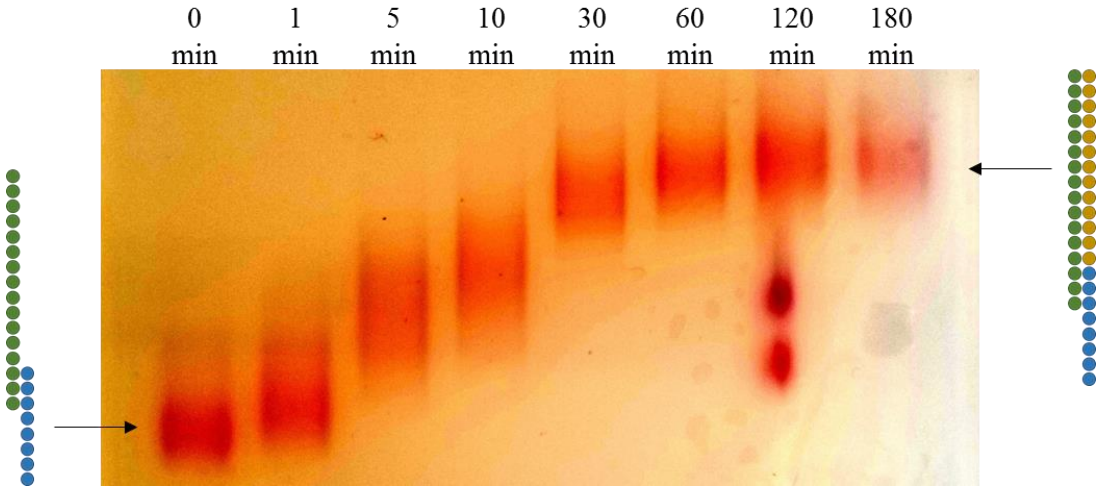

Figure 4.8. Klenow enzyme activity on DNA sequences with single-stranded overhangs on 15 nm AuNPs. Results are shown as mobility through a 2% agarose gel. AuNPs are visible in agarose to the naked eye and here contrast is increased slightly. Mass is added by the enzyme almost immediately and continues until about 60 min. After 120 min a series of degraded products are observable in the gel.

Table 4.1

DNA Sequences

	Sequence 5'→3'	Complement 3'→5'
ss19	TTTTATGGTTTACAATATT	N/A
ds19	TTTTATGGTTTACAATATT	CCAAATGTTATAA
ss52	TTTTATGGTTTACAATATT	CCAAATGTTATAAAGCAGCAGCAGCA GCAGCAGCAGCAGCAGCAGCAGC

Chapter 5

Tailored Nucleic Acid Architectures at Gold Surfaces for Controlled Therapeutic Release

5.1 Introduction

Nanoparticle drug delivery systems emerged out of a need for more effective ways of administering drugs to treat disease.[256] The precision of nanotechnology allows for construction of tailorable therapeutic vehicles, or nanocarriers, with highly controllable physiochemical properties. This control has resulted in positive treatment outcomes for many diseases including cancer due to the improved pharmacokinetics and pharmacodynamics of nanocarriers compared to drug alone.[23,257,258] The surface morphology of nanocarriers play significant role in the controlled delivery of therapeutics. For non-covalently bound drugs, the release occurs due to the diffusion gradient of drug molecules away from the nanocarrier and into the bulk solution.[259] The variables that affect drug release include a number of physiochemical properties such as material chemistry, surface roughness, uniformity, hydrophobicity, and interactions with therapeutic molecules.[260–262]

Nucleic acids are attractive nanomaterials due to their ease of controllable assembly, unique mechanical properties, stimuli responsiveness, and ability to deliver drug payloads.[263] Furthermore, nucleic acids can be used as building blocks for highly advanced, smart nanocarrier systems making them desirable in the creation of personalized therapeutics.[264–266] There are a number of ways to modulate DNA-based polymers for therapeutic release. For example, our work with DNA-capped gold nanoparticles (AuNPs) revealed controllable drug release from DNA layers via affinity modulation.[232,267] Unfortunately, the nanoscale architectures of DNA oligonucleotides at

surfaces are not well understood.[268,269] Single-stranded oligonucleotides (ssDNA) are a highly flexible polyelectrolyte biopolymer with a persistence length of only a few nanometers, while double-stranded oligonucleotides (dsDNA) are much more rigid with a persistence length of 50 nm.[242,270] This means that ssDNA may be folded over length scales of <10 nucleotides (nt) while dsDNA will remain rigid for up to 150 base pairs (bp). The differences in DNA molecule flexibility have been observed on surfaces under an applied electric field, where ssDNA is pulled to the surface segment by segment while dsDNA is flattened as a rigid rod.[254] When either covalently or noncovalently tethered to AuNPs, ssDNA can become folded and interact with the gold surface via exposed nucleobases or oriented perpendicular to the surface, with high binding densities leading to stretched layers of parallel oriented ssDNA due to the high concentration of negative charge.[271–273] On the other hand, rigid dsDNA oligonucleotides bind in an organized fashion and maintain conformational integrity on surfaces.[274]

Conformational changes of oligonucleotide layers can be exploited to achieve controllable drug release. On surfaces, nucleic acids can act as physical boundaries to the free diffusion of drug molecules, via a mechanism known as DNA-gated release. By capping the pores of porous nanoparticles with dsDNA, release of encapsulated drug by degradation of DNA duplexes can be triggered by temperature,[163,275–277] pH,[278,279] near-infrared light,[280,281] target recognition,[282] nucleases,[275] or UV light.[283] Taking into account our previous work and the multiple biological and medical applications of AuNP-DNA conjugates,[284] we hypothesized that a DNA-gated release could be achieved by modulating the surface architecture of DNA layers on 15 nm AuNPs. Dexamethasone (DXM) is a long-acting synthetic glucocorticoid steroid used to treat a number of

diseases due to its anti-inflammatory and immunosuppressive properties.[285–287] Recently it has been demonstrated that DXM can electrostatically interact with AuNPs via the fluorine atom and that the presence of negatively charged ligands (e.g. sodium 3-mercapto-1-propanesulfonate, or 3MPS) can slow the release of the drug from the AuNP surface.[288,289] In this study, we investigated the ability to sustain the release of DXM from novel nucleic acid nanoparticles via manipulation of the nucleic acid surface layer architecture to produce a DNA-gated controlled release mechanism without the need for triggered DNA degradation. Nucleic acid layers on planar gold surfaces and 15 nm AuNPs were assessed via quartz crystal microbalance with dissipation (QCM-D) and dynamic light scattering (DLS), respectively. We then compared the release of DXM from AuNP-DNA particles synthesized with DNA layers of varying architecture.

5.2 Materials and Methods

5.2.1 Materials

All DNA oligonucleotides were synthesized by IDT (Coralville, IA). Their sequences are listed in Table 5.1. Gold nanoparticles of 15 nm diameter were purchased from Ted Pella, Inc (Redding, CA). Dialysis tubes (MWCO 6-8 kDa) were from Millipore Sigma (Burlington, MA). Dexamethasone (DXM), PBS, NaCl, and all other reagents were obtained from VWR (Radnor, PA).

5.2.2 Preparation of Thiolated Oligonucleotides

Thiolated oligonucleotides were shipped lyophilized in their oxidized form and must be reduced before use. Oligonucleotide stocks were prepared in TE buffer (10 mM Tris-HCl, pH8.0 and 1 mM EDTA) at a 1 mM concentration. Stock solutions were mixed with 50 mM DTT in phosphate buffer (0.2 M, pH 7.4) for 3 hours. The reduced DNA

mixtures were desalted using NAP-10 gravity-flow sephadex columns. Concentration of DNA preparations was validated by their UV absorbance at 260 nm wavelength. All reduced DNA solutions were brought to working concentrations using deionized water. The hybridized dsDNA molecules were prepared by mixing equimolar amounts of each oligonucleotide and its complement at 80^{o}C for 10 min followed by slow cooling to room temperature.

5.2.3 Preparing Gold QCM-D Sensors

The following cleaning procedure was performed on gold-coated quartz sensors upon their receipt and immediately after each experiment: sensors and all tubing were thoroughly rinsed with 0.01% SDS. Then, sensors were cleaned in a UV/ozone chamber for 10 min, immersed in a base piranha solution (5:1:1 v/v water, H_2O_2 (30%), NH_4OH (30%)) at 75^{o}C for 5 min, dried using N_2, and cleaned again in a UZ/ozone chamber for 10 min. Baseline frequency and dissipation measurements were observed in air and water before starting experiments.

5.2.4 DNA Immobilization on QCM-D Sensors

Gold sensors were equilibrated in water at room temperature. DNA samples were injected into the QCMD chamber using a disposable 1 mL syringe. Injections were done slowly over the course of about one minute to avoid any pressure related effects. For experiments involving salt, NaCl was mixed with oligonucleotides immediately before injection into the chamber. The samples were allowed to equilibrate for at least one hour before washing with 1 mL of water.

5.2.5 Viscoelastic Modeling

Data modeling was performed using the QTools software package included with the instrument (Q-Sense Analyzer, Biolin Scientific). In QTools, the Δf and ΔD data are related to viscoelastic properties of the DNA layers using a Kelvin-Voigt model according to the research of Voinova et al.[241] The following equations were used:

$$\Delta f \approx -\frac{1}{2\pi\rho_0 h_0}\left\{\frac{\eta_3}{\delta_3} + h_1\rho_1\omega - 2h_1\left(\frac{\eta_3}{\delta_3}\right)2\frac{\eta_1\omega^2}{\mu_1^2+\omega^2\eta_1^2}\right\}$$

$$\Delta D \approx \frac{1}{\pi f p_0 h_0}\left\{\frac{\eta_3}{\delta_3} + 2h_1\left(\frac{\eta_3}{\delta_3}\right)^2\frac{\eta_1\omega}{\mu_1^2+\omega^2\eta_1^2}\right\}$$

where ρ_0 and h_0 are the density and thickness of the crystal, η_3 is the viscosity of the bulk liquid, δ_3 is the viscous penetration depth of the shear wave in the bulk liquid, and ρ_3 is the density of liquid, and ω is the angular frequency of the oscillation. The adsorbed DNA layer is characterized by density (ρ_1), viscosity (η_1), shear elasticity (μ_1), and thickness (δ_1). Before each experiment, the instrument was baselined and washed with pure water, giving a fluid viscosity of 0.001 kg/m^3 and fluid density of 1000 kg/m^3. The effective density of the DNA was assumed to be 1.06 g/cm^3.[290]

5.2.6 Preparation of Nanocarriers

Nanocarriers were prepared by mixing 50 µL of reduced, thiolated DNA stock (4 µM) with 1 mL of 15 nm AuNPs (1.4x10^{14} particles/mL) overnight. The mixture was then brought to 50 mM phosphate using 2M phosphate buffer. Salt-aging was done by slowly adding a 5 M NaCl solution drop wise over the course of a few hours to the final concentration of 0.4 M NaCl. Nanocarriers were centrifuged for 30 min at 13,200 rpm, three times, and resuspended in PBS. The final product was characterized via DLS using a Malvern ZS90 Nano series zetasizer at 25^{o}C with an AuNP concentration of 4.7 x 10^{12} particles/mL.

5.2.7 Drug Loading and Release

We mixed nanocarriers with DXM (1 mg/mL in 50% ethanol) at a weight ratio of 5:1 Au:DXM and vortexed for 4 hours, according to previous studies.[288,289] Nanocarriers were washed three times with PBS, recovered by centrifugation and resuspended in 0.01 M PBS. AuNP concentration was determined via absorbance at 520 nm. Equivalent concentrations of DXM loaded nanocarriers were aliquoted into dialysis membrane tubes and submerged in PBS at 37°C. Aliquots of release media were collected and DXM was detected by measuring UV absorbance at 241 nm and comparing to a standard curve. Cumulative release percentage was calculated using the ratio of DXM mass released at time *t* and the total DXM mass released over the course of the experiment (M_t/M_∞).

5.2.8 Statistical Analysis

Best fit lines of drug release data were obtained by modeling as a first order release. Statistical significance was calculated via Student's t-test with a p-value of < 0.05 considered significant. All data are shown as averages +/- standard deviation.

5.3 Results

Oligonucleotides were first immobilized on gold QCM-D sensors to estimate layer thickness. Observed energy dissipation from the bound layer prevents accurate calculation of bound mass via the Sauerbrey equation, and thus the Kelvin-Voigt model was necessary to estimate thickness. Note that for modeling purposes we assumed constant density of the DNA layer in all experiments. The thickness of ss19 and ds19 monolayers, including a ss19 bound in the presence of 0.4 M NaCl, on gold surfaces is shown in Figure 5.1. In our earlier studies we found that maximum DNA loading on AuNPs is achieved at a DNA concentration of 4 μM and 0.4 M NaCl.[232] On QCM-D

sensors, ss19 layers and ss19 layers bound in 0.4 M NaCl resulted in layer thicknesses of 4.5±2.5 nm and 7.5±1.63 nm, respectively, which is equivalent to 69% and 115%, respectively, of the theoretical sequence length. For ds19 bound without salt we see and average layer thickness of 5.5±0.2 nm, which is equivalent to 85% of the theoretical strand length. The effect of hybridization was also investigated using longer, 52 bp sequences. These results on QCM-D are shown in Figure 5.2. The ss52 strand forms a layer with thickness of 4.6±2.5 nm. This observation suggests that over 75% of the ssDNA strand is folded over onto the gold surface. Sequence ds52 however forms a layer of 18 nm, equivalent to 91% of the theoretical sequence length. Thus, ssDNA immobilized without the presence of salt forms a highly folded monolayer on the gold surface.

DLS profiles of the hydrodynamic particle diameter of 15 nm AuNPs conjugated to ss19 and ds19 oligonucleotides is show in Figure 5.3. Since the particles formed are spherical, this represents an accurate estimation of particle size. Additionally, the presence of particle aggregation can be confirmed or denied via observation of absorbance profiles around a wavelength of 520 nm for a 15 nm AuNP. Thus, the changes in diameter observed here represent only addition of spherical NA monolayers.

Unmodified AuNPs showed an average diameter of 18.4 nm, with a relatively sharp peak indicating a highly monodisperse sample. Conjugation of DNA induces an increase in diameter with a simultaneous increase in polydispersity. AuNP-ss19 with no NaCl had an average diameter of 23.2 nm, suggesting the ss19 layer on either side only contributes 2.45 nm, which is 38% of the theoretical sequence length. This result implies that the ss19 molecules are highly folded about the AuNP surface. AuNP-ss19 (0.4M

NaCl) and AuNP-ds19 show similar results to each other, with average diameters of 32.4 nm and 36.4 nm, respectively. This is equivalent to a single oligonucleotide contribution of 7 nm and 9 nm, respectively, or 108% and 138% of the theoretical sequence length. We observe here that the AuNP-ss19 salt-aged to 0.4 M NaCl again cause the immobilized sequences to stretch longer than their theoretical length. The AuNP-ds19 layer appears to be even more greatly stretched, which is unexpected; however, the DLS profile also indicates higher polydispersity which may be increasing the average diameter estimate.

The hydrodynamic diameter of AuNPs conjugated with ss52 or ds52 oligonucleotides is shown in Figure 5.4. AuNP-ss52 forms with an average diameter of 34.5nm, which is larger than AuNP-ss19 (23.2 nm) but smaller than AuNP-ds19 (36.4 nm). This indicates a contribution from ss52 oligonucleotides of 8.1 nm, or less than half of the total strand length, suggesting a significant amount of oligonucleotide folding. AuNP-ds52 forms a particle of average diameter 74.5nm, which suggests an oligonucleotide layer thickness 150% of the theoretical size. However, we again see an increase in polydispersity with these particles which skews the average. A large fraction of particles do match the theoretical diameter of 57.8nm. Therefore, we see a significant amount of folding within DNA monolayers formed with ssDNA while layers formed with dsDNA - or salt-aged ssDNA - present a much more organized, upright-oriented layer.

We then investigated the influence that these distinct DNA layer structures had on the release of a surface bound drug. The results for DXM release from AuNP-ss19, formed in either 0 or 0.4 M NaCl, and AuNP-ds19 into PBS at 37^{o}C are shown in Figure 5.5. Calculated release rate constants are given in Table 5.2. AuNP-ss19, bound without

salt, releases DXM at the slowest rate and continues to release the drug for 192 h with a release rate constant $k = 0.014$ ($R^2 = 0.99$). When salt-aged to 0.4M NaCl, where the ss19 showed evidence that the layer was upright and even stretched, the release rate is fastest with complete fractional release reached in about 96 h and a rate constant $k = 0.157$ ($R^2 = 0.97$). The release rate for AuNP-ds19 is only slightly lower than that of AuNP-ss19 in 0.4 M NaCl. AuNP-ds19 releases DXM for between 96-120 h with a release rate constant $k = 0.138$ ($R^2 = 0.94$).

The release of DXM from AuNPs conjugated with 52 bp DNA sequences are shown in Figure 5.6. Calculated release rate constants are given in Table 5.2. AuNP-ds52 releases all of the bound drug in about 600 h with release rate constant $k = 0.004$ ($R^2 = 0.97$), while AuNP-ss52 continues to release for about 800 h with release rate constant $k = 0.002$ ($R^2 = 0.97$). The difference in release rates between 19 and 52 bp sequences (Figure 5.5 and 5.6, respectively) is striking, with nearly a 4-fold reduction in release rate. Additionally, the magnitude of changes in release rate between ssDNA and dsDNA are different at length scales of 19bp and 52 bp. The release rate of DXM from AuNP-ds19 is almost 10-fold greater than that of AuNP-ss19. However, for AuNP-ds52 it is only twice as fast compared to AuNP-ss52. Thus, the effect of inducing an upright NA orientation has lees of an influence on drug release rate as the thickness of the layer increases.

5.4 Discussion

This work shows that the transport of a surface-bound drug through a DNA monolayer conjugated to an AuNP can be controlled via manipulation of the size and structure of the DNA layer (Figure 5.7). The DNA layer structures were validated using

QCM-D and DLS. The utilization of QCM-D allows one to determine the structure of a polymer film *in situ* by modeling viscoelastic parameters from the frequency and dissipation data. To do this, we had to assume a constant density of the DNA polymer. It is known that the true density of the layer must lie somewhere between that of water and the density of pure DNA (1.43-1.7 g/cm^3).[291] On 15 nm AuNPs under optimized conditions, short oligonucleotides were found to bind at a maximum of about 1.4x10^{13} molecules/cm^2,[232] while optimized binding of duplexes on planar surfaces resulted in about 3.4x10^{12} molecules/cm^2.[274] Previous reports utilizing QCM-D and SPR found that the grafting density of oligonucleotide layers was approximately 1.06 g/cm^3,[290] which would agree with surface density in the range of 1-3 (x10^{12}) molecules/cm^2. Therefore, this density value (1.06 g/cm^3) was utilized for all Kelvin-Voigt modeling in this work.

A perfectly organized, upright monolayer of DNA should produce an estimate thickness approaching the theoretical length of the sequence. Additionally, an upright sequence should have an identical thickness whether it is ssDNA or dsDNA. On QCM-D, in all cases the thickness of the layer was less than the theoretical length. For dsDNA, the 52 bp strand was closer to the theoretical length (91%) than the 19 bp strand (85%). This may be due to the ability of the shorter strand to lie flat on the gold surface (Figure 4.3), whereas the longer sequence is unable to lie flat in a similar way. The ss52 sequence, which is almost 3-fold larger than ss19, results in a layer thickness only marginally larger than the ss19 layer. This suggests that a large majority of the sequence is folded over the gold surface. Since this is a larger sequence, this represents a highly folded and dense network of DNA. The ss19 layer bound in 0.4 M NaCl results in an apparent stretching of the immobilized strands, leading to a thickness greater than the theoretical sequence

length. Thus, this shows evidence that the salt-aged layer is forming an upright monolayer similar to that seen with the dsDNA.

DLS experiments on DNA-AuNPs show similar behavior. Both AuNP-ss19 and AuNP-ss52 show average diameter measurements that are smaller than expected using the theoretical sequence lengths. Thus, the DNA must be folding about the AuNP surface. For the AuNP-ss19 salt-aged to 0.4 M NaCl, the resultant diameter indicates DNA sequences of 7 nm in length, which is larger than the theoretical length and suggests a stretched monolayer which would be oriented upright. The dsDNA layers both appear larger than expected from theoretical sequence lengths. This is not likely due to stretching as dsDNA is unable to stretch beyond a few nanometers. However, a significant increase in polydispersity is observed form the graphs, and this is likely causing the increase ein average diameter. For both AuNP-ds19 and AuNP-ds52, a significant fraction of particles forms around the theoretical diameters.

The mechanism behind 0.4M NaCl achieving maximum DNA loading is as of yet undetermined. In separate experiments involving salt-aging dsDNA on AuNPs, we found that concentrations of 0.6M NaCl and above would cause AuNPs to aggregate irreversibly, presumably due to an extreme coiling of dsDNA duplexes that allows for AuNP surfaces to come into close contact with one another. We hypothesize that by electrostatically shielding the negatively charged DNA backbone, increasing NaCl concentration induces dense packing of DNA up to a critical level after which the DNA is highly condensed by a high local concentration of positively charged ions. Thus, 0.4M NaCl may constitute a critical salt concentration for achieving the highest DNA loading without inducing condensation or aggregation.

DXM is not an intercalating drug and therefore will not bind directly to DNA. Therefore, the only mechanism to control the drug transport would be excluded volume and steric hindrance. This hindrance can occur via both the presence of the DNA chains in the diffusion path and the presence of negative charges along the DNA backbone (zeta potential -30mV for similar sized sequences on 15nm AuNPs[292]), which presents a barrier significantly larger than the crystal diameter of DNA. Thus, the unique, controllable layer architectures adopted by ss- and ds-DNA immobilized under certain conditions acts as the main mechanism for controlled release. Binding the ss19 strand onto gold surfaces in the absence of salt resulted in monolayers that were lower than the theoretical sequence length, implying that the DNA adopts a folded orientation. When binding in 0.4M NaCl, ss19 layers form that are at or slightly larger than our theoretical strand length, suggesting an upright orientation. This orientation is reflected in the release data, where DXM releases more quickly from the AuNP-ss19 0.4M NaCl platforms than from AuNP-ss19 formed in the absence of salt (Figure 5.4). The AuNP-ds19 releases drug marginally slower than AuNP-ss19 0.4 M NaCl; this may in fact be due to the presence of hybridized duplexes which are upright but still take up more space than ssDNA. Furthermore, AuNP-ss52 releases drug at an even slower rate, presumably due to the increased folding the longer ssDNA undergoes on the gold surface (Figure 5.5).

The reduction in release rate observed with increasing DNA sequence length is likely due to the increase in physical space taken up by the longer molecules and the subsequent increase in negative charges along the longer DNA backbone, which continues to hinder the diffusion of the drug and prevents it from entering solution. AuNP-ss52, having a highly folded or coiled structure, has the slowest release rate of all

platforms tested, suggesting that this architecture combined with the increased length slows the release of the drug further. AuNP-ds52, which remains rigid at this length scale, releases drug more quickly by comparison due to the upright nature of the bound DNA. However, both sequences at this length release drug more slowly compared to 19 bp sequences, indicating that the length of the sequence affects the release rate regardless of layer architecture. Notably, the difference in drug release rates between ss- and ds-DNA layers is greater for the shorter sequences than it is for the larger sequences, suggesting a slower relative release rate for dsDNA as the sequence length increases (Table 5.2). Thus, it appears that at shorter sequence lengths, the effect of DNA architecture on drug release rate is more prominent. For longer sequences, the increase in DNA density even with upright layers still appears to slow the release rate of the drug.

5.5 Conclusions

SNA platforms will outperform many DNA nanostructures with regard to drug delivery and systemic administration, however controlling the release of drugs from such platforms is difficult. In this work we showed that tailoring nucleic acid architectures on gold surfaces can be used to achieve controlled, DNA-gated release of bound molecules. It was shown that the binding of oligonucleotides to gold involves complex binding behaviors based on the inherent flexibility or rigidity of ss- and ds-DNA. Single-stranded oligonucleotides at low surface densities are free to randomly coil and fold over onto the gold surface. We were able to manipulate the surface architecture of DNA oligonucleotides by immobilizing in the presence of salt or by hybridizing oligonucleotides to form double-stranded duplexes, both of which appear to encourage upright, organized DNA monolayers. By conjugating oligonucleotides to AuNPs and

investigating the layer architecture, it was observed that upright oriented layers allow for a faster diffusion of the drug into solution. This is presumably due to the physical and electrostatic barrier the DNA presents to the diffusion drug molecules, which is reduced with upright oriented architectures. At longer sequence lengths, this effect is less pronounced. It is hypothesized that as the sequence length increases, the high density of DNA presents a diffusion barrier even for upright DNA layers.

We investigated DNA sequences of two different lengths, either ssDNA or dsDNA, and two distinct gold surfaces, planar gold and highly curved 15 nm AuNPs. Therefore, a wide range of parameters remains unstudied, including the role of surface curvature in DNA layer architecture and thus the release profiles of the drug.[255] A more thorough application of molecular simulations and mathematical drug release models would speed up the elucidation of key parameters involved in the controlled release of the drug.[293–296] This approach would lead to optimization of the nanocarriers for drug delivery. Additionally, the potential for triggering the release of drug via introduction of complementary sequences to ssDNA layers presents a very interesting concept. Such approaches highlight the potential of this novel controlled release mechanism.

We used DXM as a template molecule owing to its electrostatic interaction with the gold surface. As such we expect that this platform could be extended for the sustained release of a wide variety of molecules, including other fluorinated corticosteroids or surface bound therapeutics, including proteins.[297] The programmable nature of DNA nanostructures also provides an avenue toward selective targeting or triggered release mechanisms, adding to the multifunctionality of this nanocarrier. In the future, we

envision highly effective dual release nanocarriers that have sustained release from intercalated and surface bound therapeutics using a single, personalized platform.

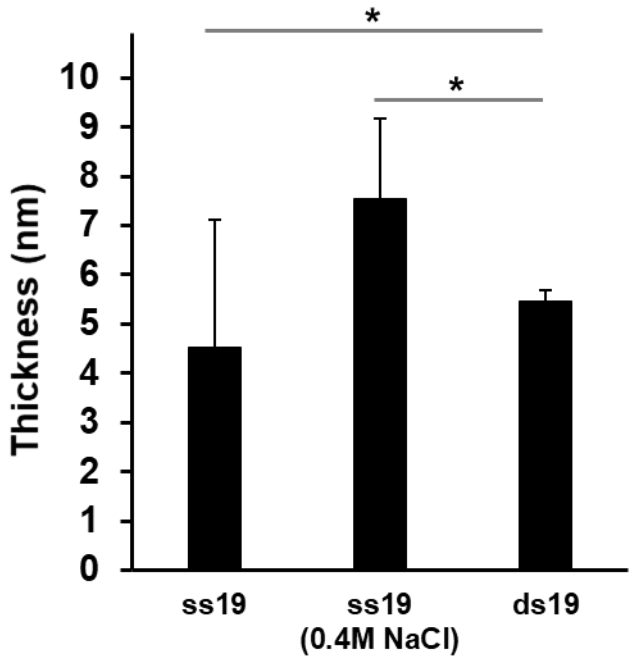

Figure 5.1. Thickness of 19 bp DNA layers on planar gold sensors. The theoretical sequence length is 6.5 nm. The ss19 and ds19 layers are less thick than the theoretical length; in the case of ss19, it is 2 nm less than expected, suggesting some oligonucleotide folding. For ss19 salt-aged to 0.4 M NaCl, the layer appears larger than the theoretical length, indicating a stretched oligonucleotide layer. Significant differences are indicated by an asterisk (p-value < 0.05).

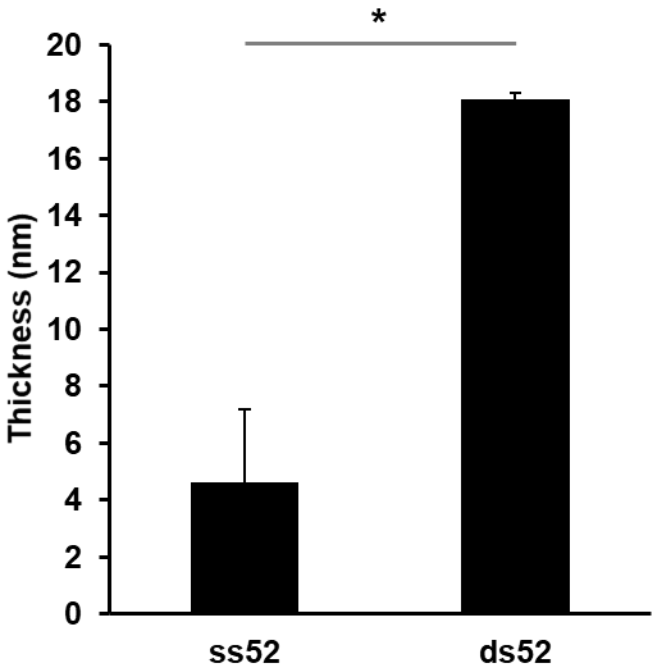

Figure 5.2. Thickness of 52 bp DNA layers on planar gold sensors. The theoretical sequence length is 19.7 nm. The ds52 sequence forms slightly under this length, suggesting an upright monolayer. The ss52 sequence, however, appears to form a highly folded nucleic acid monolayer. Significant differences are indicated by an asterisk (p-value < 0.05).

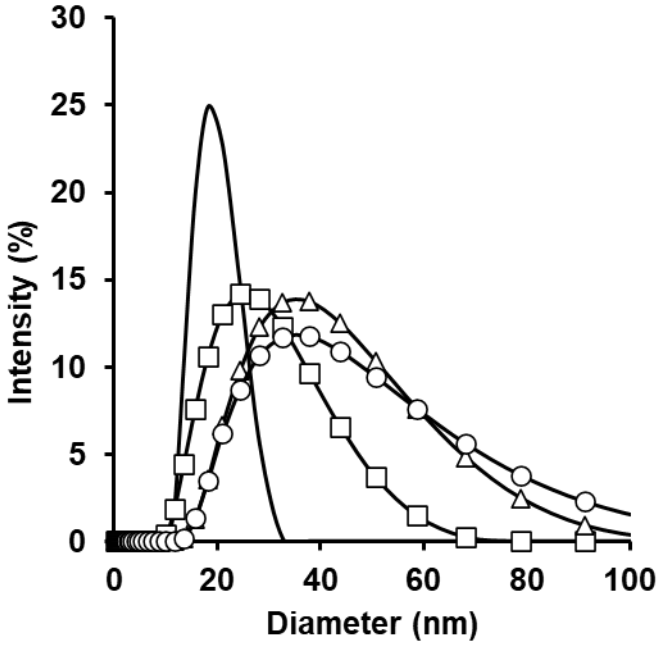

Figure 5.3. Hydrodynamic diameter of 19 bp DNA-AuNPs. Unmodified AuNP (−), AuNP-ss19 (□), AuNP-ss19 salt-aged to 0.4 M NaCl (△), AuNP-ds19 (○).

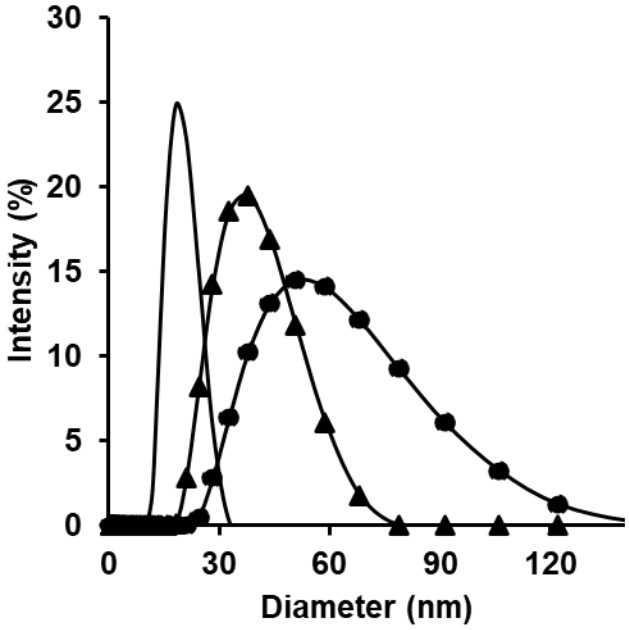

Figure 5.4. Hydrodynamic diameter of 52 bp DNA-AuNPs. Unmodified AuNP (−), AuNP-ss52 (▲), AuNP-ds52 (●).

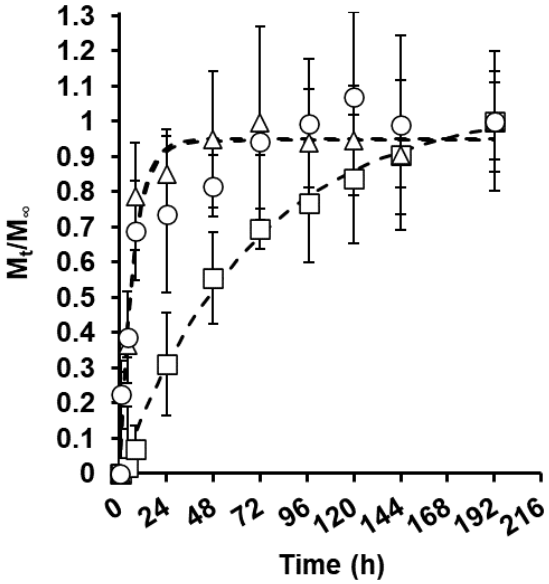

Figure 5.5. Release of DXM from 19 bp DNA-AuNPs. AuNP-ss19 (□), AuNP-ss19 salt-aged to 0.4 M NaCl (△), AuNP-ds19 (○).

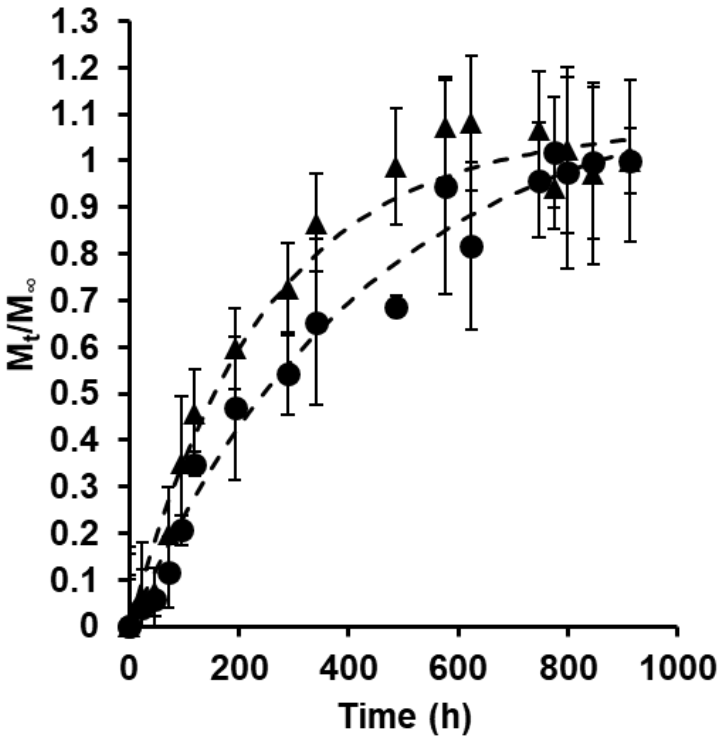

Figure 5.6. Release of DXM from 52 bp DNA-AuNPs. AuNP-ss52 (●), AuNP-ds52 (▲).

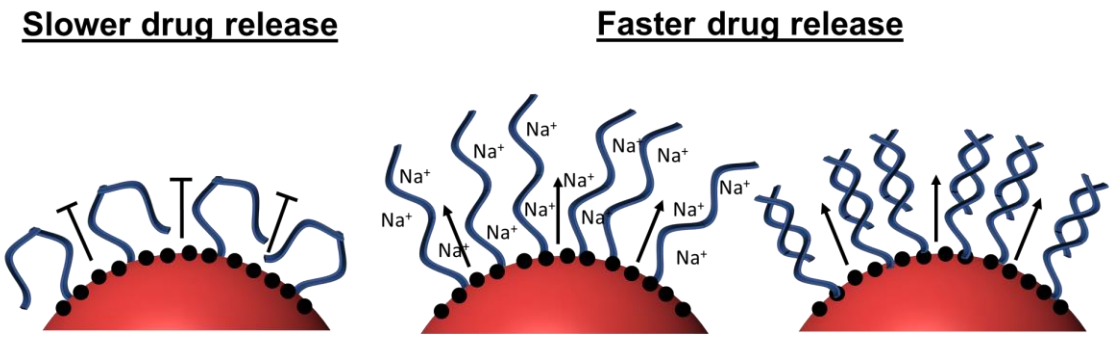

Figure 5.7. Schematic representation of a novel mechanism of controlled therapeutic release. The folded nucleic acid orientation presents a steric and electrostatic hindrance to drug transport thus slowing the release. An upright orientation, however, allows for a more rapid release of the drug.

Table 5.1

DNA Sequences

	Sequence 5'→3'	Complement 3'→5'
ss19	TTTTATGGTTTACAATATT	N/A
ds19	TTTTATGGTTTACAATATT	CCAAATGTTATAA
ss52	TTTTATGGTTTACAATATT	CCAAATGTTATAAAGCAGCAGCAGCA GCAGCAGCAGCAGCAGCAGCAGCAGC
ds52	TTTTATGGTTTACAATATTTCGTCGTCGT CGTCGTCGTCGTCGTCGTCGTCGTCGTCG	CCAAATGTTATAAAGCAGCAGCAGCA GCAGCAGCAGCAGCAGCAGCAGCAGC

Table 5.2

Release Rate Constants

	k	R^2
AuNP-ss19	0.014	0.99
AuNP-ss19 (0.4M NaCl)	0.157	0.97
AuNP-ds19	0.138	0.94
AuNP-ss52	0.002	0.97
AuNP-ds52	0.004	0.97

Chapter 6

Near Zero-Order Release of Daunomycin from Engineered Nucleic Acid Monolayers

6.1 Introduction

Cancer represents a major public health crisis worldwide. Certain cancers, such as pancreatic, liver, and non-small cell lung cancer, remain extremely deadly while generally treatable cancers, such as breast cancer, result in significant risk of mortality if not diagnosed early and allowed to metastasize.[1] Many chemotherapeutic drugs have been developed to target cancerous tissue but they often produce prohibitive side effects.[2] Advances in molecular biology and tumor physiology have revealed that a tailored and personalized approach is capable of significantly improving outcomes for patients.[3] Furthermore, driven by the emergence of nanomedicine, delivery systems for drug combinations have arisen as an exciting strategy for both personalizing treatment and carrying drugs for targeted delivery to tumor sites.

The tunable properties expressed at the nano-scale have been exploited for the treatment of many pressing medical issues with varying results.[4–6] Cancer in particular has seen a profound impact due to the development of a variety therapeutic agents designed with molecular precision for the treatment of specific cancer genotypes.[7] Drugs modified for specific delivery, such as antibody-drug conjugates (ADCs), have grown in popularity but suffer from small payloads, low avidity of ligand binding, and the emergence of drug resistance.[8–10] Utilizing a nanocarrier for payload delivery, however, has distinct advantages including diverse payloads, high drug-to-targeting-ligand ratio, multivalency, and controlled drug release.[11] Nanocarriers can be modulated and tailored

separate from the drug payload for use in a wide variety of applications. Therefore, rationally designed nanocarriers present an outstanding opportunity for the delivery of chemotherapeutics.

Nucleic acids provide a very promising molecular platform for the formulation of next-generation therapeutic nanocarriers. Specific sequence motifs for targeting, immunomodulation, structural stability, and drug loading can be incorporated into a modular nanocarrier via the well-known base pairing mechanism.[12] Controllable, layer-by-layer assembly allows for the formulation of multifunctional nanocarriers tuned to overcome the multitude of physiological barriers to drug delivery, including in vivo stability and degradation, tissue localization, immunogenicity, and overcoming multidrug resistance.[13–15] Thus, utilizing nucleic acids as the functional component of nanocarriers provides significant advantages over presently used strategies. However, one of the largest barriers to successful administration of nucleic acid nanocarriers is control over drug release, an essential parameter for highly toxic chemotherapeutics.[16,17] Unfortunately, controlling the release of drugs from nanocarriers is a great challenge.[18]

The mechanisms by which cytotoxic drugs interact with nucleic acids can be exploited to carry drug payloads, but no research thus far has utilized these mechanisms to control drug release. The mechanism of action of the drug can effectively be used in the design of the nanocarrier. Our group has pioneered this biomimetic approach to drug release using a novel, biohybrid nanocarrier based on thiolated nucleic acids conjugated to a 15 nm gold nanoparticle (AuNP) and demonstrated controlled release of drugs by varying binding affinity via sequence modulation.[19,20] Furthermore, we recently showed that the transport of a negatively charged drug bound to the surface of AuNPs can be

controlled by increasing the degree of folding/coiling of the oligonucleotide layer.[21] In this work, we show for the first time that a biomimetic approach to DNA monolayer design can be utilized to control the release of an intercalating drug, daunomycin. Daunomycin intercalates within double-stranded DNA non-covalently via molecular shape, hydrogen bonding, salt bridging, and van der Waals interactions.[22] It binds preferentially to GC-rich nucleotide sequences, specifically those flanked by an AT base pair.[23] The high-affinity binding sequence is represented by an oligonucleotide containing multiple AGC motifs (Table 6.1). At the onset of our studies, we hypothesized that by increasing the thickness of oligonucleotide monolayers we can extend the release of daunomycin. We investigated this hypothesis by pre-loading DNA duplexes with the drug and immobilizing them on gold-coated wafers to measure drug release. Additionally, we compared the release of drug from two distinct sequences conjugated to AuNPs to determine the effects of shape and curvature of the nanocarrier on drug release.

6.2 Materials and Methods

6.2.1 Materials

Custom DNA oligonucleotides with 5' terminal thiol modifications were purchased from IDT (Coralville, IA). They consisted of a high-affinity binding sequence comprised of a nucleotide triplicate motif (AGC) and a random sequence of the same length (RAN). Each sequence has a 6 nucleotide spacer and a drug binding region comprised of either 4, 8, or 12 intercalating sites (4X, 8X, and 12X). Gold-coated silicon wafers with 10mm^2 area and 100nm thick gold layers were purchased from Platypus Technologies (Madison, WI). Daunomycin powder was purchased from VWR (Radnor, PA). All other reagents were purchased from VWR.

6.2.2 Drug Loading and Quantification

DNA oligonucleotides at a constant concentration were mixed with molar ratios of daunomycin from 25-1000 to 1 (drug to DNA) in water overnight on a rocking platform at room temperature. The fluorescence of the sample was measured on a Spectramax M3 spectrophotometer (Malvern) with an excitation of 495nm and an emission of 595nm. DNA-containing samples were compared to equivalent concentrations of drug without DNA. Since daunomycin will not fluoresce while in complex with DNA, the calculated difference in total drug concentration represents the fraction of drug intercalated in DNA oligonucleotides.

6.2.3 Wafer Preparation and DNA Loading

Gold wafers were precleaned in base piranha solution for 5 min at 70^{o}C and dried under N_2. They were then submerged in a solution of drug loaded oligonucleotides at a concentration of 300nM for one hour at room temperature. The DNA loaded wafers were rinsed three times with PBS to remove unbound material. They were utilized immediately for drug release studies after loading.

6.2.4 Drug Release Studies

DNA loaded wafers with intercalated daunomycin were submerged in 3mL of PBS in a 24-well plate and kept at 37^{o}C during the course of the experiment. At specified time intervals a sample of release media was taken and measured for the presence of daunomycin, followed by replacement of fresh PBS in each well. The cumulative release of drug was plotted over time until no further release was detected. Release data was converted into a fractional release by calculating the ratio of mass released at each time point and the total mass released at the end of the experiment (M_t/M_∞).

6.2.5 Drug Release Modeling

The Korsmeyer-Peppas model describes drug release phenomena according to the following equation:

$$\frac{M_t}{M_\infty} = k_{KP} t^n$$

Where M_t/M_∞ is the fractional release at time t, k_{KP} is the release rate constant, and n is the release exponent that provides information about the mechanism of drug release. This model is appropriate used for values $M_t/M_\infty < 0.60$. A value of n=0.5 describes first-order release kinetics, values of $0.5 < n < 1$ describes anomalous (non-Fickian) diffusion, and n=1 describes zero-order release.

6.3 Results

We utilized low and high affinity daunomycin binding sequences of DNA across three different oligonucleotide lengths to control drug release from DNA films on gold surfaces. The high affinity sequence (AGC) is comprised of a repeating AGC motif which provides an energetically favored molecular structure for drug intercalation. The low affinity sequence (RAN) is a random oligonucleotide sequence designed to have a low GC content. The DNA sequences used in this work are shown in Table 6.1.

Both the RAN and AGC sequences were investigated at three lengths corresponding to the theoretical amount of drug per oligonucleotide, i.e. 4X, 8X, or 12X daunomycin molecules per DNA. These designations represent binding regions of 12, 24, and 36 base pairs in length, respectively, with one drug molecule intercalated at every three base pairs. The total drug bound to all oligonucleotides according to length is shown in Figure 6.1. The rate of drug binding increases with an increasing molar ratio of daunomycin until a plateau around the theoretical limit of intercalation at a molar ratio of

500:1 drug to DNA. As the DNA sequences get longer, the rate of drug loading increases more rapidly with increasing amounts of drug. This is due to the positive cooperativity of daunomycin intercalation along with the greater concentration of binding sites contained in the longer oligonucleotides. At the highest molar ratios intercalation decreases slightly for all sequences, which may be attributed to the instability of daunomycin in aqueous solutions at high concentrations.

All sequences were pre-loaded with daunomycin and immobilized on gold wafers via 5'-terminal thiol modifications to measure drug release over time. The release constants are summarized in Table 6.2. Within the length scales used, the investigated DNA duplexes form organized, upright monolayers with binding densities in the range of $3x10^{12}$ oligonucleotides/cm^2.[21] Therefore, the only variables are the nucleotide sequence and the thickness of the DNA layer.

The fractional release of daunomycin from RAN sequences over 168 h is shown in Figure 6.2. After 24 hours, RAN 4X released 68% of the total bound drug and the release began to plateau at 96 h. The parameter *n* calculated from equation 1 was 0.572, indicating an approximate first-order release. By increasing the length of the oligonucleotide, the release of drug from RAN sequences is extended. Both RAN 8X and RAN 12X released drug for up to 144 h, with the release constant for RAN 12X being half of that of 8X. The calculated *n* for RAN 8X was 0.524, lower than for RAN 4X, and again approximating first-order kinetics. For RAN 12X, *n* was 0.606, indicating non-Fickian diffusion.

The fractional release of daunomycin from AGC-rich sequences over 336 h is shown in Figure 6.3. After 24 hours, AGC 4X released 41% of the total bound drug and

by 96 h had released only 75% of drug. By the end of one week AGC 4X had released 95% of the bound drug. The parameter n for AGC 4X was 0.636, indicating non-Fickian diffusion and more control over drug transport. Increasing length of AGC extended the release for 216 and 288 h for AGC 8X and AGC 12X, respectively. Compared to AGC 4X, the release constants are reduced by a factor of 6.1 and 15.3, respectively. AGC 8X sequence has an *n* value of 0.864, while AGC 12X has an *n* value of 0.976, or nearly zero order.

To further analyze the effects of sequence and length on drug release, the release rate constants k_{KP} for both sequences were plotted as a function of oligonucleotide length, corresponding to 4X, 8X, or 12X drug per oligonucleotide. The results are shown in Figure 6.4. Release rates for RAN sequences are 2.2, 9.6, and 12.3-fold higher than corresponding AGC sequences for 4X, 8X, and 12X lengths, respectively. RAN release constants decrease linearly ($R^2 = 0.998$) as the sequence is extended (slope = -0.011). For sequence AGC, the release rate decreases more rapidly between 4X and 8X (linear slope = -0.013). The value k_{KP} for all three lengths of AGC follows a power law relationship ($R^2 = 1$). Thus, increasing the length of AGC above 12X, or 36 bp, is likely to show diminishing returns regarding drug release.

As drugs are delivered using spherical nanoparticles, curvature of the surface to which DNA is attached is likely to play a role in release rate. This is due to the increased surface area to volume ratio at the nanoscale and the resultant substantial increase in deflection angle between neighboring oligonucleotides.[24] To investigate this, we compared RAN 12X and AGC 12X drug-loaded sequences on 15 nm AuNPs and measured drug release over 144 h. The results are shown in Figure 6.5. Release rate

constants are shown in Table 6.2. The release kinetics are strikingly different on AuNPs compared to planar gold. In this case, the best fit for release kinetics for both sequences is first-order kinetics (n = 0.43 for spherical particles). AuNP-RAN release all of the drug payload in 48 h, while AuNP-AGC extends the release for 96 h. Additionally, the release rate constant of AuNP-AGC is significantly lower than AuNP-RAN (0.304 and 0.401, respectively).

6.4 Discussion

Nucleic acids have excellent potential for constructing personalizable drug delivery vehicles but controlling the release of intercalated drugs presents a huge challenge for researchers. In this work, we were able to achieve improved drug release kinetics from gold wafers and AuNPs coated with diverse DNA sequences of various length . On the flat surface of the wafers, we also achieved near constant release of the drug from a DNA monolayer via sequence and length modulation. However, the release from the AuNP surface was much more rapid.

The mechanism of daunomycin binding to nucleic acid duplexes has been described in previous reports.[22,23] Insights into the structure of the daunomycin-DNA complex reveals the likely reason for the sequence specific drug release. The aglycon chromophore of daunomycin is oriented at a right angle to the long axis of the DNA with the cyclohexane ring and daunosamine moieties resting in the minor groove, covering three base pairs. The ratio of one drug per three base pairs is confirmed in Figure 6.1. Several hydrogen bonds and a bridging sodium ion stabilize the complex. The hydroxyl group on daunomycin C9 forms two hydrogen bonds with N2 and N3 of the adjacent guanine. These two hydrogen bonds contribute to the preference of daunomycin for

subsequent GC base pairs. Additionally, a flanking AT may be energetically favorable as well due to the repulsive forces that would arise between the daunosamine and the 2-amino group of guanine if a GC pair were substituted.[23] Thus, the specific motif of AGC within oligonucleotide duplexes is energetically favored than the RAN sequence and results in more extended drug release.

Figures 6.2 and 6.3 illustrate that increasing sequence length leads to more extended drug release, even for RAN sequences. One driver for this extended release is the principle of excluded volume. As the drug must diffuse through the polymer before dissolving in solution, longer DNA oligonucleotides increase the steric restrictions on the diffusing molecules, keeping them trapped within the polymer layer. Indeed, in low ionic conditions, the effective diameter of upright oligonucleotides increases substantially compared to the crystal diameter of DNA.[25,26] Additionally, the binding of daunomycin to DNA duplexes exhibits positive cooperativity at physiological salt concentrations.[20,27] Thus, the drug likely intercalates with higher affinity to the longer sequences. This higher affinity would supplement the excluded volume effect and sustain the release of the drug for longer periods. In the case of AGC 12X, where sequence specificity, excluded volume, and cooperative binding all play a part, diffusion of the drug is effectively controlled.

Additionally, unique intermolecular interactions between the parallel DNA sequences cannot be discounted.[28] Recently it was observed that homologous DNA sequences can undergo complex intermolecular associations even in physiological salt concentrations.[29] This phenomena may be exacerbated by the dense packing of parallel DNA on the gold surface. Furthermore, guanine-rich sequences are capable of forming

inter- and intra-molecular structures such as the G-quadruplex. It has been observed that daunomycin can interact with G-quadruplex structures and effectively increase the thermal stability of the complex.[30] Thus, for the AGC sequences, the presence of parallel strand interactions stimulated by the high GC content and the subsequent binding of daunomycin and complex stabilization may further contribute to the controlled release of the drug from the DNA layer. The extent to which these intermolecular interactions play a role, if at all, is unknown.

Finally, the striking differences in release kinetics between oligonucleotide layers in planar gold and AuNPs must be noted. Daunomycin was released at a rate between 3 and 4-fold faster using sequences attached to AuNPs compared to planar surfaces. Additionally, AuNPs show concentration based, first-order release kinetics as opposed to the controlled transport exhibited by the planar monolayers. Indeed, even for small oligonucleotides, the surface curvature of AuNPs has significant effects on the deflection angle between adjacent molecules.[24] This curvature has significant implications for properties such as surface ligand structure, surface solvation, and flow dynamics.[31–33] Our experiments clearly demonstrate that the curvature increases the rate of drug release. It is likely that the increased curvature on the nanoparticle surface significantly reduces the intermolecular interactions between parallel-oriented DNA strands and the probability of re-binding of the drug to DNA strands with free intercalation sites. Thus, transport from the layer cannot be controlled precisely and dissociated drug is quick to dissolve in the release media.

Spherical nucleic acid nanocarriers, such as those constructed on AuNPs in this work, have gained great interest for their stability in vivo and ability to be internalized

into cells.[34] To date, they have been used mainly as agents for delivering RNAs rather than as nanocarriers for chemotherapeutics drugs. More recently, a first-in-human phase 0 clinical study of RNA interference–based spherical nucleic acids has commenced to treat patients with recurrent glioblastoma.[35] The principles of design for nucleic acid nanocarriers may require a different strategy. Fortunately, nucleic acids provide a toolkit for the facile production of unique nanoarchitectures based on specific angles to create distinct molecular shapes and tunable physiochemical properties.[36–38] As such, the investigation of nanostructures with flat surfaces, such as polyhedra, or at least larger aspect ratios, such as nanorods, may provide both the advantages of spherical nucleic acid architecture with the advantages of planar nucleic acid layers for extending drug release.

6.5 Conclusions

In conclusion, this work shows for the first time near zero-order release of an intercalating drug from an engineered DNA monolayer via biomimetically exploiting the binding mechanism of the drug to nucleic acids. This was achieved by modulating the nucleotide sequence and length of a drug loaded DNA oligonucleotide to take advantage of the sequence-specific and cooperative binding of the drug. By using a 36 bp sequence comprised of a repeating AGC motif immobilized on a planar gold surface, the release was sustained for 12 days. However, the high curvature of AuNPs resulted in a much more rapid release, emphasizing the importance of particle shape and curvature on the structure of the DNA layer and subsequently the release of the drug. These results will significantly impact the future design of therapeutic nanoparticles driven by the excellent tailorability of nucleic acid nanomaterials. Future work will investigate the synergism of

oligonucleotide sequence, structure, and particle shape and their influence on drug release profiles.

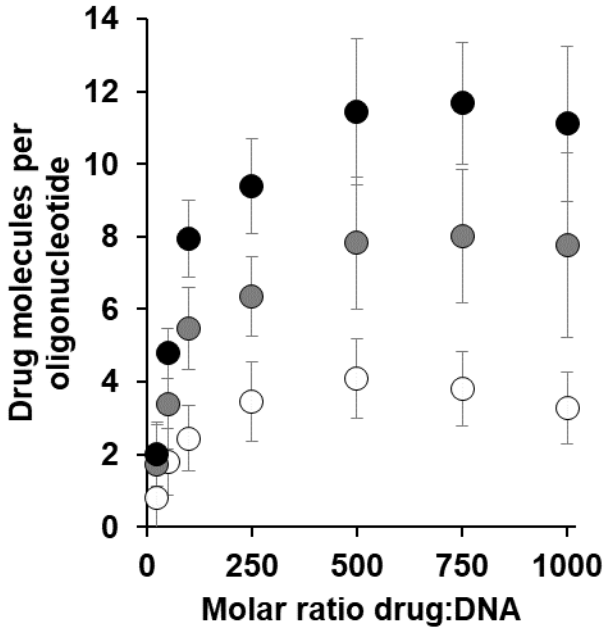

Figure 6.1. Daunomycin loading as a function of molar ratio of drug to DNA. DNA sequences were designed to have either 12, 24, or 36 bp binding regions corresponding to 4X (○), 8X (●), or 12X (●) binding sites. Both RAN and AGC sequences loaded comparable amounts of daunomycin. Results are shown as average of both sequences. Loading values approached theoretical maxima for all sequences at a molar ratio of 500:1 drug:DNA.

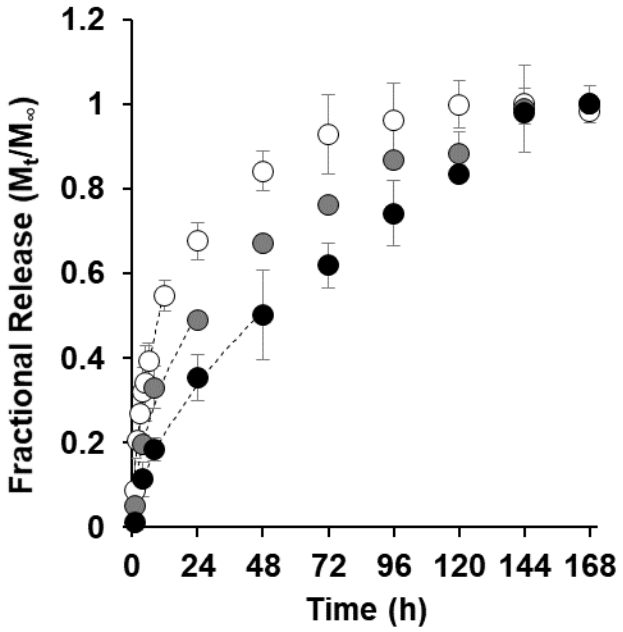

Figure 6.2. Comparing drug release between RAN sequences with 4X, 8X, and 12X intercalation sites. RAN sequences pre-loaded with drug were self-assembled on a planar gold surface and submerged in PBS at 37ºC. Sequence lengths of 4X (○), 8X (●), or 12X (●) were investigated. Drug release from RAN is extended as the sequence length increases, emphasizing monomer size-dependent release kinetics. Dotted lines represent a fit of the first 60% of drug release to the Korsmeyer-Peppas equation.

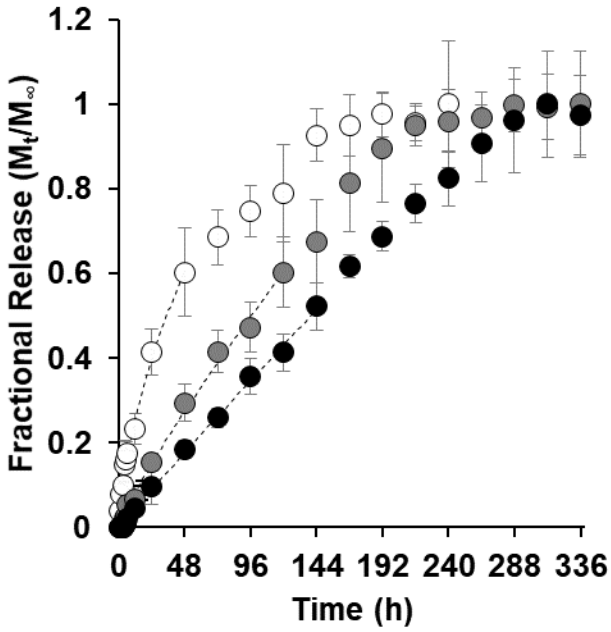

Figure 6.3. Comparing drug release between AGC sequences with 4X, 8X, and 12X intercalation sites. AGC sequences pre-loaded with drug were self-assembled on a planar gold surface and submerged in PBS at 37ºC. Sequence lengths of 4X (○), 8X (●), or 12X (●) were investigated. Drug release from AGC is extended as the sequence length increases, emphasizing monomer size-dependent release kinetics. Additionally, release is extended at a greater rate compared to RAN, reinforcing the sequence-dependent release. AGC 12X shows near zero-order release kinetics, indicating exquisite control of drug transport. Dotted lines represent a fit of the first 60% of drug release to the Korsmeyer-Peppas equation.

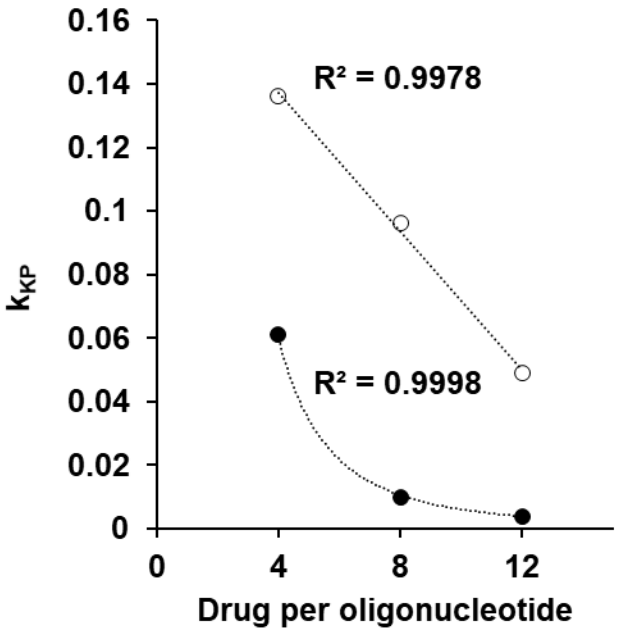

Figure 6.4. Comparing release rate constants (k_{KP}) of RAN and AGC sequences at increasing sequence lengths. Sequence designators of 4X, 8X, and 12X represent the theoretical and observed loading of daunomycin per oligonucleotide. For RAN (○), k_{KP} has a negative linear correlation to sequence length. For AGC (●), all values of k_{KP} are lower than that of RAN with equivalent length. Additionally, across the same length scales, k_{KP} for AGC decreases according to a power law relationship.

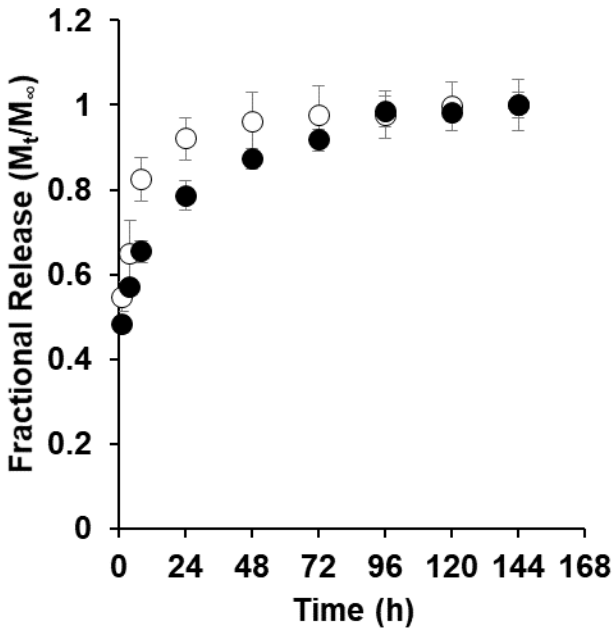

Figure 6.5. Comparing drug release between 15 nm AuNPs conjugated with RAN and AGC sequences with 12X intercalation sites. Release from AuNPs is unique due to the high surface curvature of the particles compared to planar gold. Both sequences release drug at a much more rapid rate in comparison. Here, the sequence specificity is still showcased as AuNP-AGC (●) release at a slower rate compared to AuNP-RAN (○). Both release profiles fit well with first-order release kinetics, corresponding to $n = 0.43$ as determined via fitting to the Korsmeyer-Peppas equation.

Table 6.1

DNA Sequences

Name	Sequence
RAN (4X)	5′–S–TTTTATGGTTTACAATATT CCAAATGTTATAA
RAN (8X)	5′–S–TTTTATGGTTTACAATATTGTTTACAATATT CCAAATGTTATAACAAATGTTATAA
RAN (12X)	5′–S–TTTTATGGTTTACAATATTGTTTACAATATTGTTTACAATATT CCAAATGTTATAACAAATGTTATAACAAATGTTATAA
AGC (4X)	5′–S–TTTTATACGACGACGACGA TGCTGCTGCTGCT
AGC (8X)	5′–S–TTTTATAGCAGCAGCAGCAGCAGCAGCA TCGTCGTCGTCGTCGTCGTCGTCGT
AGC (12X)	5′–S–TTTTATAGCAGCAGCAGCAGCAGCAGCAGCAGCAGCAGCA TCGTCGTCGTCGTCGTCGTCGTCGTCGTCGTCGTCGT

Table 6.2

Release Rate Constants

		k_{KP}	n	R^2
RAN	**4X**	0.136	0.572	0.972
	8X	0.096	0.524	0.959
	12X	0.049	0.606	0.987
AGC	**4X**	0.061	0.636	0.982
	8X	0.010	0.864	0.993
	12X	0.004	0.976	0.998
AuNP	**RAN 12X**	0.401	0.43	0.950
	AGC 12X	0.304	0.43	0.939

Chapter 7

Conclusions

7.1 Significance

In the battle against cancer, much progress has been made in the past century. However, the fight is far from over. During the COVID-19 pandemic, the suggestion from professional societies such as the American Cancer Society, the American Society of Clinical Oncology, the American Society of Breast Surgeons, the American College of Radiology, and the American Society for Colposcopy and Cervical Pathology was to postpone routine healthcare checkups in order to avoid possible exposure to the virus; this included routine cancer screenings.[319] As a result, many screenings for common cancers such as breast, cervical, and colorectal were skipped over the past two years. Therefore, the incidence of cancer in the future is expected to trend upward.

Nanomedicine has seen an unprecedented expansion in recent years for the diagnosis and treatment of cancer. The profound tunability of nanomaterials and the capability to bind, adsorb, or carry drugs make them extremely attractive in the field of oncology and has had significant impact on the field.[320] Of the multitude of materials at our disposal, nucleic acids present the most compelling choice for bottom-up assembly of anticancer nanomedicines. Unfortunately, to date there has been a significant lack of methods to control the release of drugs from nucleic acid nanocarriers for sustained drug release. With this dissertation, novel biomimetic strategies for controlling drug release are exhibited via facile manipulation of immobilized DNA nanoarchitectures using both surface-bound and intercalating drugs. Using a high-affinity binding sequence for daunomycin and increasing the thickness of the DNA layer, near zero-order release

kinetics were observed, an unprecedented feat in the field. Thus, the strategies herein will profoundly impact the field regarding the design of next-generation therapeutic nanocarriers.

7.2 Broader Impacts

Spherical nucleic acids are not restricted to gold surfaces. Indeed, similar structures have been formed on silica, iron oxide, proteins, liposomes, micelles, PLGA, and as hollow spheres, and the oligonucleotide layer can be formed using DNA, RNA, peptide NAs, etc. Thus, the possibilities of customization and personalization are extensive. Additionally, NA nanoparticles can formulated for more advanced delivery systems such as inhalable therapeutics,[321] blood-brain-barrier penetration,[322] and injectable hydrogels,[323] exemplifying their applicability in a number of unique situations. Furthermore, in this work, two specific template drugs were utilized. Dexamethasone was bound to the gold surface via electrostatic attraction from the fluorine atom; thus, other fluorinated corticosteroids, or other small molecule drugs capable of sticking to gold, can likely be utilized in the same manner for controlled drug release. Similarly, daunomycin is not the only intercalating therapeutic, and indeed many therapeutics interact with the major and minor grooves of nucleic acids in different ways - such drugs can be investigated for sequence specificity and exploited in similar ways to control drug release. Therefore, the methods of drug release described in this work can be exploited in a vast number of distinct ways in order to produce highly tailorable and personalizable nanocarriers for drug delivery in the treatment of many pressing diseases.

7.3 Concluding Remarks

The main conclusions of this work are as follows: 1) the nanoarchitectures of nucleic acid monolayers on gold surfaces can be manipulated via sequence and length selection, cation addition, immobilization strategy, and core surface curvature, 2) the release of a surface-bound drug can be controlled by inducing distinct nanoarchitecture, e.g., folded or upright nucleic acid orientations, and 3) the release of an intercalating drug can be controlled via sequence selection, changes in layer thickness, and core surface curvature. These strategies will have a great impact on future design of next-generation therapeutic nanocarriers and will improve personalized therapies for chemotherapeutic delivery.

The influence of surface curvature presents one of the most interesting possibilities. Future work should involve drug release from polyhedral, discoidal, or rod-shaped gold nanoparticles to determine how curvature and surface area affect the release rate. In Chapter 2, the influence of nanoparticle shape was discussed in terms of transport through physiological barriers. Thus, a more focused investigation of how these properties influence drug release is needed.

Additionally, a clinically focused nanocarrier will gain significant advantages using a targeting ligand. Nucleic acid aptamers constitute the likely next-generation of targeting molecules, although they have not been optimized for clinical use as of yet. Oligonucleotide-conjugated antibodies are another advanced method of targeting, provided that their addition does not significantly later the size or shape of the underlying nanocarrier. These molecules can be conjugated to the surface of NA nanocarriers either via complementary hybridization or through the use of a long PEG spacer, which is

charge neutral and thus able to penetrate dense NA layers on gold surfaces. Thus, through utilization of the techniques discovered herein to control drug release, novel nanocarriers can be synthesized with different shapes and sizes (determined by core structure) and different targeting capabilities (determined by the outer layer structure), with controllable drug release NA layers remaining on the core surface.

References

1. Ferlay J, Ervik M, Lam F, et al. Global Cancer Observatory: Cancer Today. Lyon, France: International Agency for Research on Cancer. Published 2020. https://gco.iarc.fr/today/home

2. Cancer: Key facts. World Health Organization. Published 2022. https://www.who.int/news-room/fact-sheets/detail/cancer

3. Siegel RL, Miller KD, Fuchs HE, Jemal A. Cancer statistics, 2022. *CA Cancer J Clin*. 2022;72(1):7-33. doi:10.3322/caac.21708

4. Mariotto AB, Enewold L, Zhao J, Zeruto CA, Robin Yabroff K. Medical care costs associated with cancer survivorship in the United States. *Cancer Epidemiol Biomarkers Prev*. 2020;29(7):1304-1312. doi:10.1158/1055-9965.EPI-19-1534

5. Strebhardt K, Ullrich A. Paul Ehrlich's magic bullet concept: 100 Years of progress. *Nat Rev Cancer*. 2008;8(6):473-480. doi:10.1038/nrc2394

6. DeVitaJr. VT, Chu E. A history of cancer chemotherapy. *Cancer Res*. 2008;68(21):8643-8653.

7. Shear M, Hartwell J, Peters V, Dalton A. Some aspects of a joint institutional research program on chemotherapy of cancer: current laboratory and clinical experiments with bacterial. *Approaches to tumor Chemother Washingt Am Assoc Adv Sci*. Published online 1947:236-284.

8. Cheung-Ong K, Giaever G, Nislow C. DNA-damaging agents in cancer chemotherapy: Serendipity and chemical biology. *Chem Biol*. 2013;20(5):648-659. doi:10.1016/j.chembiol.2013.04.007

9. Devita VT, Serpick AA, Carbone PP. Combination chemotherapy in the treatment of advanced Hodgkin's disease. *Ann Intern Med*. 1970;73(6):881-895. doi:10.7326/0003-4819-73-6-881

10. Liu JKH. The history of monoclonal antibody development - Progress, remaining challenges and future innovations. *Ann Med Surg*. 2014;3(4):113-116. doi:10.1016/j.amsu.2014.09.001

11. Druker BJ, Tamura S, Buchdunger E, et al. Effects of a selective inhibitor of the Ab1 tyrosine kinase on the growth of Bcr-Ab1 positive cells. *Nat Med*. 1996;2(5):561-566. doi:10.1038/nm0596-561

12. Topalian SL, Drake CG, Pardoll DM. Immune checkpoint blockade: A common denominator approach to cancer therapy. *Cancer Cell*. 2015;27(4):450-461. doi:10.1016/j.ccell.2015.03.001

13. Miliotou AN, Papadopolou LC. CAR T-cell Therapy: A New Era in Cancer Immunotherapy. *Curr Pharm Biotechnol*. 2018;19(1):5-18. doi:10.1155/2016/5474602

14. Barenholz Y. Doxil® - The first FDA-approved nano-drug: Lessons learned. *J Control Release*. 2012;160(2):117-134. doi:10.1016/j.jconrel.2012.03.020

15. Haney SA. Expanding the repertoire of RNA interference screens for developing new anticancer drug targets. *Expert Opin Ther Targets*. 2007;11(11):1429-1441. doi:10.1517/14728222.11.11.1429

16. Wang M, Zhao J, Zhang L, et al. Role of tumor microenvironment in tumorigenesis. *J Cancer*. 2017;8(5):761-773. doi:10.7150/jca.17648

17. Yuan Y, Gu Z, Yao C, Luo D, Yang D. Nucleic Acid–Based Functional Nanomaterials as Advanced Cancer Therapeutics. *Small*. 2019;15(26):1900172. doi:10.1002/smll.201900172

18. Verma M. Personalized medicine and cancer. *J Pers Med*. 2012;2(1):1-14.

19. Nikulainen T, Palmberg C. Transferring science-based technologies to industry-Does nanotechnology make a difference? *Technovation*. 2010;30(1):3-11. doi:10.1016/j.technovation.2009.07.008

20. Kargozar S, Mozafari M. Nanotechnology and Nanomedicine: Start small, think big. *Mater Today Proc*. 2018;5(7):15492-15500. doi:10.1016/j.matpr.2018.04.155

21. Duncan R, Gaspar R. Nanomedicine(s) under the Microscope. *Mol Pharm*. 2011;8(6):2101-2141. doi:10.1201/9780429027819-13

22. Wagner V, Dullaart A, Bock A-K, Zweck A. The emerging nanomedicine landscape. *Nat Biotechnol*. 2006;24:1211-1217.

23. He H, Liu L, Morin EE, Liu M, Schwendeman A. Survey of Clinical Translation of Cancer Nanomedicines - Lessons Learned from Successes and Failures. *Acc Chem Res*. 2019;52(9):2445-2461. doi:10.1021/acs.accounts.9b00228

24. Germain M, Caputo F, Metcalfe S, et al. Delivering the power of nanomedicine to patients today. *J Control Release*. 2020;326:164-171. doi:10.1016/j.jconrel.2020.07.007

25. Wang Y, Sun S, Zhang Z, Shi D. Nanomaterials for Cancer Precision Medicine. *Adv Mater*. 2018;30(17):1705660. doi:10.1002/adma.201705660

26. Barkalina N, Charalambous C, Jones C, Coward K. Nanotechnology in reproductive medicine: Emerging applications of nanomaterials. *Nanomedicine Nanotechnology, Biol Med*. 2014;10(5):e921-e938. doi:10.1016/j.nano.2014.01.001

27. Bilal M, Barani M, Sabir F, Rahdar A, Kyzas GZ. Nanomaterials for the treatment and diagnosis of Alzheimer's disease: An overview. *NanoImpact*. 2020;20:100251. doi:10.1016/j.impact.2020.100251

28. Rixin C, Dan Q, Peng W, Lingjun L, Yangheng Z, Fuhua Y. Gold Nanoclusters Exert Bactericidal Activity and Enhance Phagocytosis of Macrophage Mediated Killing of Fusobacterium nucleatum. *Front Nanomater*. 2021;8.

29. Jiang W, Rutherford D, Vuong T, Liu H. Nanomaterials for treating cardiovascular diseases: A review. *Bioact Mater*. 2017;2(4):185-198. doi:10.1016/j.bioactmat.2017.11.002

30. Lim JW, Ahn YR, Park G, Kim HO, Haam S. Application of nanomaterials as an advanced strategy for the diagnosis, prevention, and treatment of viral diseases. *Pharmaceutics*. 2021;13(10):1570. doi:10.3390/pharmaceutics13101570

31. Oshi MA, Haider A, Siddique MI, et al. Nanomaterials for chronic inflammatory diseases: the current status and future prospects. *Appl Nanosci*. Published online 2021. doi:10.1007/s13204-021-02019-8

32. Masoudi Asil S, Ahlawat J, Guillama Barroso G, Narayan M. Nanomaterial based drug delivery systems for the treatment of neurodegenerative diseases. *Biomater Sci*. 2020;8(15):4109-4128. doi:10.1039/d0bm00809e

33. Sanvicens N, Marco MP. Multifunctional nanoparticles - properties and prospects for their use in human medicine. *Trends Biotechnol*. 2008;26(8):425-433. doi:10.1016/j.tibtech.2008.04.005

34. Anselmo AC, Mitragotri S. Nanoparticles in the clinic: An update post COVID-19 vaccines. *Bioeng Transl Med*. 2021;6:e10246. doi:10.1002/btm2.10246

35. Ariga K, Leong DT, Mori T. Nanoarchitectonics for Hybrid and Related Materials for Bio-Oriented Applications. *Adv Funct Mater*. 2018;28(27). doi:10.1002/adfm.201702905

36. Ruiz-Hitzky E, Darder M, Aranda P, Ariga K. Advances in biomimetic and nanostructured biohybrid materials. *Adv Mater*. 2010;22(3):323-336. doi:10.1002/adma.200901134

37. Khai B, Ngo D, Grunlan MA. Protein Resistant Polymeric Biomaterials. Published online 2017. doi:10.1021/acsmacrolett.7b00448

38. Elschner T, Obst F, Heinze T. Furfuryl- and Maleimido Polysaccharides: Synthetic Strategies Toward Functional Biomaterials. *Macromol Biosci*. 2018;18(11):1800258. doi:10.1002/mabi.201800258

39. Clegg JR, Peppas NA. Molecular recognition with soft biomaterials. *856 | Soft Matter*. 2020;16:856. doi:10.1039/c9sm01981b

40. Pattanashetti NA, Heggannavar GB, Kariduraganavar MY. Smart Biopolymers and their Biomedical Applications. *Procedia Manuf*. 2017;12:263-279. doi:10.1016/j.promfg.2017.08.030

41. Sharma P, Dwivedi S. Prospects of Molecular Biotechnology in Diagnostics: Step Towards Precision Medicine. *Indian J Clin Biochem*. 2017;32(2):121-123. doi:10.1007/s12291-017-0650-9

42. Metselaar JM, Lammers T. Challenges in nanomedicine clinical translation. *Drug Deliv Transl Res*. 2020;10(3):721-725. doi:10.1007/s13346-020-00740-5

43. Wu LP, Wang D, Li Z. Grand challenges in nanomedicine. *Mater Sci Eng C*. 2020;106:110302. doi:10.1016/j.msec.2019.110302

44. Fernandez-Moure JS. Lost in translation: The gap in scientific advancements and clinical application. *Front Bioeng Biotechnol*. 2016;4(43). doi:10.3389/fbioe.2016.00043

45. Blanco E, Shen H, Ferrari M. Principles of Nanoparticle Design for Overcoming Biological Barriers to Drug Delivery. *Nat Biotechnol*. 2015;33:941-951. doi:10.1201/9780429027819-9

46. Arisaka Y, Yui N. Polyrotaxane-based biointerfaces with dynamic biomaterial functions. *J Mater Chem B*. 2019;7(13):2123-2129. doi:10.1039/c9tb00256a

47. Jaspers M, Vaessen SL, Van Schayik P, Voerman D, Rowan AE, Kouwer PHJ. Nonlinear mechanics of hybrid polymer networks that mimic the complex mechanical environment of cells. *Nat Commun*. 2017;8(1):1-10. doi:10.1038/ncomms15478

48. Johnston MC, Scott CJ. Antibody conjugated nanoparticles as a novel form of antibody drug conjugate chemotherapy. *Drug Discov Today Technol*. 2018;30:63-69. doi:10.1016/j.ddtec.2018.10.003

49. Mitragotri S, Lahann J. Physical approaches to biomaterial design. *Nat Mater*. 2009;8(1):15-23. doi:10.1038/nmat2344

50. Anselmo AC, Mitragotri S. Impact of particle elasticity on particle-based drug delivery systems. *Adv Drug Deliv Rev*. 2017;108:51-67. doi:10.1016/j.addr.2016.01.007

51. Ernsting MJ, Murakami M, Roy A, Li SD. Factors controlling the pharmacokinetics, biodistribution and intratumoral penetration of nanoparticles. *J Control Release*. 2013;172(3):782-794. doi:10.1016/j.jconrel.2013.09.013

52. Mout R, Moyano DF, Rana S, Rotello VM. Surface functionalization of nanoparticles for nanomedicine. *Chem Soc Rev*. 2012;41(7):2539-2544. doi:10.1039/c2cs15294k

53. Gisbert-Garzarán M, Vallet-Regí M. Influence of the surface functionalization on the fate and performance of mesoporous silica nanoparticles. *Nanomaterials*. 2020;10:916. doi:10.3390/nano10050916

54. Kohane DS, Plesnila N, Thomas SS, Le D, Langer R, Moskowitz MA. Lipid-sugar particles for intracranial drug delivery: Safety and biocompatibility. *Brain Res*. 2002;946(2):206-213. doi:10.1016/S0006-8993(02)02878-0

55. Kohane DS, Tse JY, Yeo Y, Padera R, Shubina M, Langer R. Biodegradable polymeric microspheres and nanospheres for drug delivery in the peritoneum. *J Biomed Mater Res - Part A*. 2006;77(2):351-361. doi:10.1002/jbm.a.30654

56. Choi HS, Liu W, Misra P, et al. Renal clearance of nanoparticles. *Nat Biotechnol*. 2007;25(10):1165-1170. doi:10.1038/nbt1340.

57. Decuzzi P, Godin B, Tanaka T, et al. Size and shape effects in the biodistribution of intravascularly injected particles. *J Control Release*. 2010;141(3):320-327. doi:10.1016/j.jconrel.2009.10.014

58. He C, Hu Y, Yin L, Tang C, Yin C. Effects of particle size and surface charge on cellular uptake and biodistribution of polymeric nanoparticles. *Biomaterials*. 2010;31(13):3657-3666. doi:10.1016/j.biomaterials.2010.01.065

59. Kamps JAAM, Morselt HWM, Swart PJ, Meijer DKF, Scherphof GL. Massive targeting of liposomes, surface-modified with anionized albumins, to hepatic endothelial cells. *Proc Natl Acad Sci U S A*. 1997;94(21):11681-11685. doi:10.1073/pnas.94.21.11681

60. Zhang YN, Poon W, Tavares AJ, McGilvray ID, Chan WCW. Nanoparticle–liver interactions: Cellular uptake and hepatobiliary elimination. *J Control Release*. 2016;240:332-348. doi:10.1016/j.jconrel.2016.01.020

61. Cataldi M, Vigliotti C, Mosca T, Cammarota MR, Capone D. Emerging role of the spleen in the pharmacokinetics of monoclonal antibodies, nanoparticles and exosomes. *Int J Mol Sci*. 2017;18(6):1249. doi:10.3390/ijms18061249

62. Decuzzi P, Lee S, Bhushan B, Ferrari M. A theoretical model for the margination of particles within blood vessels. *Ann Biomed Eng*. 2005;33(2):179-190. doi:10.1007/s10439-005-8976-5

63. Tan J, Shah S, Thomas A, Ou-Yang HD, Liu Y. The influence of size, shape and vessel geometry on nanoparticle distribution. *Microfluid Nanofluidics*. 2013;14:77-87. doi:10.1007/s10404-012-1024-5

64. Ikeda-Imafuku M, Wang LL-W, Rodrigues D, Shaha S, Zhao Z, Mitragotri S. Strategies to improve the EPR effect: A mechanistic perspective and clinical translation. *J Control Release*. Published online 2022. https://doi.org/10.1016/j.jconrel.2022.03.043

65. Kang H, Rho S, Stiles WR, et al. Size-Dependent EPR Effect of Polymeric Nanoparticles on Tumor Targeting. *Adv Healthc Mater*. 2020;9(1):308-311. doi:10.1002/adhm.201901223

66. Kolhar P, Anselmo AC, Gupta V, et al. Using shape effects to target antibody-coated nanoparticles to lung and brain endothelium. *Proc Natl Acad Sci U S A*. 2013;110(26):10753-10758. doi:10.1073/pnas.1308345110

67. Barua S, Yoo JW, Kolhar P, Wakankar A, Gokarn YR, Mitragotri S. Particle shape enhances specificity of antibody-displaying nanoparticles. *Proc Natl Acad Sci U S A*. 2013;110(9):3270-3275. doi:10.1073/pnas.1216893110

68. Lin SY, Hsu WH, Lo JM, Tsai HC, Hsiue GH. Novel geometry type of nanocarriers mitigated the phagocytosis for drug delivery. *J Control Release*. 2011;154(1):84-92. doi:10.1016/j.jconrel.2011.04.023

69. Walkey CD, Olsen JB, Guo H, Emili A, Chan WCW. Nanoparticle size and surface chemistry determine serum protein adsorption and macrophage uptake. *J Am Chem Soc*. 2012;134(4):2139-2147. doi:10.1021/ja2084338

70. Champion JA, Mitragotri S. Role of target geometry in phagocytosis. *Proc Natl Acad Sci U S A*. 2006;103(13):4930-4934. doi:10.1073/pnas.0600997103

71. Paul D, Achouri S, Yoon YZ, Herre J, Bryant CE, Cicuta P. Phagocytosis dynamics depends on target shape. *Biophys J*. 2013;105(5):1143-1150. doi:10.1016/j.bpj.2013.07.036

72. Shukla SK, Sarode A, Kanabar DD, et al. Bioinspired particle engineering for non-invasive inhaled drug delivery to the lungs. *Mater Sci Eng C*. 2021;128:112324. doi:10.1016/j.msec.2021.112324

73. Huang X, Li L, Liu T, et al. The shape effect of mesoporous silica nanoparticles on biodistribution, clearance, and biocompatibility in vivo. *ACS Nano*. 2011;5(7):5390-5399. doi:10.1021/nn200365a

74. Shah S, Liu Y, Hu W, Gao J. Modeling particle shape-dependent dynamics in nanomedicine. *J Nanosci Nanotechnol*. 2011;11(2):919-928. doi:10.1166/jnn.2011.3536

75. Hinde E, Thammasiraphop K, Duong HTT, et al. Pair correlation microscopy reveals the role of nanoparticle shape in intracellular transport and site of drug release. *Nat Nanotechnol*. 2017;12(1):81-89. doi:10.1038/nnano.2016.160

76. Banerjee A, Qi J, Gogoi R, Wong J, Mitragotri S. Role of nanoparticle size, shape and surface chemistry in oral drug delivery. *J Control Release*. 2016;238:176-185. doi:10.1016/j.jconrel.2016.07.051

77. Nowak M, Brown TD, Graham A, Helgeson ME, Mitragotri S. Size, shape, and flexibility influence nanoparticle transport across brain endothelium under flow. *Bioeng Transl Med*. 2020;5:e10153. doi:10.1002/btm2.10153

78. Arnida, Janát-Amsbury MM, Ray A, Peterson CM, Ghandehari H. Geometry and surface characteristics of gold nanoparticles influence their biodistribution and uptake by macrophages. *Eur J Pharm Biopharm*. 2011;77(3):417-423. doi:10.1016/j.ejpb.2010.11.010

79. Huang X, Teng X, Chen D, Tang F, He J. The effect of the shape of mesoporous silica nanoparticles on cellular uptake and cell function. *Biomaterials*. 2010;31(3):438-448. doi:10.1016/j.biomaterials.2009.09.060

80. Zhang B, Sai Lung P, Zhao S, Chu Z, Chrzanowski W, Li Q. Shape dependent cytotoxicity of PLGA-PEG nanoparticles on human cells. *Sci Rep*. 2017;7:7315. doi:10.1038/s41598-017-07588-9

81. Geng Y, Dalhaimer P, Cai S, et al. Shape effects of filaments versus spherical particles in flow and drug delivery. *Nat Nanotechnol*. 2007;2(4):249-255. doi:10.1038/nnano.2007.70

82. Champion JA, Mitragotri S. Shape induced inhibition of phagocytosis of polymer particles. *Pharm Res*. 2009;26(1):244-249. doi:10.1007/s11095-008-9626-z

83. Hui Y, Yi X, Hou F, et al. Role of Nanoparticle Mechanical Properties in Cancer Drug Delivery. *ACS Nano*. 2019;13(7):7410-7424. doi:10.1021/acsnano.9b03924

84. Merkel TJ, Jones SW, Herlihy KP, et al. Using mechanobiological mimicry of red blood cells to extend circulation times of hydrogel microparticles. *Proc Natl Acad Sci U S A*. 2011;108(2):586-591. doi:10.1073/pnas.1010013108

85. Anselmo AC, Zhang M, Kumar S, et al. Elasticity of nanoparticles influences their blood circulation, phagocytosis, endocytosis, and targeting. *ACS Nano*. 2015;9(3):3169-3177. doi:10.1021/acsnano.5b00147

86. Zhang L, Cao Z, Li Y, Ella-Menye JR, Bai T, Jiang S. Softer zwitterionic nanogels for longer circulation and lower splenic accumulation. *ACS Nano*. 2012;6(8):6681-6686. doi:10.1021/nn301159a

87. Sun X, Rossin R, Turner JL, et al. An assessment of the effects of shell cross-linked nanoparticle size, core composition, and surface PEGylation on in vivo biodistribution. *Biomacromolecules*. 2005;6(5):2541-2554. doi:10.1021/bm050260e

88. Allen TM, Austin GA, Chonn A, Lin L, Lee KC. Uptake of liposomes by cultured mouse bone marrow macrophages: influence of liposome composition and size. *BBA - Biomembr*. 1991;1061(1):56-64. doi:10.1016/0005-2736(91)90268-D

89. Tsoi KM, Macparland SA, Ma XZ, et al. Mechanism of hard-nanomaterial clearance by the liver. *Nat Mater*. 2016;15(11):1212-1221. doi:10.1038/nmat4718

90. Beningo KA, Wang YL. Fc-receptor-mediated phagocytosis is regulated by mechanical properties of the target. *J Cell Sci*. 2002;115(4):849-856. doi:10.1242/jcs.115.4.849

91. Hui Y, Wibowo D, Liu Y, et al. Understanding the Effects of Nanocapsular Mechanical Property on Passive and Active Tumor Targeting. *ACS Nano*. 2018;12(3):2846-2857. doi:10.1021/acsnano.8b00242

92. Stern T, Kaner I, Laser Zer N, et al. Rigidity of polymer micelles affects interactions with tumor cells. *J Control Release*. 2017;257:40-50. doi:10.1016/j.jconrel.2016.12.013

93. Yu M, Xu L, Tian F, et al. Rapid transport of deformation-tuned nanoparticles across biological hydrogels and cellular barriers. *Nat Commun*. 2018;9(1):2607. doi:10.1038/s41467-018-05061-3

94. Wang Y, Wang J, Zhu D, et al. Effect of physicochemical properties on in vivo fate of nanoparticle-based cancer immunotherapies. *Acta Pharm Sin B*. 2021;11(4):886-902. doi:10.1016/j.apsb.2021.03.007

95. Verma A, Stellacci F. Effect of surface properties on nanoparticle-cell interactions. *Small*. 2010;6(1):12-21. doi:10.1002/smll.200901158

96. Fischer HC, Hauck TS, Gómez-Aristizábal A, Chan WCW. Exploring primary liver macrophages for studying quantum dot interactions with biological systems. *Adv Mater*. 2010;22(23):2520-2524. doi:10.1002/adma.200904231

97. Lundqvist M, Stigler J, Elia G, Lynch I, Cedervall T, Dawson KA. Nanoparticle size and surface properties determine the protein corona with possible implications for biological impacts. *Proc Natl Acad Sci U S A*. 2008;105(38):14265-14270. doi:10.1073/pnas.0805135105

98. Salvati A, Pitek AS, Monopoli MP, et al. Transferrin-functionalized nanoparticles lose their targeting capabilities when a biomolecule corona adsorbs on the surface. *Nat Nanotechnol*. 2013;8:137-143. doi:10.1038/nnano.2012.237

99. Kreuter J. Influence of the surface properties on nanoparticle-mediated transport of drugs to the brain. *J Nanosci Nanotechnol*. 2004;4(5):484-488. doi:10.1166/jnn.2003.077

100. Alkilany AM, Zhu L, Weller H, et al. Ligand density on nanoparticles: A parameter with critical impact on nanomedicine. *Adv Drug Deliv Rev*. 2019;143:22-36. doi:10.1016/j.addr.2019.05.010

101. Myerson JW, Patel PN, Rubey KM, et al. Supramolecular arrangement of protein in nanoparticle structures predicts nanoparticle tropism for neutrophils in acute lung inflammation. *Nat Nanotechnol*. 2022;17:86-97. doi:10.1038/s41565-021-00997-y

102. Harder P, Grunze M, Dahint R, Whitesides GM, Laibinis PE. Molecular conformation in oligo(ethylene glycol)-terminated self-assembled monolayers on gold and silver surfaces determines their ability to resist protein adsorption. *J Phys Chem B*. 1998;102(2):426-436. doi:10.1021/jp972635z

103. Hu Y, Xie J, Tong YW, Wang CH. Effect of PEG conformation and particle size on the cellular uptake efficiency of nanoparticles with the HepG2 cells. *J Control Release*. 2007;118(1):7-17. doi:10.1016/j.jconrel.2006.11.028

104. Sant S, Poulin S, Hildgen P. Effect of polymer architecture on surface properties, plasma protein adsorption, and cellular interactions of pegylated nanoparticles. *J Biomed Mater Res - Part A*. 2008;87(4):885-895. doi:10.1002/jbm.a.31800

105. Verma A, Uzun O, Hu Y, et al. Surface-structure-regulated cell-membrane penetration by monolayer-protected nanoparticles. *Nat Mater*. 2008;7:588-595. doi:10.1038/nmat2202

106. Parodi A, Quattrocchi N, Van De Ven AL, et al. Synthetic nanoparticles functionalized with biomimetic leukocyte membranes possess cell-like functions. *Nat Nanotechnol*. 2013;8:61-68. doi:10.1038/nnano.2012.212

107. Hogrefe RI, Midthune B, Lebedev A. Current challenges in nucleic acid synthesis. *Isr J Chem*. 2013;53:326-349. doi:10.1002/ijch.201300032

108. Tuerk C, Gold L. Systematic evolution of ligands by exponential enrichment: RNA ligands to bacteriophage T4 DNA polymerase. *Science*. 1990;249(4968):505-510. doi:10.1126/science.2200121

109. Ellington, Andrew D. JWS. In vitro selection of RNA molecules that bind specific ligands. *Nature*. 1990;346(1):818-821. doi:10.1016/0021-9797(80)90501-9

110. O'Sullivan CK. Aptasensors – the future of biosensing? *Anal Bioanal Chem*. 2002;372(1):44-48. doi:10.1007/s00216-001-1189-3

111. Aldaye FA, Palmer AL, Sleiman HF. Assembling materials with DNA as the guide. *Science (80-)*. 2008;321(5897):1795-1799. doi:10.1126/science.1154533

112. Ariga K, Nakanishi T, Michinobu T. Immobilization of biomaterials to nano-assembled films (self-assembled monolayers, langmuir-blodgett films, and layer-by-layer assemblies) and their related functions. *J Nanosci Nanotechnol*. 2006;6(8):2278-2301. doi:10.1166/jnn.2006.503

113. Talap J, Zhao J, Shen M, et al. Recent advances in therapeutic nucleic acids and their analytical methods. *J Pharm Biomed Anal*. 2021;206:114368. doi:10.1016/j.jpba.2021.114368

114. Sridharan K, Gogtay NJ. Therapeutic nucleic acids: current clinical status. *Br J Clin Pharmacol*. 2016;82:659-672. doi:10.1111/bcp.12987

115. Vij M, Alam S, Gupta N, et al. Non-invasive Oil-Based Method to Increase Topical Delivery of Nucleic Acids to Skin. *Mol Ther*. 2017;25(6):1342-1352. doi:10.1016/j.ymthe.2017.03.009

116. Zakrewsky M, Kumar S, Mitragotri S. Nucleic acid delivery into skin for the treatment of skin disease: Proofs-of-concept, potential impact, and remaining challenges. *J Control Release*. 2015;219:445-456. doi:10.1016/j.jconrel.2015.09.017

117. Van den Boorn JG, Daßler J, Coch C, Schlee M, Hartmann G. Exosomes as nucleic acid nanocarriers. *Adv Drug Deliv Rev*. 2013;65(3):331-335. doi:10.1016/j.addr.2012.06.011

118. Mendes LP, Pan J, Torchilin VP. Dendrimers as nanocarriers for nucleic acid and drug delivery in cancer therapy. *Molecules*. 2017;22(9):1401-1422. doi:10.3390/molecules22091401

119. Johnson MB, Chandler M, Afonin KA. Nucleic acid nanoparticles (NANPs) as molecular tools to direct desirable and avoid undesirable immunological effects. *Adv Drug Deliv Rev*. 2021;173:427-438. doi:10.1016/j.addr.2021.04.011

120. Benson E, Mohammed A, Gardell J, et al. DNA rendering of polyhedral meshes at the nanoscale. *Nature*. 2015;523:441-444. doi:10.1038/nature14586

121. Veneziano R, Ratanalert S, Zhang K, et al. Designer nanoscale DNA assemblies programmed from the top down. *Science (80-)*. 2016;352(6293):1534. doi:10.1126/science.aaf4388

122. Cassinelli V, Oberleitner B, Sobotta J, et al. One-Step Formation of "chain-Armor"-Stabilized DNA Nanostructures. *Angew Chemie - Int Ed*. 2015;54(27):7795-7798. doi:10.1002/anie.201500561

123. Xu B, Wiehle S, Roth JA, Cristiano RJ. The contribution of poly-L-lysine, epidermal growth factor and streptavidin to EGF/PLL/DNA polyplex formation. *Gene Ther*. 1998;5(9):1235-1243. doi:10.1038/sj.gt.3300719

124. Katayose S, Kataoka K. Water-soluble polyion complex associates of DNA and poly(ethylene glycol)-poly(L-lysine) block copolymer. *Bioconjug Chem*. 1997;8(5):702-707. doi:10.1021/bc9701306

125. Ponnuswamy N, Bastings MMC, Nathwani B, et al. Oligolysine-based coating protects DNA nanostructures from low-salt denaturation and nuclease degradation. *Nat Commun*. 2017;8:15654. doi:10.1038/ncomms15654

126. Perrault SD, Shih WM. Virus-inspired membrane encapsulation of DNA nanostructures to achieve in vivo stability. *ACS Nano*. 2014;8(5):5132-5140. doi:10.1021/nn5011914

127. Kiviaho JK, Linko V, Ora A, et al. Cationic polymers for DNA origami coating-examining their binding efficiency and tuning the enzymatic reaction rates. *Nanoscale*. 2016;8(22):11674-11680. doi:10.1039/c5nr08355a

128. Jin R, Wu G, Li Z, Mirkin CA, Schatz GC. What Controls the Melting Properties of DNA-Linked Gold Nanoparticle Assemblies?*. *J Am Chem Soc*. 2003;125(6):1643-1654. doi:10.1201/9781003056676-12

129. Seferos DS, Prigodich AE, Giljohann DA, Patel PC, Mirkin CA. Polyvalent DNA nanoparticle conjugates stabilize nucleic acids. *Nano Lett*. 2009;9(1):308-311. doi:10.1021/nl802958f

130. Cutler JI, Zhang K, Zheng D, Auyeung E, Prigodich AE, Mirkin CA. Polyvalent nucleic acid nanostructures. *J Am Chem Soc*. 2011;133(24):9254-9257. doi:10.1021/ja203375n

131. Lee H, Lytton-Jean AKR, Chen Y, et al. Molecularly self-assembled nucleic acid nanoparticles for targeted in vivo siRNA delivery. *Nat Nanotechnol*. 2012;7:389-393. doi:10.1038/nnano.2012.73

132. Mikkilä J, Eskelinen AP, Niemelä EH, et al. Virus-encapsulated DNA origami nanostructures for cellular delivery. *Nano Lett*. 2014;14(4):2196-2200. doi:10.1021/nl500677j

133. Jasinski DL, Li H, Guo P. The Effect of Size and Shape of RNA Nanoparticles on Biodistribution. *Mol Ther*. 2018;26(3):784-792. doi:10.1016/j.ymthe.2017.12.018

134. Ghimire C, Wang H, Li H, Vieweger M, Xu C, Guo P. RNA nanoparticles as rubber for compelling vessel extravasation to enhance tumor targeting and for fast renal excretion to reduce toxicity. *ACS Nano*. 2020;14(10):13180-13191. doi:10.1021/acsnano.0c04863

135. Erts D, Polyakov B, Olin H, Tuite E. Spatial and mechanical properties of dilute DNA monolayers on gold imaged by AFM. *J Phys Chem B*. 2003;107(15):3591-3597. doi:10.1021/jp0261657

136. Lytton-Jean AKR, Mirkin CA. A thermodynamic investigation into the binding properties of DNA functionalized gold nanoparticle probes and molecular fluorophore probes. *J Am Chem Soc*. 2005;127(37):12754-12755. doi:10.1021/ja052255o

137. Rosi NL. Oligonucleotide-Modified Gold Nanoparticles for Intracellular Gene Regulation. *Science (80-).* 2006;312(5776):1027-1030. doi:10.1126/science.1125559

138. Choi CHJ, Hao L, Narayan SP, Auyeung E, Mirkin CA. Mechanism for the Endocytosis of Spherical Nucleic Acid Nanoparticle Conjugates. *PNAS*. 2013;110(19):7625-7630. doi:10.1201/9781003056676-21

139. Giljohann DA, Seferos DS, Patel PC, Millstone JE, Rosi NL, Mirkin CA. Oligonucleotide Loading Determines Cellular Uptake of DNA-Modified Gold Nanoparticles*. *Nano Lett*. 2007;7(12):3818-3821. doi:10.4324/9780429200151-17

140. Williams SCP. Spherical nucleic acids: A whole new ball game. *Proc Natl Acad Sci U S A*. 2013;110(33):13231-13233. doi:10.1073/pnas.1313483110

141. Zheng D, Giljohann DA, Chen DL, et al. Topical Delivery of siRNA-Based Spherical Nucleic Acid Nanoparticle Conjugates for Gene Regulation. *Spherical Nucleic Acids*. 2012;109(30):11975-11980. doi:10.1201/9781003056713-17

142. Melamed JR, Kreuzberger NL, Goyal R, Day ES. Spherical Nucleic Acid Architecture Can Improve the Efficacy of Polycation-Mediated siRNA Delivery. *Mol Ther - Nucleic Acids*. 2018;12:207-219. doi:10.1016/j.omtn.2018.05.008

143. Kato H, Takeuchi O, Mikamo-Satoh E, et al. Length-dependent recognition of double-stranded ribonucleic acids by retinoic acid-inducible gene-I and melanoma differentiation-associated gene 5. *J Exp Med*. 2008;205(7):1601-1610. doi:10.1084/jem.20080091

144. D.M. K. Immunotherapeutic uses of CpG oligodeoxynucleotides. *Nat Rev Immunol*. 2004;4:249-258.

145. Li Y, Berke IC, Modis Y. DNA binding to proteolytically activated TLR9 is sequence-independent and enhanced by DNA curvature. *EMBO J*. 2012;31(4):919-931. doi:10.1038/emboj.2011.441

146. Civril F, Deimling T, De Oliveira Mann CC, et al. Structural mechanism of cytosolic DNA sensing by cGAS. *Nature*. 2013;498:332-337. doi:10.1038/nature12305

147. Hong E, Halman JR, Shah A, et al. Toll-like receptor-mediated recognition of nucleic acid nanoparticles (NANPs) in human primary blood cells. *Molecules*. 2019;24(6):1094. doi:10.3390/molecules24061094

148. Hong E, Halman JR, Shah AB, Khisamutdinov EF, Dobrovolskaia MA, Afonin KA. Structure and Composition Define Immunorecognition of Nucleic Acid Nanoparticles. *Nano Lett*. 2018;18(7):4309-4321. doi:10.1021/acs.nanolett.8b01283

149. Khisamutdinov EF, Li H, Jasinski DL, Chen J, Fu J, Guo P. Enhancing immunomodulation on innate immunity by shape transition among RNA triangle, square and pentagon nanovehicles. *Nucleic Acids Res*. 2014;42(15):9996-10004. doi:10.1093/nar/gku516

150. Guo S, Li H, Ma M, Fu J, Dong Y, Guo P. Size, Shape, and Sequence-Dependent Immunogenicity of RNA Nanoparticles. *Mol Ther - Nucleic Acids*. 2017;9:399-408. doi:10.1016/j.omtn.2017.10.010

151. Massich MD, Giljohann DA, Seferos DS, Ludlow LE, Horvath CM, Mirkin CA. Regulating immune response using polyvalent nucleic acid-gold nanoparticle conjugates. *Mol Pharm*. 2009;6(6):1934-1940. doi:10.1021/mp900172m

152. Pallares RM, Choo P, Cole LE, Mirkin CA, Lee A, Odom TW. Manipulating immune activation of macrophages by tuning the oligonucleotide composition of gold nanoparticles. *Bioconjug Chem*. 2019;30(7):2032-2037. doi:10.1021/acs.bioconjchem.9b00316

153. Wang S, Qin L, Yamankurt G, et al. Rational vaccinology with spherical nucleic acids. *Proc Natl Acad Sci U S A*. 2019;116(21):10473-10481. doi:10.1073/pnas.1902805116

154. Teplensky MH, Dittmar JW, Qin L, et al. Spherical Nucleic Acid Vaccine Structure Markedly Influences Adaptive Immune Responses of Clinically Utilized Prostate Cancer Targets. *Adv Healthc Mater*. 2021;10(22):2101262. doi:10.1002/adhm.202101262

155. Chen Y, Chen H, Shi J. Inorganic nanoparticle-based drug codelivery nanosystems to overcome the multidrug resistance of cancer cells. *Mol Pharm*. 2014;11(8):2495-2510. doi:10.1021/mp400596v

156. Vargason AM, Anselmo AC, Mitragotri S. The evolution of commercial drug delivery technologies. *Nat Biomed Eng*. 2021;5:951-967. doi:10.1038/s41551-021-00698-w

157. Moghimi SM, Hunter AC, Murray JC. Long-circulating and target-specific nanoparticles: Theory to practice. *Pharmacol Rev*. 2001;53(2):283-318.

158. Sarode A, Annapragada A, Guo J, Mitragotri S. Layered self-assemblies for controlled drug delivery: A translational overview. *Biomaterials*. 2020;242:119929. doi:10.1016/j.biomaterials.2020.119929

159. Goodman AM, Hogan NJ, Gottheim S, Li C, Clare SE, Halas NJ. Understanding Resonant Light-Triggered DNA Release from Plasmonic Nanoparticles. *ACS Nano*. 2017;11(1):171-179. doi:10.1021/acsnano.6b06510

160. Sellner S, Kocabey S, Zhang T, et al. Dexamethasone-conjugated DNA nanotubes as anti-inflammatory agents in vivo. *Biomaterials*. 2017;134:78-90. doi:10.1016/j.biomaterials.2017.04.031

161. Song L, Ho VHB, Chen C, et al. Efficient, pH-Triggered Drug Delivery Using a pH-Responsive DNA-Conjugated Gold Nanoparticle. *Adv Healthc Mater*. 2013;2(2):275-280. doi:10.1002/adhm.201200112

162. Awino JK, Gudipati S, Hartmann AK, et al. Nucleic Acid Nanocapsules for Enzyme-Triggered Drug Release. *J Am Chem Soc*. 2017;139(18):6278-6281. doi:10.1021/jacs.6b13087

163. Yu Z, Li N, Zheng P, Pan W, Tang B. Temperature-responsive DNA-gated nanocarriers for intracellular controlled release. *Chem Commun*. 2014;50(26):3494-3497. doi:10.1039/C3CC49183H

164. Chen WH, Karmi O, Willner B, Nechushtai R, Willner I. Thrombin aptamer-modified metal–organic framework nanoparticles: Functional nanostructures for sensing thrombin and the triggered controlled release of anti-blood clotting drugs. *Sensors (Switzerland)*. 2019;19(23):5260. doi:10.3390/s19235260

165. Zhang P, Fischer A, Ouyang Y, et al. Aptamer-modified DNA tetrahedra-gated metal-organic framework nanoparticle carriers for enhanced chemotherapy or photodynamic therapy. *Chem Sci*. 2021;12(43):14473-14483. doi:10.1039/d1sc04229g

166. Engelen W, Sigl C, Kadletz K, Willner EM, Dietz H. Antigen-Triggered Logic-Gating of DNA Nanodevices. *J Am Chem Soc*. 2021;143(51):21630-21636. doi:10.1021/jacs.1c09967

167. Chen WH, Yang Sung S, Fadeev M, Cecconello A, Nechushtai R, Willner I. Targeted VEGF-triggered release of an anti-cancer drug from aptamer-functionalized metal-organic framework nanoparticles. *Nanoscale*. 2018;10(10):4650-4657. doi:10.1039/c8nr00193f

168. Mosley RJ, Hart J, Davis KL, Wower J, Byrne ME. Tailored Nucleic Acid Architectures at Gold Surfaces for Controlled Therapeutic Release. *Langmuir*. 2022;38(5):1698-1704. doi:10.1021/acs.langmuir.1c02718

169. Dahotre SN, Chang YM, Wieland A, Stammen SR, Kwong GA. Individually addressable and dynamic DNA gates for multiplexed cell sorting. *Proc Natl Acad Sci U S A*. 2018;115(17):4357-4362. doi:10.1073/pnas.1714820115

170. Pu F, Liu Z, Ren J, Qu X. Nucleic acid–mesoporous silica nanoparticle conjugates for keypad lock security operation. *Chem Commun*. 2013;49(23):2305-2307. doi:10.1039/c3cc38883b

171. Wang D, Li S, Zhao Z, Zhang X, Tan W. Engineering a Second-Order DNA Logic-Gated Nanorobot to Sense and Release on Live Cell Membranes for Multiplexed Diagnosis and Synergistic Therapy. *Angew Chemie - Int Ed*. 2021;60(29):15816-15820. doi:10.1002/anie.202103993

172. Whitener R, Mosley RJ, Wower J, Byrne ME. Nucleic acid biohybrid nanocarriers with high-therapeutic payload and controllable extended release of daunomycin for cancer therapy. *J Biomed Mater Res - Part A*. 2021;109(7):1256-1265. doi:10.1002/jbm.a.37119

173. Zhang J, Salaita K. Smart Nucleic Acids as Future Therapeutics. *Trends Biotechnol*. 2021;39(12):1289-1307. doi:10.1016/j.tibtech.2021.03.007

174. Kumthekar P, Ko CH, Paunesku T, et al. A first-in-human phase 0 clinical study of RNA interference-based spherical nucleic acids in patients with recurrent glioblastoma. *Sci Transl Med*. 2021;13(584):eabb3945. doi:10.1126/scitranslmed.abb3945

175. Bharali DJ, Khalil M, Gurbuz M, Simone TM, Mousa SA. Nanoparticles and cancer therapy: A concise review with emphasis on dendrimers. *Int J Nanomedicine*. 2009;4(1):1-7.

176. Bourne RRA, Steinmetz JD, Saylan M, et al. Causes of blindness and vision impairment in 2020 and trends over 30 years, and prevalence of avoidable blindness in relation to VISION 2020: The Right to Sight: An analysis for the Global Burden of Disease Study. *Lancet Glob Heal*. 2021;9(2):144-160. doi:10.1016/S2214-109X(20)30489-7

177. Foster A. Vision 2020: The Cataract Challenge. *Community Eye Heal*. 2000;13(34):17-19. Accessed August 13, 2021. /pmc/articles/PMC1705965/

178. Organization WH. *Universal Eye Health: A Global Action Plan 2014-2019*.; 2013.

179. Flaxman SR, Bourne RRA, Resnikoff S, et al. Global causes of blindness and distance vision impairment 1990–2020: a systematic review and meta-analysis. *Lancet Glob Heal*. 2017;5(12):e1221-e1234. doi:10.1016/S2214-109X(17)30393-5

180. Lansingh VC, Carter MJ, Martens M. Global Cost-effectiveness of Cataract Surgery. *Ophthalmology*. 2007;114(9):1670-1678. doi:10.1016/J.OPHTHA.2006.12.013

181. Yorston D. Cataract complications. *Community Eye Heal J*. 2008;21(65):1-3.

182. Raj SM, Vasavada AR, Johar SRK, Vasavada VA, Vasavada VA. Post-Operative Capsular Opacification: A Review. *Int J Biomed Sci*. 2007;3(4):237-250. Accessed August 13, 2021. /pmc/articles/PMC3614664/

183. Awasthi N, Guo S, Wagner BJ. Posterior capsular opacification: A problem reduced but not yet eradicated. *Arch Ophthalmol*. 2009;127(4):555-562. doi:10.1001/archophthalmol.2009.3

184. Aron-Rosa D, Aron JJ, Griesemann M, Thyzel R. Use of the neodymium-yag laser to open the posterior capsule after lens implant surgery: a preliminary report. *Am Intra-Ocular Implant Soc J*. 1980;6(4):352-354. doi:10.1016/S0146-2776(80)80036-X

185. Ursell PG, Dhariwal M, O'Boyle D, Khan J, Venerus A. 5 year incidence of YAG capsulotomy and PCO after cataract surgery with single-piece monofocal intraocular lenses: a real-world evidence study of 20,763 eyes. *Eye*. 2019;34:960-968. doi:10.1038/s41433-019-0630-9

186. Parajuli A, Joshi P, Subedi P, Pradhan C. Effect of Nd:YAG laser posterior capsulotomy on intraocular pressure, refraction, anterior chamber depth, and macular thickness. *Clin Ophthalmol*. 2019;13:945-952. doi:10.2147/OPTH.S203677

187. Wesolosky JD, Tennant M, Rudnisky CJ. Rate of retinal tear and detachment after neodymium:YAG capsulotomy. *J Cataract Refract Surg*. 2017;43(7):923-928. doi:10.1016/J.JCRS.2017.03.046

188. Glacet-Bernard A, Brahim R, Mokhtari O, Quentel G, Coscas G. Retinal detachment following posterior capsulotomy using Nd:YAG laser. Retrospective study of 144 capsulotomies. *J Fr Ophtalmol*. 1993;16(2):87-94. Accessed August 13, 2021. https://europepmc.org/article/med/8496561

189. Pérez-Vives C. Biomaterial Influence on Intraocular Lens Performance: An Overview. *J Ophthalmol*. Published online March 15, 2018. doi:10.1155/2018/2687385

190. Aliancy J, Werner L, Ludlow J, et al. Long-term capsule clarity with a disk-shaped intraocular lens. *J Cataract Refract Surg*. 2018;44(4):504-509. doi:10.1016/j.jcrs.2017.12.029

191. Rabinovich M, Niegowski LJ, Bovet J, Aramburu del Boz A, Baumgartner J-M, Gillmann K. Comparison of posterior capsule opacification rates between femto-second laser-assisted and micro-incision cataract surgery over 24 months. *Spektrum der Augenheilkd*. Published online June 25, 2021:1-5. doi:10.1007/S00717-021-00491-9

192. Wormstone IM, Wormstone YM, Smith AJO, Eldred JA. Posterior capsule opacification: What's in the bag? *Prog Retin Eye Res*. 2021;82. doi:10.1016/J.PRETEYERES.2020.100905

193. Nibourg LM, Gelens E, Kuijer R, Hooymans JMM, van Kooten TG, Koopmans SA. Prevention of posterior capsular opacification. *Exp Eye Res*. 2015;136:100-115. doi:10.1016/J.EXER.2015.03.011

194. Gerhart J, Greenbaum M, Scheinfeld V, et al. Myo/Nog cells: Targets for preventing the accumulation of skeletal muscle-like cells in the human lens. *PLoS One*. 2014;9(4). doi:10.1371/journal.pone.0095262

195. Gerhart J, Greenbaum M, Casta L, et al. Antibody-conjugated, DNA-based nanocarriers intercalated with doxorubicin eliminate myofibroblasts in explants of human lens tissue. *J Pharmacol Exp Ther*. 2017;361(1):60-67. doi:10.1124/jpet.116.239079

196. Gerhart J, Werner L, Mamalis N, et al. Depletion of Myo/Nog cells in the lens mitigates posterior capsule opacification in rabbits. *Investig Ophthalmol Vis Sci*. 2019;60(6):1813-1823. doi:10.1167/iovs.19-26713

197. Gerhart J, Elder J, Neely C, et al. MyoD-positive epiblast cells regulate skeletal muscle differentiation in the embryo. *J Cell Biol*. 2006;175(2):283-292. doi:10.1083/jcb.200605037

198. Gerhart J, Baytion M, DeLuca S, et al. DNA dendrimers localize MyoD mRNA in presomitic tissues of the chick embryo. *J Cell Biol*. 2000;149(4):825-833. doi:10.1083/jcb.149.4.825

199. Gerhart J, Pfautz J, Neely C, et al. Noggin producing, MyoD-positive cells are crucial for eye development. *Dev Biol*. 2009;336(1):30-41. doi:10.1016/j.ydbio.2009.09.022

200. Gerhart J, Bowers J, Gugerty L, et al. Brain-specific angiogenesis inhibitor 1 is expressed in the Myo/Nog cell lineage. *PLoS One*. 2020;15(7). doi:10.1371/journal.pone.0234792

201. Gerhart J, Neely C, Elder J, et al. Cells that express MyoD mRNA in the epiblast are stably committed to the skeletal muscle lineage. *J Cell Biol*. 2007;178(4):649-660. doi:10.1083/jcb.200703060

202. Gerhart J, Scheinfeld VL, Milito T, et al. Myo/Nog cell regulation of bone morphogenetic protein signaling in the blastocyst is essential for normal morphogenesis and striated muscle lineage specification. *Dev Biol*. 2011;359(1):12-25. doi:10.1016/J.YDBIO.2011.08.007

203. Gwon A. The Rabbit in Cataract/IOL Surgery. In: *Animal Models in Eye Research*. Academic Press; 2008:184-204. doi:10.1016/B978-0-12-374169-1.00013-8

204. Gerhart J, Withers C, Gerhart C, et al. Myo/Nog cells are present in the ciliary processes, on the zonule of Zinn and posterior capsule of the lens following cataract surgery. *Exp Eye Res*. 2018;171:101-105. doi:10.1016/j.exer.2018.03.016

205. Gerhart J, Behling K, Paessler M, et al. Rhabdomyosarcoma and Wilms tumors contain a subpopulation of noggin producing, myogenic cells immunoreactive for lens beaded filament proteins. *PLoS One*. 2019;14(4). doi:10.1371/journal.pone.0214758

206. Osorno LL, Medina JDR, Maldonado DE, Mosley RJ, Byrne ME. Extended Release of Doxorubicin-Loaded 3DNA Nanocarriers from In-Situ Forming, Self-Assembled Hydrogels. *J Ocul Pharmacol Ther*. 2020;36(6):447-457. doi:10.1089/jop.2019.0145

207. Nilsen TW, Grayzel J, Prensky W. Dendritic nucleic acid structures. *J Theor Biol*. 1997;187(2):273-284. doi:10.1006/jtbi.1997.0446

208. Wang J, Jiang M. Dendritic Nucleic Acid Probes for DNA Biosensors. *J Am Chem Soc*. 1998;120(11):8281-8282.

209. Osorno LL, Maldonado DE, Whitener RJ, et al. Amphiphilic PLGA-PEG-PLGA triblock copolymer nanogels varying in gelation temperature and modulus for the extended and controlled release of hyaluronic acid. *J Appl Polym Sci*. 2020;137(25). doi:10.1002/app.48678

210. Lee VHL, Robinson JR. Topical Ocular Drug Delivery: Recent Developments and Future Challenges. *J Ocul Pharmacol*. 1986;2(1):67-108. doi:10.1089/jop.1986.2.67

211. Gote V, Sikder S, Sicotte J, Pal D. Ocular drug delivery: Present innovations and future challenges. *J Pharmacol Exp Ther*. 2019;370(3):602-624. doi:10.1124/jpet.119.256933

212. Andrés-Guerrero V, Bravo-Osuna I, Pastoriza P, Molina-Martinez IT, Herrero-Vanrell R. Novel technologies for the delivery of ocular therapeutics in glaucoma. *J Drug Deliv Sci Technol*. 2017;42:181-192. doi:10.1016/j.jddst.2017.07.001

213. Krag S, Andreassen TT. Mechanical properties of the human lens capsule. *Prog Retin Eye Res*. 2003;22(6):749-767. doi:10.1016/S1350-9462(03)00063-6

214. Barar J, Asadi M, Mortazavi-Tabatabaei SA, Omidi Y. Ocular drug delivery; Impact of in vitro cell culture models. *J Ophthalmic Vis Res*. 2014;4(4):238-252. doi:10.1007/978-3-319-29346-2_21

215. Torres-Luna C, Fan X, Domszy R, Hu N, Wang NS, Yang A. Hydrogel-based ocular drug delivery systems for hydrophobic drugs. *Eur J Pharm Sci*. 2020;154. doi:10.1016/j.ejps.2020.105503

216. Grimaudo MA, Pescina S, Padula C, et al. Topical application of polymeric nanomicelles in ophthalmology: a review on research efforts for the noninvasive delivery of ocular therapeutics. *Expert Opin Drug Deliv*. 2019;16(4):397-413. doi:10.1080/17425247.2019.1597848

217. Bisht R, Mandal A, Jaiswal JK, Rupenthal ID. Nanocarrier mediated retinal drug delivery: overcoming ocular barriers to treat posterior eye diseases. *Wiley Interdiscip Rev Nanomedicine Nanobiotechnology*. 2018;10(2):e1473. doi:10.1002/wnan.1473

218. Mandal A, Pal D, Agrahari V, Trinh HM, Joseph M, Mitra AK. Ocular delivery of proteins and peptides: Challenges and novel formulation approaches. *Adv Drug Deliv Rev*. 2018;126:67-95. doi:10.1016/j.addr.2018.01.008

219. Irimia T, Dinu-Pîrvu CE, Ghica MV, et al. Chitosan-based in situ gels for ocular delivery of therapeutics: A state-of-the-art review. *Mar Drugs*. 2018;16(10). doi:10.3390/md16100373

220. Souto EB, Dias-Ferreira J, López-Machado A, et al. Advanced formulation approaches for ocular drug delivery: State-of-the-art and recent patents. *Pharmaceutics*. 2019;11(9). doi:10.3390/pharmaceutics11090460

221. Chan PS, Xian JW, Li Q, Chan CW, Leung SSY, To KKW. Biodegradable Thermosensitive PLGA-PEG-PLGA Polymer for Non-irritating and Sustained Ophthalmic Drug Delivery. *AAPS J*. 2019;21(4). doi:10.1208/s12248-019-0326-x

222. Thackaberry EA, Lorget F, Farman C, Bantseev V. The safety evaluation of long-acting ocular delivery systems. *Drug Discov Today*. 2019;24(8):1539-1550. doi:10.1016/j.drudis.2019.05.032

223. Chang E, J. McClellan A, J. Farley W, Quan Li D-. Biodegradable PLGA-Based Drug Delivery Systems for Modulating Ocular Surface Disease under Experimental Murine Dry Eye. *J Clin Exp Ophthalmol*. 2011;02(11). doi:10.4172/2155-9570.1000191

224. McKenzie M, Betts D, Suh A, et al. Proof-of-Concept of Polymeric Sol-Gels in Multi-Drug Delivery and Intraoperative Image-Guided Surgery for Peritoneal Ovarian Cancer. *Pharm Res*. 2016;33(9):2298-2306. doi:10.1007/s11095-016-1968-3

225. Samoylov A, Cochran A, Schemera B, et al. Humoral immune responses against gonadotropin releasing hormone elicited by immunization with phage-peptide constructs obtained via phage display. *J Biotechnol*. 2015;216:20-28. doi:10.1016/j.jbiotec.2015.10.001

226. Horowitz LF, Rodriguez AD, Ray T, Folch A. Microfluidics for interrogating live intact tissues. *Microsystems Nanoeng*. 2020;6(1). doi:10.1038/s41378-020-0164-0

227. Bai J, Wang C. Organoids and Microphysiological Systems: New Tools for Ophthalmic Drug Discovery. *Front Pharmacol*. 2020;11. doi:10.3389/fphar.2020.00407

228. Wu Q, Liu J, Wang X, et al. Organ-on-a-chip: Recent breakthroughs and future prospects. *Biomed Eng Online*. 2020;19(1). doi:10.1186/s12938-020-0752-0

229. Code Biotherapeutics Announces Collaboration with Takeda to Use Proprietary 3DNA Genetic Medicine Delivery Platform to Design and Develop Gene Therapies for Rare Diseases. BUSINESS WIRE. Published 2022. Accessed May 4, 2022. https://www.businesswire.com/news/home/20220222005249/en/Code-Biotherapeutics-Announces-Collaboration-with-Takeda-to-Use-Proprietary-3DNA-Genetic-Medicine-Delivery-Platform-to-Design-and-Develop-Gene-Therapies-for-Rare-Diseases

230. Song C, Ouyang Z, Guo H, et al. Core-shell tecto dendrimers enable enhanced tumor MR imaging through an amplified EPR effect. *Biomacromolecules*. 2021;22(5):2181-2188. doi:10.1021/acs.biomac.1c00262

231. Mirkin CA, Letsinger RL, Mucic RC, Storhoff JJ. A DNA-based method for rationally assembling nanoparticles into macroscopic materials. *Nature*. 1996;382(6592):607-609. doi:10.1038/382607a0

232. Sundaram P, Wower J, Byrne ME. A nanoscale drug delivery carrier using nucleic acid aptamers for extended release of therapeutic. *Nanomedicine Nanotechnology, Biol Med*. 2012;8(7):1143-1151. doi:10.1016/j.nano.2012.01.010

233. Dias AP, da Silva Santos S, da Silva JV, et al. Dendrimers in the context of nanomedicine. *Int J Pharm*. 2020;573(118814). doi:10.1016/j.ijpharm.2019.118814

234. Liu L, Han L, Wu Q, et al. Multifunctional DNA dendrimer nanostructures for biomedical applications. *J Mater Chem B*. 2021;9(25):4991-5007. doi:10.1039/d1tb00689d

235. Auvinen H, Zhang H, Nonappa, et al. Protein Coating of DNA Nanostructures for Enhanced Stability and Immunocompatibility. *Adv Healthc Mater*. 2017;6(18):1700692. doi:10.1002/adhm.201700692

236. Keller A, Linko V. Challenges and Perspectives of DNA Nanostructures in Biomedicine. *Angew Chemie - Int Ed*. 2020;59(37):15818-15833. doi:10.1002/anie.201916390

237. Li F, Lyu D, Liu S, Guo W. DNA Hydrogels and Microgels for Biosensing and Biomedical Applications. *Adv Mater*. 2020;32(3):1806538. doi:10.1002/adma.201806538

238. Carabineiro SAC. Applications of gold nanoparticles in nanomedicine: Recent advances in vaccines. *Molecules*. 2017;22(5):857. doi:10.3390/molecules22050857

239. Hurst SJ, Lytton-Jean AKR, Mirkin CA. Maximizing DNA loading on a range of gold nanoparticle sizes. *Anal Chem*. 2006;78(24):8313-8318. doi:10.1021/ac0613582

240. Sauerbrey G. Verwendung von Schwingquarzen zur Wägung dünner Schichten und zur Mikrowägung. *Zeitschrift für Phys*. 1959;155(2):206-222. doi:10.1007/BF01337937

241. Voinova M V, Rodahl M, Jonson M, Kasemo B. Viscoelastic Acoustic Response of Layered Polymer Films at Fluid-Solid Interfaces: Continuum Mechanics Approach. *Phys Scr*. 1999;59(5):391-396. doi:10.1238/physica.regular.059a00391

242. Chi Q, Wang G, Jiang J. The persistence length and length per base of single-stranded DNA obtained from fluorescence correlation spectroscopy measurements using mean field theory. *Phys A Stat Mech its Appl*. 2013;392(5):1072-1079. doi:10.1016/j.physa.2012.09.022

243. Singh A, Snyder S, Lee L, Johnston APR, Caruso F, Yingling YG. Effect of oligonucleotide length on the assembly of DNA materials: Molecular dynamics simulations of layer-by-layer DNA films. *Langmuir*. 2010;26(22):17339-17347. doi:10.1021/la102762t

244. Kelley SO, Hill MG, Barton JK, et al. Orienting DNA Helices on Gold Using Applied Electric Fields. *Langmuir*. 1998;14(24):6781-6784.

245. Tajik-Ahmadabad B, Mechler A, Muir BW, et al. A QCM-D and SAXS Study of the Interaction of Functionalised Lyotropic Liquid Crystalline Lipid Nanoparticles with siRNA. *ChemBioChem*. 2017;18(10):921-930. doi:10.1002/cbic.201600613

246. Liu SX, Kim JT. Application of Kevin—Voigt Model in Quantifying Whey Protein Adsorption on Polyethersulfone Using QCM-D. *J Lab Autom*. 2009;14(4):213-220. doi:10.1016/j.jala.2009.01.003

247. Ross PD, Scruggs RL. Viscosity study of DNA. II. The effect of simple salt concentration on the viscosity of high molecular weight DNA and application of viscometry to the study of DNA isolated from T4 and T5 bacteriophage mutants. *Biopolymers*. 1968;6(8):1005-1018. doi:10.1002/bip.1968.360060802

248. Levicky R, Herne TM, Tarlov MJ, Satija SK. Using self-assembly to control the structure of DNA monolayers on gold: A neutron reflectivity study. *J Am Chem Soc*. 1998;120(38):9787-9792. doi:10.1021/ja981897r

249. Tsortos A, Papadakis G, Mitsakakis K, Melzak KA, Gizeli E. Quantitative determination of size and shape of surface-bound DNA using an acoustic wave sensor. *Biophys J*. 2008;94(7):2706-2715. doi:10.1529/biophysj.107.119271

250. Stengel G, Höök F, Knoll W. Viscoelastic modeling of template-directed DNA synthesis. *Anal Chem*. 2005;77(11):3709-3714. doi:10.1021/ac048302x

251. Kroy K. Elasticity, dynamics and relaxation in biopolymer networks. *Curr Opin Colloid Interface Sci*. 2006;11(1):56-64. doi:10.1016/j.cocis.2005.10.001

252. Balakrishnan B, Banerjee R. Biopolymer-Based Hydrogels for Cartilage Tissue Engineering. *Chem Rev*. 2011;111:4453-4474. doi:10.1021/cr100123h

253. Tanaka M, Hayashi T, Morita S. The roles of water molecules at the biointerface of medical polymers. *Polym J*. 2013;45(7):701-710. doi:10.1038/pj.2012.229

254. Rant U, Arinaga K, Tornow M, et al. Dissimilar kinetic behavior of electrically manipulated single- and double-stranded DNA tethered to a gold surface. *Biophys J*. 2006;90(10):3666-3671. doi:10.1529/biophysj.105.078857

255. Hill HD, Millstone JE, Banholzer MJ, Mirkin CA. The role radius of curvature plays in thiolated oligonucleotide loading on gold nanoparticles. *ACS Nano*. 2009;3(2):418-424. doi:10.1021/nn800726e

256. Yun YH, Lee BK, Park K. Controlled Drug Delivery: Historical perspective for the next generation. *J Control Release*. 2015;219:2-7. doi:10.1016/j.jconrel.2015.10.005

257. Anselmo AC, Mitragotri S. Nanoparticles in the clinic: An update. *Bioeng Transl Med*. 2019;4(3):e10143. doi:10.1002/btm2.10143

258. Din FU, Aman W, Ullah I, et al. Effective use of nanocarriers as drug delivery systems for the treatment of selected tumors. *Int J Nanomedicine*. 2017;12:7291-7309. doi:10.2147/IJN.S146315

259. E. Azhdaria, Emamib A, Ferreira JA. Drug release from a surface erosion biodegradable viscoelastic polymeric platform: Analysis and numerical simulation. *Comput Math with Appl*. 2020;80(12):3004-3026.

260. Hussain M, Xie J, Hou Z, et al. Regulation of Drug Release by Tuning Surface Textures of Biodegradable Polymer Microparticles. *ACS Appl Mater Interfaces*. 2017;9(16):14391–14400.

261. Yarce CJ, Echeverri JD, Palacio MA, Rivera CA, Salamanca CH. Relationship between Surface Properties and In Vitro Drug Release from Compressed Matrix Containing Polymeric Materials with Different Hydrophobicity Degrees. *Pharmaceuticals*. 2017;10(1):15.

262. Cheng Y, Samia AC, Li J, Kenney ME, Resnick A, Burda C. Delivery and Efficacy of a Cancer Drug as a Function of the Bond to the Gold Nanoparticle Surface. *Langmuir*. 2010;26(4):2248-2255.

263. Xu W, He W, Du Z, et al. Functional Nucleic Acid-Nanomaterials: Development, Properties, and Applications. *Angew Chem Int Ed*. 2021;60:6890.

264. Lv Z, Zhu Y, Li F. DNA Functional Nanomaterials for Controlled Delivery of Nucleic Acid-Based Drugs. *Front Bioeng Biotechnol*. 2021;9:720291. doi:10.3389/fbioe.2021.720291

265. Tjong V, Tang L, Zauscher S, Chilkoti A. "Smart" DNA interfaces. *Chem Soc Rev*. 2014;43(5):1612-1626. doi:10.1039/c3cs60331h

266. Chandler M, Afonin KA. Smart-responsive Nucleic Acid Nanoparticles (NANPs) with the potential to modulate immune behavior. *Nanomaterials*. 2019;9(4):611. doi:10.3390/nano9040611

267. Whitener R, Mosley RJ, Wower J, Byrne ME. Nucleic acid biohybrid nanocarriers with high-therapeutic payload and controllable extended release of daunomycin for cancer therapy. *J Biomed Mater Res - Part A*. Published online October 26, 2020. doi:10.1002/jbm.a.37119

268. Ariga K, Leong DT, Mori T. Nanoarchitectonics for Hybrid and Related Materials for Bio-Oriented Applications. *Adv Funct Mater*. 2018;28:1702905. doi:10.1002/adfm.201702905

269. Rao AN, Grainger DW. Biophysical Properties of Nucleic Acids At Surfaces Relevant To Microarray Performance. *Biomater Sci*. 2014;2(4):436-471. doi:10.1039/C3BM60181A

270. Roth E, Glick Azaria A, Girshevitz O, Bitler A, Garini Y. Measuring the Conformation and Persistence Length of Single-Stranded DNA Using a DNA Origami Structure. *Nano Lett*. 2018;18(11):6703-6709. doi:10.1021/acs.nanolett.8b02093

271. Brown KA, Park S, Hamad-Schifferli K. Nucleotide-surface interactions in DNA-modified Au-nanoparticle conjugates: Sequence effects on reactivity and hybridization. *J Phys Chem C*. 2008;112(20):7517-7521. doi:10.1021/jp711869p

272. Parak WJ, Pellegrino T, Micheel CM, Gerion D, Williams SC, Alivisatos AP. Conformation of oligonucleotides attached to gold nanocrystals probed by gel electrophoresis. *Nano Lett*. 2003;3(1):33-36. doi:10.1021/nl025888z

273. Ambia-Garrido J, Vainrub A, Pettitt BM. A model for structure and thermodynamics of ssDNA and dsDNA near a surface: A coarse grained approach. *Comput Phys Commun*. 2010;181(12):2001-2007. doi:10.1016/j.cpc.2010.08.029

274. Razumovitch J, De França K, Kehl F, Wiki M, Meier W, Vebert C. Optimal hybridization efficiency upon immobilization of oligonucleotide double helices. *J Phys Chem B*. 2009;113(24):8383-8390. doi:10.1021/jp902383m

275. Chen C, Geng J, Pu F, Yang X, Ren J, Qu X. Polyvalent Nucleic Acid/Mesoporous Silica Nanoparticle Conjugates: Dual Stimuli-Responsive Vehicles for Intracellular Drug Delivery. *Angew Chemie Int Ed*. 2011;50(4):882-886. doi:10.1002/ANIE.201005471

276. Ruiz-Hernández E, Baeza A, Vallet-Regí M. Smart drug delivery through DNA/magnetic nanoparticle gates. *ACS Nano*. 2011;5(2):1259-1266. doi:10.1021/nn1029229

277. Schlossbauer A, Warncke S, Gramlich PME, et al. A programmable DNA-based molecular valve for colloidal mesoporous silica. *Angew Chemie - Int Ed*. 2010;49(28):4734-4737. doi:10.1002/anie.201000827

278. He D, He X, Wang K, Cao J, Zhao Y. A Photon-Fueled Gate-Like Delivery System Using i-Motif DNA Functionalized Mesoporous Silica Nanoparticles. *Adv Funct Mater*. 2012;22(22):4704-4710. doi:10.1002/ADFM.201201343

279. Chen L, Di J, Cao C, et al. A pH-driven DNA nanoswitch for responsive controlled release. *Chem Commun*. 2011;47(10):2850-2852. doi:10.1039/c0cc04765a

280. Li W-P, Liao P-Y, Su C-H, Yeh C-S. Formation of Oligonucleotide-Gated Silica Shell-Coated Fe3O4-Au Core–Shell Nanotrisoctahedra for Magnetically Targeted and Near-Infrared Light-Responsive Theranostic Platform. *J Am Chem Soc*. 2014;136(28):10062-10075. doi:10.1021/JA504118Q

281. Yang X, Liu X, Liu Z, Pu F, Ren J, Qu X. Near-infrared light-triggered, targeted drug delivery to cancer cells by aptamer gated nanovehicles. *Adv Mater*. 2012;24(21):2890-2895. doi:10.1002/adma.201104797

282. Cao X, Xia J, Meng X, Xu J, Liu Q, Wang Z. Stimuli-Responsive DNA-Gated Nanoscale Porous Carbon Derived from ZIF-8. *Adv Funct Mater*. 2019;29(34):1902237. doi:10.1002/ADFM.201902237

283. Yuan Q, Zhang Y, Chen T, et al. Photon-Manipulated Drug Release from a Mesoporous Nanocontainer Controlled by Azobenzene-Modified Nucleic Acid. *ACS Nano*. 2012;6(7):6337-6344. doi:10.1021/NN3018365

284. Graczyk A, Pawlowska R, Jedrzejczyk D, Chworos A. Gold nanoparticles in conjunction with nucleic acids as a modern molecular system for cellular delivery. *Molecules*. 2020;25(1):204. doi:10.3390/molecules25010204

285. Williams DM. Clinical pharmacology of corticosteroids. *Respir Care*. 2018;63(6):655-670. doi:10.4187/respcare.06314

286. National Cancer Institute. Dexamethasone. NIH. Published 2021. https://www.cancer.gov/about-cancer/treatment/drugs/dexamethasone

287. European Medicines Agency. EMA endorses use of dexamethasone in COVID-19 patients on oxygen or mechanical ventilation.

288. Rossi A, Donati S, Fontana L, et al. Negatively charged gold nanoparticles as a dexamethasone carrier: Stability in biological media and bioactivity assessment: In vitro. *RSC Adv*. 2016;6(101):99016-99022. doi:10.1039/c6ra19561j

289. Venditti I, Fontana L, Fratoddi I, et al. Direct interaction of hydrophilic gold nanoparticles with dexamethasone drug: Loading and release study. *J Colloid Interface Sci*. 2014;418:52-60. doi:10.1016/j.jcis.2013.11.063

290. Larsson C, Rodahl M, Höök F. Characterization of DNA immobilization and subsequent hybridization on a 2D arrangement of streptavidin on a biotin-modified lipid bilayer supported on SiO2. *Anal Chem*. 2003;75(19):5080-5087. doi:10.1021/ac034269n

291. Śmiałek MA, Jones NC, Hoffmann SV, Mason NJ. Measuring the density of DNA films using ultraviolet-visible interferometry. *Phys Rev E - Stat Nonlinear, Soft Matter Phys*. 2013;87(6):060701. doi:10.1103/PHYSREVE.87.060701/FIGURES/3/MEDIUM

292. Wong AC, Wright DW, Wong AC, Wright DW. Size-Dependent Cellular Uptake of DNA Functionalized Gold Nanoparticles. *Small*. 2016;12(40):5592-5600. doi:10.1002/SMLL.201601697

293. Shen J, Jiang X, Xu L, et al. Poly-Adenine-Engineered Gold Nanogaps for SERS Nanostructures. *ACS Appl Nano Mater*. 2019;2(6):3501-3509. doi:10.1021/ACSANM.9B00473/SUPPL_FILE/AN9B00473_SI_001.PDF

294. de Izarra A, Jang YH, Lansac Y. DNA-assisted assembly of cationic gold nanoparticles: Monte Carlo simulation. *Soft Matter*. 2021;17(41):9315-9325. doi:10.1039/D1SM01014J

295. Wolski P, Nieszporek K, Panczyk T. Carbon Nanotubes and Short Cytosine-Rich Telomeric DNA Oligomeres as Platforms for Controlled Release of Doxorubicin—A Molecular Dynamics Study. *Int J Mol Sci*. 2020;21(10):3619. doi:10.3390/IJMS21103619

296. Ghosh S, Das T, Chakraborty S, Das SK. Predicting DNA-mediated drug delivery in interior carcinoma using electromagnetically excited nanoparticles. *Comput Biol Med*. 2011;41(9):771-779. doi:10.1016/j.compbiomed.2011.06.013

297. Duncan B, Kim C, Rotello VM. Gold nanoparticle platforms as drug and biomacromolecule delivery systems. *J Control Release*. 2010;148(1):122-127. doi:10.1016/j.jconrel.2010.06.004

298. Siegel RL, Miller KD, Jemal A. Cancer statistics, 2019. *CA Cancer J Clin*. 2019;69(1):7-34. doi:10.3322/caac.21551

299. Wang C, Huang S. Drug development against metastatic cancers. *Yale J Biol Med*. 2017;90(1):119-123.

300. D'Errico G, Machado HL, Sainz B. A current perspective on cancer immune therapy: step-by-step approach to constructing the magic bullet. *Clin Transl Med*. 2017;6(3). doi:10.1186/s40169-016-0130-5

301. Tarantino P, Carmagnani Pestana R, Corti C, et al. Antibody–drug conjugates: Smart chemotherapy delivery across tumor histologies. *CA Cancer J Clin*. Published online 2021. doi:10.3322/caac.21705

302. Andre F, Mardis E, Salm M, Soria JC, Siu LL, Swanton C. Prioritizing targets for precision cancer medicine. *Ann Oncol*. 2014;25(12):2295-2303. doi:10.1093/annonc/mdu478

303. Swanton C. Intratumor heterogeneity: Evolution through space and time. *Cancer Res*. 2012;72(19):4875-4882. doi:10.1158/0008-5472.CAN-12-2217

304. Chen L, Hong W, Ren W, Xu T, Qian Z, He Z. Recent progress in targeted delivery vectors based on biomimetic nanoparticles. *Signal Transduct Target Ther*. 2021;6(1). doi:10.1038/s41392-021-00631-2

305. Kohane DS. Microparticles and nanoparticles for drug delivery. *Biotechnol Bioeng*. 2007;96(2):203-209.

306. Frederick CA, Williams LD, Ughetto G, et al. Structural Comparison of Anticancer Drug-DNA Complexes: Adriamycin and Daunomycin. *Biochemistry*. 1990;29(10):2538-2549. doi:10.1021/bi00462a016

307. Chaires JB, Fox KR, Herrera JE, Britt M, Waring MJ. Site and Sequence Specificity of the Daunomycin-DNA Interaction. *Biochemistry*. 1987;26(25):8227-8236. doi:10.1021/bi00399a031

308. Peppas NA. Analysis of Fickian and non-Fickian drug release from polymers. *Pharm Acta Helv*. 1985;60(4):110-111.

309. Rybenkov V V., Cozzarelli NR, Vologodskii A V. Probability of DNA knotting and the effective diameter of the DNA double helix. *Proc Natl Acad Sci U S A*. 1993;90(11):5307-5311. doi:10.1073/pnas.90.11.5307

310. Hsieh CC, Balducci A, Doyle PS. Ionic effects on the equilibrium dynamics of DNA confined in nanoslits. *Nano Lett*. 2008;8(6):1683-1688. doi:10.1021/nl080605+

311. Graves DE, Krugh TR. Adriamycin and Daunorubicin Bind in a Cooperative Manner to Deoxyribonucleic Acid. *Biochemistry*. 1983;22(16):3941-3947. doi:10.1021/bi00285a033

312. Fritzsche H, Akhebat A, Taillandier E, Rippe K, Jovin TM. Structure and Interactions of Parallel-Stranded DNA Studied by Infrared Spectroscopy and Fluorescence. *Fifth Int Conf Spectrosc Biol Mol*. 1993;21(22):5085-5091. doi:10.1007/978-94-011-1934-4_21

313. Lai CL, Chen C, Ou SC, Prentiss M, Pettitt BM. Interactions between identical DNA double helices. *Phys Rev E*. 2020;101:032414. doi:10.1103/PhysRevE.101.032414

314. Tariq Z, Barthwal R. Binding of anticancer drug daunomycin to parallel G-quadruplex DNA [d-(TTGGGGT)]4 leads to thermal stabilization: A multispectroscopic investigation. *Int J Biol Macromol*. 2018;120:1965-1974. doi:10.1016/j.ijbiomac.2018.09.154

315. Cutler JI, Auyeung E, Mirkin CA. Spherical nucleic acids. *J Am Chem Soc*. 2012;134(3):1376-1391. doi:10.1021/ja209351u

316. Shu Y, Haque F, Shu D, et al. Fabrication of 14 different RNA nanoparticles for specific tumor targeting without accumulation in normal organs. *RNA*. 2013;19(6):767-777. doi:10.1261/rna.037002.112

317. Afonin KA, Lindsay B, Shapiro BA. Engineered RNA Nanodesigns for Applications in RNA Nanotechnology. *DNA RNA Nanotechnol*. 2013;1(1):1-15. doi:10.2478/rnan-2013-0001

318. Jasinski DL, Khisamutdinov EF, Lyubchenko YL, Guo P. Physicochemically tunable polyfunctionalized RNA square architecture with fluorogenic and ribozymatic properties. *ACS Nano*. 2014;8(8):7620-7629. doi:10.1021/nn502160s

319. Gorin SNS, Jimbo M, Heizelman R, Harmes KM, Harper DM. The future of cancer screening after COVID-19 may be at home. *Cancer*. 2021;127(4):498-503. doi:10.1002/cncr.33274

320. Thakor AS, Gambhir SS. Nanooncology: The future of cancer diagnosis and therapy. *CA Cancer J Clin*. 2013;63(6):395-418. doi:10.3322/caac.21199

321. YT Chow M, KW Lam J. Dry powder formulation of plasmid DNA and siRNA for inhalation. *Curr Pharm Des*. 2015;21(27):3854-3866.

322. Nafee N, Gouda N. Nucleic Acids-based Nanotherapeutics Crossing the Blood Brain Barrier. *Curr Gene Ther*. 2017;17(2):154-169. doi:10.2174/1566523217666170510155803

323. Zhou L, Pi W, Hao M, et al. An injectable and biodegradable nano-photothermal DNA hydrogel enhances penetration and efficacy of tumor therapy. *Biomater Sci*. 2021;9(14):4904-4921. doi:10.1039/d1bm00568e